Dielectric Properties of Amorphous Phase-Change Materials

Von der Fakultät für Mathematik, Informatik und Naturwissenschaften der RWTH Aachen University zur Erlangung des akademischen Grades eines Doktors der Naturwissenschaften genehmigte Dissertation

vorgelegt von
Master-Physikerin
Chao Chen
aus China

Berichter: Universitätsprofessor Dr. rer. nat. Matthias Wuttig
Dr. rer.nat. Ricardo P. S. M. Lobo

Tag der mündlichen Prüfung: 4th/May/2018

Abstract

The AC conductivities and dielectric properties of five amorphous phase-change materials (PCMs) and three ordinary chalcogenides have been determined by employing a combination of the AC electrical measurement (0.5 Hz – 186.2 Hz), the impedance spectroscopy (9 kHz – 3 GHz) and the optical spectroscopy (20 cm^{-1} – 12000 cm^{-1}, i.e., 0.6 THz – 360 THz). Those measurements almost range from the DC limit to the first interband transition. In addition, the temperature dependence of the low-frequency dielectric permittivity and the AC conductivities of amorphous PCMs were also investigated by the AC electrical measurement in the range of 4 K – 170 K and by the impedance spectroscopy in the range of 220 K – 350 K. Moreover, the aging effect on these properties of amorphous GeTe thin films annealed for one hour at successively higher temperatures, i.e. 333 K, 353 K, 373 K, 393 K, 403 K was studied by the AC electrical measurement.

This work mainly focuses on amorphous PCMs. Firstly, measurements of AC conductivities of amorphous PCMs have been extensively used to understand the conduction process in these materials. No frequency dependence of AC conductivities is discernible in the impedance spectroscopy measurements, which is in line with charge transport via extended states. Secondly, the permittivities of amorphous PCMs are frequency independent among the impedance measurement frequency range. Consequently, there are no dielectric relaxations in this range. Thirdly, the static dielectric constants of amorphous PCMs significantly exceed their optical dielectric constants. This observation is corroborated by transmittance measurements in the far-infrared, which show optical phonons. Particular attention is also paid to the correlation between the dielectric constant and Born effective charge of the amorphous phase-change materials. From the intensity of these phonon modes, a large Born effective charge is derived. Nevertheless, it is known that crystalline PCMs such as GeTe possess even significantly larger Born effective charges. Crystallization is hence accompanied by a huge increase in the Born effective charge, which reveals a significant change of bonding upon crystallization. Interestingly, a clear stoichiometry trend in the static dielectric constant along the pseudo-binary line between GeTe and Sb_2Te_3 has been identified.

On the other hand, there is a comparison of dielectric properties between the PCMs and non-PCMs. The optical dielectric constants of amorphous PCMs increase a lot after crystallization, while there is no difference between the optical dielectric constants of the amorphous and crystalline chalcogenide $AgInTe_2$. This illustrates that the PCMs undergo a change from covalent bonding to resonant bonding on crystallization, but the amorphous and crystalline phases of ordinary chalcogenides are both governed by virtually the same covalent bonds. In addition, the static dielectric constants obtained for PCMs on the pseudo-binary line between GeTe and Sb_2Te_3 are compared with those obtained for ordinary covalently-bonded chalcogenide semiconductors. The static dielectric constants of both PCMs and non-PCMs significantly enhance from amorphous to crystalline, which hints that the contribution of infrared active phonons is remarkably strengthened in the crystalline states of both PCMs and non-phase-change materials. Moreover, the temperature dependence of dielectric constants of amorphous chalcogenides shows the contribution enhancement of infrared active phonons with temperature.

Lastly, the aging effect on the dielectric property of amorphous GeTe thin films derived from the experimental results is in good agreement with the results of density functional theory (DFT) calculations, which at the same time reveal the bonding mechanisms and atomic structures in the representative amorphous phase.

Abstrakt

Die Wechselstromleitfähigkeit und die dielektrischen Eigenschaften von fünf amorphen Phasenänderungsmaterialien (PCMs) und drei gewöhnlichen Chalkogeniden wurde bestimmt durch eine Kombination aus elektrischer Wechselstrommessung (0.5 Hz – 186.2 Hz), Impedanzspektroskopie (9 kHz – 3 GHz) und optischer Spektroskopie (20 cm^{-1}– 12000 cm^{-1}, dh. 0.6 THz – 360 THz). Der Messbereich der drei Techniken deckt vom DC-Limit bis zum ersten Interband-Übergang nahezu ab. Zusätzlich wurden die Temperaturabhängigkeit der niederfrequenten Dielektrizitätskonstanten und die Wechselstromleitfähigkeit von amorphen PCMs auch durch elektrische AC-Messung im Bereich von 4 K – 170 K und Impedanzspektroskopie im Bereich von 220 K – 350 K untersucht. Darüber hinaus wurde die Abhängigkeit dieser Eigenschaften vom Alterungseffekt amorpher GeTe-Dünnschichten, welche für eine Stunde mit steigenden Temperaturen (dh 333 K, 353 K, 373 K, 393 K, 403 K) geglüht wurden, durch elektrische AC-Messung untersucht.

Diese Arbeit konzentriert sich hauptsächlich auf amorphe PCMs. Erstens wurden Messungen der Wechselstromleitfähigkeiten von Materialien mit amorpher Phasen extensiv verwendet, um den Leitungsprozess in diesen Materialien zu verstehen. Bei den Impedanzspektroskopiemessungen ist keine Frequenzabhängigkeit der AC-Leitfähigkeiten erkennbar, was dem Ladungstransport über ausgedehnte Zustände entspricht. Zweitens sind die Permittivitäten von amorphen PCMs unter dem Impedanzmessfrequenzbereich frequenzunabhängig. Folglich gibt es in diesem Bereich keine dielektrischen Relaxationen. Drittens übersteigen die statischen Dielektrizitätskonstanten von amorphen PCMs signifikant ihre optischen Dielektrizitätskonstanten. Diese Beobachtung wurde durch Transmissionsmessungen im fernen Infrarot bestätigt, welche optische Phononen zeigten. Besondere Aufmerksamkeit wurde auch der Korrelation zwischen der Dielektrizitätskonstante und der effektiven Ladung der amorphen PCMs gewidmet. Aus der Intensität dieser Phononenmodi wurde eine große effektive Born-Ladung abgeleitet. Es ist jedoch bekannt, dass kristalline PCMs wie GeTe sogar signifikant größere effektive Born-Ladungen besitzen. Die Kristallisation wird daher von einer starken Zunahme der effektiven Born-Ladung begleitet, die für eine signifikante Änderung der Bindung bei der Kristallisation charakteristisch ist. Interessanterweise wurde ein deutlicher Stöchiometrie Trend in der statischen

Dielektrizitätskonstante entlang der pseudo-binären Linie zwischen GeTe und Sb_2Te_3 identifiziert.

Desweiteren wurden die dielektrischen Eigenschaften der PCMs mit den Nicht-PCMs verglichen. Die optischen Dielektrizitätskonstanten von amorphen PCMs steigen nach der Kristallisation stark an, während die optischen Dielektrizitätskonstanten des amorphen und kristallinen Chalkogenids $AgInTe_2$ keinen Unterschied aufwiesen. Dies veranschaulicht, dass die PCMs eine Änderung von kovalenten Bindungen zu resonanten Bindungen bei der Kristallisation erfahren, aber die amorphen und kristallinen Phasen gewöhnlicher Chalcogenidhalbleiter werden beide von nahezu den gleichen kovalenten Bindungen bestimmt. Zusätzlich wurden die statischen Dielektrizitätskonstanten, die für PCMs entlang der pseudo-binären Linie zwischen GeTe und Sb_2Te_3, mit denen für gewöhnliche kovalent gebundene Chalcogenidhalbleiter verglichen. Die statischen Dielektrizitätskonstanten von sowohl PCMs als auch Nicht-PCMs steigen signifikant von amorph zu kristallin an, was darauf hindeutet, dass der Beitrag von infrarotaktiven Phononen in den kristallinen Zuständen sowohl von PCMs als auch von Nicht-PCMs bemerkenswert verstärkt ist. Darüber hinaus zeigt die Temperaturabhängigkeit der Dielektrizitätskonstanten von amorphen Chalkogeniden die Beitragsverstärkung von infrarotaktiven Phononen mit der Temperatur.

Der aus den experimentellen Ergebnissen abgeleitete Alterungseffekt auf die dielektrischen Eigenschaften von amorphen GeTe-Dünnschichten stimmt schließlich gut mit den Ergebnissen der Dichtefunktionaltheorie (DFT) überein, die gleichzeitig die Bindungsmechanismen und atomaren Strukturen in der repäsentativen amorphen Phase zeigen.

Contents

Introduction

1.1 PCMs

As the name implies, phase-change materials (PCMs) are materials that make use of properties transition from one phase to another. There are five classes of PCMs based on the following alloys separately: $(GeTe)_{1-x}(Sb_2Te_3)_x$ (GST for short) [WY07, SMW12, Raou09]; Ag/In/Ge doped Sb_2Te (eg. $Ag_4In_3Sb_{67}Te_{26}$) [WY07]; $(GeTe)_{1-y}(SnTe)_y$ [Herp09, LPB+13] and In_3SbTe_2 [WY07, MAI+88]; Ge doped Sb (eg. $Ge_{15}Sb_{85}$) [Herp09]. This thesis mainly focuses on the PCMs of the first class, which are characterized by both low ionicity and hybridization [LSG+08]. Those materials are expected to meet requirements given in table 1.1 for data storage application.

Table 1.1 Fundamental features of the PCMs for data storage. Adapted from Wuttig et al. [WY07].

Requirements of materials for data storage	**Features of the PCMs**
High–speed phase transition	Induced by nanosecond laser or voltage pulse
Long thermal stability of amorphous state	At least several decades at room temperature
Large optical change between the two states (for rewriteable optical storage)	Considerable difference in refractive index and/or absorption coefficient
Large resistance change between the states (for non-volatile electronic storage)	Resistivity change 10^3 – 10^4 times from amorphous to crystalline state
Large of reversible transitions cycles	Around 10^{10} cycles with stable composition
High chemical stability	High water-resistivity

Phase-change memory technology relies on the electrical or optical properties of certain materials changing substantially when the atomic structure of the material is altered by heating or some other excitation processes. The electrical resistivity of amorphous GST compounds decrease about 3 – 4 orders of magnitude on crystallizing [SJV+11, FWN+00]. The optical dielectric constant ε_∞ of the crystalline PCMs are 70 – 200% larger than that of the amorphous

phases. The prominent optical contrast in the energy range from 25 meV to 3 eV is attributed to the existence of resonant bonding in the crystalline PCMs [SKW+08]. The high crystallization speed of PCMs is also crucial for applications in rewritable optical discs and electronic memory cells.

Table 1.2 lists properties possessed by the PCMs along the GeTe-Sb_2Te_3 pseudo-binary line. The atomic density of amorphous PCMs calculated according to their mass density decreases as the content of Sb_2Te_3 goes up. Obviously both the crystallization and melting temperatures of the PCMs decrease monotonically from GeTe to $Ge_1Sb_2Te_4$, which is partly attributed to the increase of the fraction of weaker Sb-Te bonds (277.5 kJ/mol [SKL+17]) and the decrease of the stronger Ge-Te bonds (402 kJ/mol [SKL+17]). Only those materials with sufficient content of GeTe, which crystallize above 373 K (i.e. 100 ˚C) to ensure the long-term stability of the amorphous state at typical application temperatures, can be employed as PCMs. Furthermore, the optical contrast between the amorphous and crystalline phases weakens as the composition of Sb_2Te_3 increases.

Table 1.2 The mass density, atomic density, crystallization temperature T_c, melting temperature T_m and the optical dielectric constant of the amorphous PCMs along the pseudo-binary line are summarized [Krem09, Zald12, YON+91, Luck12]. Amorphous (abbreviated as a-), crystalline (abbreviated as c-).

Materials	Density ρ (g/cm^3)	Atomic density N	T_c (K)	T_m (K)	ε_∞ a-	ε_∞ c-
GeTe	5.50	3.31E22	460	943	13.2	33.2
$Ge_8Sb_2Te_{11}$	5.45	3.10E22	455	903	13.5	36.2
$Ge_3Sb_2Te_6$	5.80	3.13E22	427	903	12.1	36.0
$Ge_2Sb_2Te_5$	5.82	3.07E22	425	879	16.0	33.3
$Ge_1Sb_2Te_4$	5.95	3.04E22	412	877	16.6	36.2

1.1.1 Crystalline PCMs

GeTe crystallizes in a distorted rocksalt structure (α phase) and will change to an undistorted rocksalt structure (β phase) at higher temperatures. Ternary GST alloys have two different crystalline structures including the intermediate metastable cubic structure (rocksalt-like) and

stable hexagonal (trigonal) structure. The valence configuration of antimony is $5s^2 5p^3$, and the 5s electrons are significantly lower in energy than the 5p orbitals. This energy gap decreases the hybridization and prevents the formation of sp^3 bonds between Sb and Te. The antimony becomes trivalent and forms covalent bonds with the tellurium by sharing its p electrons. The competition between the covalent bonding and lone pair repulsion in some of the rocksalt-based GST compounds leads to crystal instability [MVJ13]. Hence, the cubic structure is metastable. Data storage involves a fast phase transformation only between the metastable crystalline phase and amorphous phases because the metastable state is faster achieved and the short timescale is favored.

The cubic crystalline GST has two sublattices, in which Te locates at the anion lattice sites and Ge, Sb, and vacancy randomly locate at the cation lattice sites. Taking $Ge_1Sb_2Te_4$ as an example, one sublattice is occupied by tellurium, while the other is occupied by 50% antimony, 25% germanium and 25% intrinsic vacancies. Likewise, there are 20% vacancies in $Ge_2Sb_2Te_5$. It is demonstrated that additional ("excess-") vacancies in GST compounds lead to their p-type conduction [MKY+06].

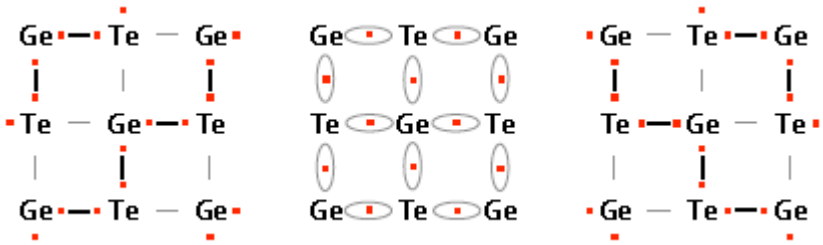

Figure 1.1 ***Resonant bonding diagram of GeTe.*** *Two dimensional cross-section of the rocksalt structure of GeTe. On average, 3 p-electrons are available in the 6-fold coordination of each atom. The material has several different configurations to form ordinary covalent bonds, two of which are shown in the left and right. Resonant bonding formed by a hybrid wave function with lower energy, shown in the center, is responsible for the high electronic polarizability in crystalline PCMs. Reprinted from Merkelbach [Merk11].*

The average number of p electrons in the lattice site of cubic GST compounds is 3 and all lattice sites have a 6-fold coordination. The bonding of GST alloys is governed by p-orbitals. The

crystalline PCMs characterized by a large electronic polarizability, which has been explained through the effect of resonant bonding [SKW+08]. Resonant bonding can only form in the crystalline GST materials having translational periodicity. The mechanism of resonant bonding in GeTe is shown in figure 1.1.

1.1.2 Amorphous PCMs

Zachariasen et al. [Zach32] proposed that the principal difference between the network of a crystal and the related glasses is the presence of symmetry and periodicity in the former and the absence of periodicity and symmetry in the latter. The atoms in Zachariasen glasses are linked together by forces essentially the same as in crystals and the local structure of amorphous states should follow their parent crystalline phase. Ioffe and Regel [IR60] also suggested that the properties of an amorphous semiconductor would be broadly similar to those of the related crystalline semiconductors in spite of the lack of long-range order, if the crystalline short-range order is preserved. But the observations in amorphous PCMs are contradictory to this view. Amorphous PCMs possess covalent bonding with coordination numbers obeying the 8-N rule, which are much less than those in the corresponding crystalline phase. The average coordination number of Ge atoms inferred from Extended X-ray Absorption Fine Structure (EXAFS) data [SCM+11] decreases from sixfold in the crystal to a fourfold coordination in the amorphous. However, while a fourfold coordination can be reliably inferred from EXAFS, bonding angles are subject to large uncertainties. Recent ab initio molecular-dynamics simulations of a-$Ge_2Sb_2Te_5$ and a-GeTe [MSS+16] showed that while indeed some Ge atoms are mostly fourfold coordinated in the melt-quenched amorphous phases, the majority of Ge and all Te and Sb atoms are in defective octahedral with bond angles typical of the octahedral geometry (~ 90º or ~ 180º), but with coordination lower than six. This is consistent with the density functional theory (DFT) calculations of amorphous network in GeTe [RZL+15, AJ12], from which it is seen from the trends in the heat of formation that octahedral bonding is favored for GST alloys.

In contrast to a well-defined energy gap in crystalline state, there is a “mobility gap” in the amorphous semiconductors. The disorder in the structure of amorphous materials lead to a high density of localized states, which act as carrier-traps. Electrical properties of amorphous PCMs possess an Arrhenius behavior with an activation energy of about half the bandgap. There are

two important phenomena of threshold switching and resistance drift in amorphous PCMs, any explanatory approach of which is impeded by the fact that there is no commonly accepted view of the charge transport mechanism.

1.1.2.1 Threshold Switching

Threshold switching is a kind of dielectric breakdown under a distinct electrical field. It has been firstly reported in semiconducting glasses by Ovshinsky in 1968 [Ovsh68]. The current-voltage characteristics of the phase-change memory cell are shown in figure 1.2. The initially high resistive OFF-state breaks down with resistance decrease by orders of magnitude at the electrical threshold field E_t, after which a conductive ON-state is entered. The OFF-current is strongly temperature dependent, non-Ohmic before switching and it is proportional to the electrode area for un-switched devices, while the ON-voltage is hardly dependent on the film thickness [AHM78]. The weak thickness dependence of ON-state indicates that the electric field drops mostly at the electrodes instead of the film volume. These features indicate that the threshold switching is not caused by thermal breakdown [PLB+04], but by a non-equilibrium enhancement of either carrier concentration or mobility or both (electronic processes) [WS14]. The physical description of threshold switching may thus contribute to the conceptual clarification of transport mechanisms at localized states in amorphous semiconductors. Several transport mechanisms, such as small-polaron hopping [Emin06] and thermally induced Poole-Frenkel conduction [IZ07, IZ072], have been established, unfortunately, none of them is commonly accepted or without shortcomings. The threshold switching is explained in Ielmini [Ielm08] by the field-induced energy increase of electrons in their hopping transport, moderated by the energy relaxation due to phonon-electron interaction. Emin et al. [Emin06] also attributed the threshold switching phenomenon to a drastic change in mobility of small polarons acting as charge carriers in a-PCMs at low electric fields.

The recrystallization of the amorphous volume requires a certain heating power $Q = (U^2/R)t$. If the high resistance of the amorphous phase in a memory cell, which allows for a safe readout, was independent of voltage, it would not be possible to introduce enough Joule heating power at appropriate voltages in a short time to crystallize the material. Therefore this non-linear behavior is crucial for the electrical switching for data-storage in a phase-change memory cell.

Both the threshold effect and crystallization kinetics help to resolve the voltage-time dilemma in PCM-based memories.

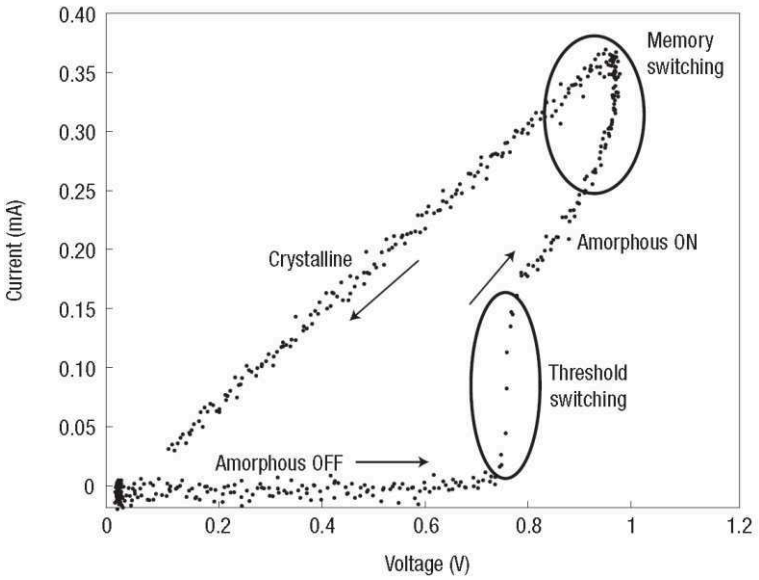

Figure 1.2 ***Typical current – voltage curve of the phase-change memory cell.*** *It starts from the amorphous state with large resistance, which leads to an extremely slow increase of current with the voltage. The resistance drops dramatically at the threshold switching electric field E_t. This allows for significant heating for crystallization after holding E_t for a sufficient duration, otherwise the material returns to the amorphous, high resistant state. Reprinted from Wuttig et al. Reprinted from [WY07].*

1.1.2.2 Resistance Drift

Aging effect exists ubiquitously in glasses and it leads to resistance drift in phase-change chalcogenide alloys. The resistance drift refers to the increase of electrical resistance with time, which is phenomenologically described by

$$R = R_0 (\frac{t}{t_0})^{\nu} \qquad (1.1),$$

where R and R_0 are the resistance at time t and t_0 and ν is the drift exponent. This phenomenon is attributed to structural relaxation claimed in many references [Zald12, BI11]. It hampers the

implementation of multi-level storage as the resistance of an intermediate level may reach values associated with a more resistive state. In order to realize the application of PCMs in multilevel-storage technologies, one has to overcome the challenge of controlling the resistance drift in the amorphous state of these materials. It would then be desirable to achieve a full microscopic understanding of this process to keep it under control and eventually to minimize its effects by a suitable tuning of the alloy composition without sacrificing the other function.

Gabardi et al. [GCS+15] studied the atomistic origin of the resistance drift in the prototypical phase-change compound GeTe by means of combined molecular dynamics and electronic structure calculations. The result suggested that chains of Ge-Ge homopolar bonds were removed because of structural relaxations with time, which caused a widening of the bandgap and a reduction of Urbach tails, and hence the resistance drift. This is consistent with the DFT calculation by Raty et. al. [RZL+15]. The aging mechanisms in amorphous PCMs will be further investigated by the AC electrical measurement in Chapter 5.

1.1.3 Application Principles for Data Storage

The working principle of the phase-change memory is depicted in figure 1.3. The resistance of memory cell in the amorphous state is high, since the amorphous phase-change material (PCM) has a large resistivity. With a moderate electrical pulse, the amorphous PCM can be heated to transform into a crystalline state (set), which has a high conductivity. To re-amorphize (reset) the memory cell, a short pulse of higher power is needed to heat the PCM over the melting temperature into liquid, which is subsequently cooled rapidly by the environment to form the amorphous state. The state of the memory cell needs a pulse of low power to read out (read) without being changed. Similarly, rewritable optical storage makes use of the contrast in reflectivity of light of a given wavelength (i.e. different optical refractive index) on the PCM.

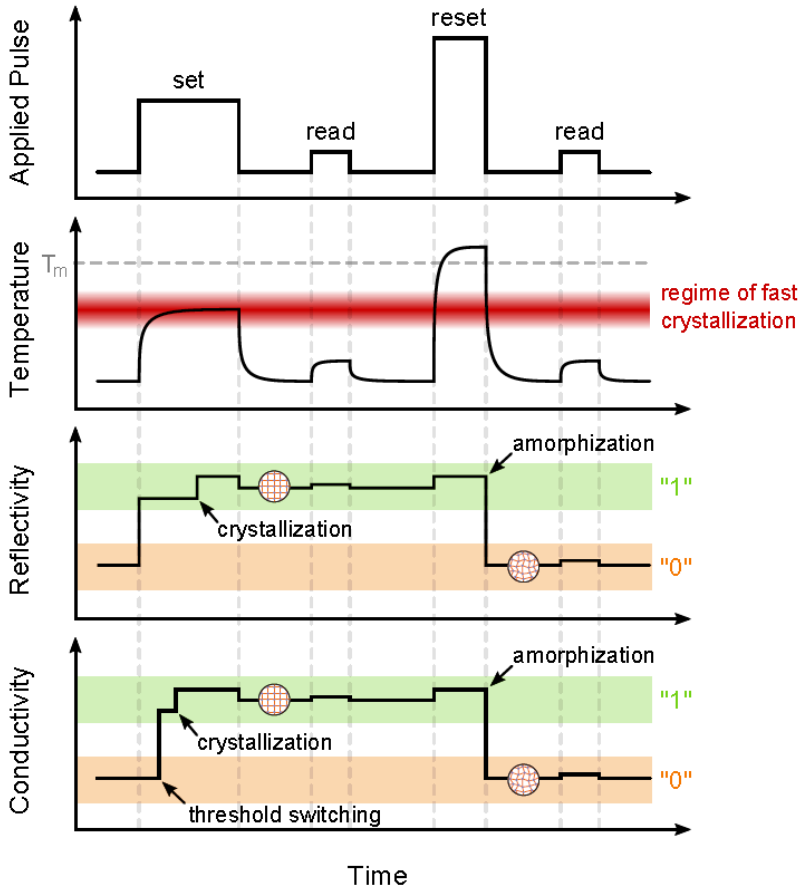

Figure 1.3 ***Diagram of the working principle of phase-change memory.*** *The amorphous PCM is heated using a laser or voltage pulse into the fast crystallization regime (in red) and then the crystalline state "1" (in green). In order to reset the PCM into amorphous state "0" (in orange), a pulse with higher power is applied for a shorter time, after which the material can cool down very rapidly without crystallization. A low power pulse enables reading out both states of the material without changing the states. Reprinted from Krebs [Kreb10].*

1.2 Motivations

The ever-increasing demand for storing and accessing data requires memory media with higher capacity, faster speed and lower energy consumption. Chalcogenide-based PCMs are very attractive due to their potential for optical and electrical data storage applications [Ovsh68, WY07, BBF+10, HOM+06, LSW11]. These applications rely on a pronounced property

contrast between the amorphous and the crystalline phase in combination with the possibility to switch rapidly between these phases to code "0" s and "1" s. They have already been applied in rewriteable optical discs, such as blue-ray disc (BD). Recently, electronic phase-change random access memories (PRAMs) have raised particular interest since they enable data storage in a way that differs from the presently employed Flash Memory and Dynamic Random Access Memory (DRAM). In particular, PRAMs uniquely combine non-volatility and high switching speeds (10 ns [BMS+09]) with good endurance (10^{10} cycles [Hwa15]).

In the last decade, substantial progress has been made in understanding structure, bonding, and charge transport in crystalline PCMs [LSG+08, SKW+08, SJV+11, ZTZ+12, HR10]. At the same time, the resistance drift [GCS+15] in the amorphous state and the high switching speeds have motivated significant interest in the atomic arrangement of the amorphous state. Zachariasen [Zach32] et al. reported in 1932 that basic structural units in a glass are connected in a random manner without the periodic arrangement such as in a crystalline material, but the nature of bonding in a glass material is the same as in its crystalline state. This is very different in PCMs, where resonant bonding exists in the crystalline [LSG+08, SKW+08], but not in the amorphous state [HR10, KBJ+14, AJ07]. Hence, ab-initio theory as well as advanced X-ray and neutron methods have been employed extensively to study the local structure of amorphous PCMs [KFF+04, JKS+08, KKF+11]. Nevertheless, as it can be inferred from the ongoing discussion, the atomic arrangement and bonding in the amorphous state as well as the phase-change mechanism are still under debate [MOI+16, DZL+14]. Consequently, the already mentioned amorphous-state phenomena resistance drift and threshold switching [WW08] are not yet fully understood, which hampers the development of PCMs-based electronic devices and the realization of multilevel memories [KBJ+14].

Detailed knowledge of the dielectric response between the DC limit and the infrared-regime provides valuable input to address many of the questions currently under debate: For instance, a plethora of theoretical models for the structure of amorphous PCMs has been developed [AJ07, AJK+09, HE08, CBK+09]. The polarizability depends on subtle details of structure and bonding. The nature of the bond has an effect on the polarizability of the electron system (optical dielectric constant, i.e. ε_∞), on the polarizability of the phonons (static dielectric constant, i.e. ε_{st}), and, of course, on the phonon frequencies. These quantities can easily be derived from the

dielectric function. Hence, knowledge of the static dielectric constant and the phonons can help in gauging and singling out competing DFT models for amorphous PCMs. In addition, exact knowledge of the static dielectric constant is desirable for the simulation of capacitive effects in high-speed PRAM devices [RBB+08]. Moreover, comparing differences in the dielectric functions of amorphous and crystalline PCMs of the same stoichiometry should help in unraveling the bonding in amorphous PCMs.

The optical dielectric constants ε_∞ of amorphous and crystalline PCMs have been reasonably derived from the Fourier transform infrared (FT-IR) spectroscopy in the infrared and spectroscopic ellipsometry in the visible region [SKW+08, Krem09, PBK+08]. However, only very few attempts to determine the static dielectric constant have been reported. The conclusions summarized from these earlier investigations are puzzling. Both Prokhorov et al. [PGL+13], and Santos et al. [SPH+10] performed measurements up to the MHz range. They reported numbers of the static dielectric constant, which are, within error bars, identical to the high frequency (optical) dielectric constant as derived by Shportko [SKW+08]. This equality of ε_{st} and ε_∞ is difficult to understand. For any material possessing optical phonons accompanied by a dynamic dipole moment (IR-active phonons), ε_{st} must exceed ε_∞. Only for materials without a dynamic dipole moment, such as crystalline Si, ε_{st} equals ε_∞. As crystalline IV-VI semiconductors such as GeTe are characterized by very high values of the Born effective charge [LSG+08], it is very difficult to imagine that for the corresponding amorphous material a vanishing Born effective charge, i.e. no dipole moment, is found. Indeed, DFT calculations revealed a non-vanishing Born effective charge for amorphous GeTe [Emin76] and optical phonon modes have been observed by THz spectroscopy [ISL+09]. These findings are clearly incompatible with the statement that ε_{st} equals ε_∞.

Similar to the already mentioned competing structure models, several mutually incompatible models for the charge transport in amorphous PCMs such as the small polaron model [AJK+09], the Poole-Frenkel model [HE08], and the band transport model [CBK+09] have been suggested. Knowing the frequency dependence of the conductivity can help to determine the charge transport mechanism.

Therefore the above questions call for a thorough investigation via impedance spectroscopy, which provides both information on dielectric function and AC conductivity. It is possible that previous impedance spectroscopy data have suffered from shortcomings. Prokhorov et al. [RBB+08] and Li et al. [MGK89] reported that the resistivity of $Ge_2Sb_2Te_5$ at room temperature decreases by merely one order of magnitude on crystallization. This observation is in conflict with the majority of studies agreeing on a resistivity decrease of about 3 to 4 orders of magnitude [SJV+11, PGL+13] when crystallizing PCMs. This discrepancy might be a hint that the device resistance actually originates from highly resistive interface layers between the TiW electrodes and the PCM. Indeed, it was Street et al. [SPH+10] who already emphasized the detrimental impact of contact related effects in measurements on As_2Se_3, a composition closely related to PCMs. Hence special emphasis is put on the verification that data in this thesis are not affected by the interface effects.

In the master thesis of Schlich [Schl12] and Krüger [Krüg10], they have conducted impedance measurements on amorphous GeTe and amorphous $Ge_2Sb_2Te_5$. It is very challenging to fabricate qualified samples with the capacitor area from 10^2 μm^2 to 400^2 μm^2 by photo-lithography process. The AC conductivity and dielectric function were dependent on the device size, which hinted at sample defects. Hence the frequency dependence of the AC conductivity and dielectric function is also doubtful. The increase in the dielectric permittivity at low frequency is caused by charge blocking at the interface between the PCMs layer and electrodes, namely, Maxwell/Wagner polarization.

In this work, micro-sized capacitors of amorphous PCMs on the pseudo-binary line between GeTe and Sb_2Te_3 have been successfully developed for the impedance measurement. The interpretation of the impedance spectroscopy might be ambiguous when the ordinary lumped constant elements (i.e. R, C and L) are inadequate to describe the electrical response. And the equivalent circuit involving three or more circuit elements can often be substituted by other circuits with different elements. Hence, the impedance measurement at radio frequencies is corroborated by the AC electrical measurement at low frequencies close to DC. In order to overcome difficulties in measuring the dielectric permittivity at frequencies below kHz, the chalcogenides under investigation were cooled down to decrease the conductivity and then lower the resistive-to-capacitive transition frequency (i.e. f_{RC}) of the investigated devices.

Furthermore, it is desirable to measure the dielectric permittivity of thin films by the Fourier transform far-infrared (FT-FIR) measurement, which extends from the near-infrared to the far-infrared range. The FT-FIR spectra that investigated in the full infrared range provides information about the molecule vibrations of the solid. For comparison, three other chalcogenides, namely GeSe, $Ge_{15}Te_{85}$ and $AgInTe_2$, which do not possess the properties of PCMs, were also studied.

1.3 Aims and Structure of This Work

As solid experimental data on many physical properties of amorphous PCMs are still lacking, this thesis aims at providing an in-depth understanding of the dielectric functions and the AC conductivities of amorphous PCMs employing electrical measurements and optical spectroscopy. The thesis also elucidates the dielectric functions of some amorphous sp^3 bonded non-PCMs for comparison with the amorphous PCMs. Both AC conductivity and dielectric permittivity over frequency will be derived from the impedance spectroscopy and the FT-FIR spectroscopy data. It is useful to determine the frequency dependence of AC properties when attempting to decide on transport mechanisms and structure models. These findings are of general importance for the understanding of the physical properties of PCMs.

Results of the electrical and optical measurements in this thesis provide important information about the polarizability and phonon frequencies, which may be related to the (local) atomic arrangement and bonding in the amorphous network revealed by earlier synchrotron X-ray and neutron scattering studies. Thus, the data complement to the advanced X-ray and neutron methods: any model for the atomic arrangement in the amorphous state has to reproduce the geometrical information derived from X-ray and neutron experiments as well as the trends in polarizability and phonon-frequencies observed in this study. This may stimulate follow-up studies such as ab-initio calculations to help clarify the relation between the local structure and polarizability. Ab-initio calculations linking the observations to the presence of local structural motives and local vibrational modes would be highly desirable. However, performing such calculations would be clearly beyond the scope of this work.

In conclusion, the task of this work is to study the dielectric functions of the amorphous PCMs from near DC to the infrared region. This thesis is outlined as follows. The key properties of PCMs are introduced in this chapter. Charge transport mechanisms and dielectric functions of amorphous semiconductors will be summarized in chapter 2. The third chapter illustrates experimental methods involving the Physical Property Measurement System (PPMS), VNA and Fourier transform far-infrared (FT-FIR) transmission and FT-IR reflectance. Chapter 4 deals with the details of sample preparation. Afterwards, chapter 5 discusses the results of the AC electrical measurement at frequencies close to DC and chapter 6 explains the impedance measurement at radio frequencies. The temperature and frequency dependence of the AC conductivity and dielectric properties were measured for amorphous PCM-devices with different geometries, such as capacitor area and film thickness. In addition, the aging effect on the dielectric properties of amorphous GeTe thin films is measured by the AC electrical measurement and compared with the DFT calculation results by [RZL+15]. In chapter 7, both of the FT-IR reflectance spectra and FT-FIR transmission spectra are analyzed for the dielectric functions of PCMs and ordinary chalcogenides in the infrared range. Finally conclusions as well as an outlook are summarized and discussed in chapter 8.

Charge Transport Mechanisms in Amorphous Chalcogenides

This chapter summarizes electronic transport mechanisms in amorphous chalcogenides. In spite of a number of investigations, the nature of the AC conductivity in amorphous PCMs is still a matter of controversy. A brief summary of the general description of electrical transport models is given in section 2.1. Different defect states models of disordered structures are introduced, based on which electrical transport mechanisms are illustrated. Section 2.2 introduces the fundamental concepts behind the dielectric function, such as polarization mechanisms in different frequency regions and the Clausius-Mossotti relation. This relation explains the stoichiometric trend in the optical dielectric functions of PCMs. This chapter also illustrates the derivation of Born effective charges from optical spectra.

2.1 Electronic Transport Models in Amorphous Semiconductors

The amorphous semiconductors have no symmetry of the periodic electrostatic potential as in crystals, but their electronic energy spectra can be treated as quasi-continuous. The fluctuations in potential on the atomic scale caused by disorders induce defect states in amorphous states. Many transport models proposed for amorphous PCMs involve localized defect states. Electronic properties such as DC and AC conductivity of chalcogenide glasses depend on their electronic structure. The Fermi energy is supposed to pin in some way near the mid-gap for amorphous chalcogenides. The presence of localized trap states in the bandgap has a strong influence on the electronic properties in a disordered solid.

2.1.1 Defect States Models in Disordered Structures

A charge carrier occupying a trap state is described by an exponentially decaying wavefunction (i.e. localized wavefunction), which is localized in a spatially restricted region because of the disorder. On the contrary in an extended state, the wavefunction of the charge carrier is spread

over the whole volume of a sample. There are band tails originating from the lack of long-range order in disordered structures. The critical energies that separate the extended states from the localized ones in disordered materials are called the mobility edges, see E_C and E_V in figure 2.1. At the absolute zero of temperature only charge carriers above E_C or below E_V are mobile and contribute to transport, and the mobility of electrons and holes decrease by 2 to 3 orders of magnitude at the mobility edges of semiconductors [LA71, Mott87]. To describe the electronic transport in amorphous semiconductors, the mobility gap $E_C - E_V$ is introduced, which contains only localized states. States lying beyond the valence band edge E_V or conduction band edge E_C are delocalized and form the valence band and the conduction band, respectively. Conduction-band states are neutral when unoccupied, while valence-band states are neutral when occupied by an electron.

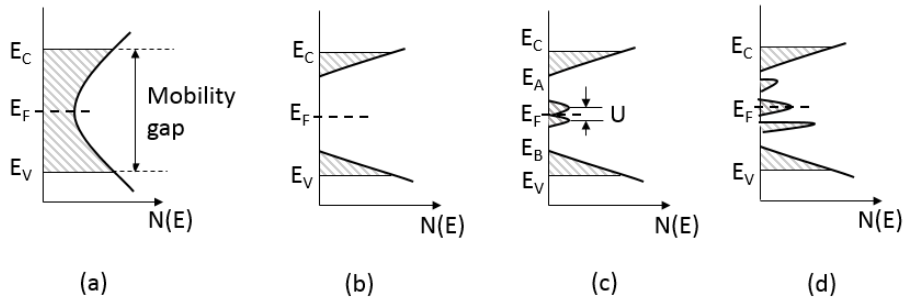

Figure 2.1 ***Various forms proposed for the density of states in amorphous semiconductors:*** *(a) the CFO model with trap states in the overlapping conduction and valence band tails; (b) the Davis-Mott model of an ideal amorphous semiconductor without defects; (c) the Davis-Mott model with defects near the center of the gap; (d) the Marshal and Owen model of a real glass with defect states. Both defect band states within the bandgap and band tail states are trap states. All trap states are shown shaded. Redrawn after [Asal93, Rahm11, KKA+16, LKG+13].*

In order to explain some properties of amorphous semiconductors, three different models have been proposed. The Cohen-Fritzsche-Ovshinsky (CFO) [CFO69] model assumed that the non-crystalline structure would lead to over-lapping exponential band tails of localized states as shown in figure 2.1(a), which extend across the gap. The density of the localized tail states gradually decreases in the gap and this destroys the sharpness of the conduction and valence band edges, which is originated from varied bond length and bond angles. The tails of the valence and conduction bands overlap, arousing an appreciable density of states in the middle

of the gap near E_F, which also means that an electron in a valence band in some region of the material may have a higher energy than an extra electron in an extended state in another part of the material. A redistribution of electrons must take place, forming filled states in the conduction band tail and empty states in the valence band. This results in self-compensation and pinning of the Fermi level close to the middle of the gap where the total density of states is near its minimum. Although the observed electrical properties of amorphous chalcogenides exhibit the pinning of E_F over a wide temperature range, the high transparency of amorphous chalcogenides below a well-defined absorption edge is in contradiction to this model, which hints that the extent of tailing in chalcogenides is rather limited [Kirk73].

Davis and Mott [MD79] proposed a band model with rather narrow tails of localized states in the mobility gap. An ideal amorphous semiconductor would be expected to have a density of states in figure 2.1 (b) if all bonds are saturated and there are no long-range fluctuations, which is the simplified Davis and Mott model without defects. But real amorphous materials always contain point defects or dangling bonds introduced by impurities or microvoids, which lead to localized states within the bandgap. They could act as both deep donors and acceptors, single and double occupancy conditions leading to two bands separated by an appropriate correlation energy or Hubbard U with E_F lie between them, shown in figure 2.1 (c).

Experiments such as luminescence, photoconductivity and drift mobility measurements have indicated that there exists various localized states in the gap. They are split off from the tail states and are located at well-defined energies in the gap, the nature of those localized states is not always clear. Marshall and Owen [MO71] proposed a model showing bands of donors and acceptors in the upper and lower halves of the mobility gap. It makes it clear that the density of states of a “real” amorphous semiconductor does not decrease monotonically into the gap, but shows many peaks which can be well separated from each other, shown in figure 2.1 (d).

Therefore, there are three basic channels for conduction in amorphous semiconductors: extended state conduction above a mobility edge (i.e. band transport); hopping conduction in localized states near the mobility edge and in localized states around the Fermi level.

2.1.2 AC Conductivity

The AC conductivity is composed of a direct current contribution and a delayed polarization contribution, namely: $\sigma_{AC}(\omega) = \sigma_{DC} + \sigma(\omega)$. The first term describes loss due to collision of electrons with other electrons and atoms and the second term is called the polarization conductivity, which denotes loss due to bound charges. Bound charges should have no losses under a DC electric field. However, some bound charges can follow the applied electric field below microwave frequency and cause conduction current giving rise to energy loss, i.e. $\sigma(\omega) = \omega\varepsilon_0\varepsilon_2(\omega)$. At DC fields there is only the contribution from free charges while at AC fields the energy loss will be both due to free and bound charges. Both of the DC and AC conductivity are supposed to be temperature dependent.

In addition, the amorphous chalcogenides have higher carrier densities at higher temperatures. If the transport is entirely due to one type of carriers in extended states, neglecting the weak temperature dependencies of the mobility, the electrical conductivity conforms to the Arrhenius dependence [MD79]:

$$\sigma = \sigma_0 \exp\left(-\frac{E_a}{k_B T}\right) \qquad (2.1),$$

where σ_0 is a prefactor, E_a is the activation energy and k_B is the Boltzmann constant.

Above equations can be applied to amorphous PCMs, which are not intrinsic semiconductors (i.e. they have an equal number of excited electrons and holes) and show p-type conduction. For materials having a Fermi level close to mid gap and comparable mobilities of holes and electrons, the electronic conduction will take part in both bands as a sum of independent contributions from both carriers, where the electron contribution is calculated in an equivalent manner as for holes [Luck12].

Generally, a decrease of conductivity with frequency is associated with a band-type conduction process, while an increasing trend of conductivity with frequency is attributed to a hopping-type conduction mechanism [AS03]. It has been established in numerous experimental studies

that the real part of the AC conductivity in a wide variety of materials, crystalline and amorphous, is dependent on frequency. It varies as $C\omega^s$, where s is a decreasing function of temperature and C is weakly temperature dependent [Mans80, FAH05]. The exponent s is different for the various transport mechanisms, so that from this knowledge, conclusions regarding the underlying transport mechanism can be drawn. Additional information about the localized states can be gained from AC conductivity measurements. Related to models described in section 2.1.1 for the defect states and mobility edges in an amorphous semiconductor, this thesis introduces three mechanisms of conduction in the following subsections.

2.1.2.1 Band Transport

Transport by carriers excited beyond the mobility edges into non-localized (extended) states at E_C or E_V is expected to follow the Drude model [AM76], which ignores any long-range interaction of electron-electron and electron-ion. The mean free time between collisions, τ, is independent of the electron's position and velocity. The average velocity of randomly moving electrons, $\langle \boldsymbol{v} \rangle$, vanishes in thermal equilibrium. An electron will have a velocity $\boldsymbol{v}$ after applying a constant electric field $\boldsymbol{E}$,

$$\langle \boldsymbol{v} \rangle = \langle \boldsymbol{v}_0 \rangle - \frac{e\boldsymbol{E}\langle t \rangle}{m} = -\frac{e\boldsymbol{E}\tau}{m} \tag{2.2}$$

$$\boldsymbol{j} = -ne\langle \boldsymbol{v} \rangle = \frac{ne^2\tau}{m}\boldsymbol{E} \tag{2.3}$$

$$\sigma_0 = \frac{ne^2\tau}{m} \tag{2.4}$$

This is the DC conductivity in the Drude model. The AC conductivity can be measured under application of an external alternating electric field with frequency ω: $\boldsymbol{E}(t) = \boldsymbol{E}_0 e^{-i\omega t}$. Under the AC electric field, the momentum equation of electrons in the presence of collisions with the surrounding ions is:

$$\frac{d\boldsymbol{p}(t)}{dt} = -\frac{\boldsymbol{p}(t)}{\tau} - e\boldsymbol{E}(t) \tag{2.5}$$

Using the ansatz:

$$-\boldsymbol{p}(t) = \boldsymbol{p}_0 e^{-i\omega t} \tag{2.6}$$

leads to

$$i\omega\boldsymbol{p}_0 = \frac{\boldsymbol{p}_0}{\tau} - e\boldsymbol{E}_0 \tag{2.7}$$

$$\boldsymbol{j} = ne\boldsymbol{v} = -\frac{ne\boldsymbol{p}}{m} = \frac{\sigma_0}{1-i\omega\tau}\boldsymbol{E} \tag{2.8}$$

$$\sigma(\omega) = \frac{\sigma_0}{1-i\omega\tau} = \frac{\sigma_0(1+i\omega\tau)}{1+\omega^2\tau^2} \tag{2.9},$$

where τ is the relaxation time. For transport by carriers excited to the extended states near E_C or E_V, it is expected that

$$\mathrm{Re}(\sigma(\omega)) = \frac{\sigma_0}{1+\omega^2\tau^2} \tag{2.10}.$$

The time of relaxation τ in real materials is very short (~10^{-15} s) [MD79] and a decrease in $\sigma(\omega)$ as ω^{-2} (i.e. free carrier intraband absorption) is not expected until a frequency ~10^{15} Hz is reached, therefore $\mathrm{Re}(\sigma(\omega)) = \sigma_0$ when $\omega\tau \ll 1$. The band transport of extended states could dominate in disordered systems at high temperatures.

2.1.2.2 Multiple-Trapping Transport (Trap-limited Band Motion)

In the multiple-trapping transport model, also known as trap-limited band motion, the electronic transport is dominated by free carriers, namely electrons having an energy $E > E_C$ in n-type materials and holes having an energy $E < E_V$ in p-type materials. Free carriers drift through the

specimen after applying an electric field. During the drift process of an electron from one electrode to the other, it might be captured and released several times. Hence, this model is a band transport interrupted by multiple capture and release processes. Figure 2.2 shows the multiple trapping transport process of a free electron being trapped from the conduction band. Empty trapping centers in the bandgap capture free carriers from the band. The electron is localized and does not contribute to the electronic conduction, until it is thermally released back to the conduction band with the activation energy E_a. These multiple trapping and release processes hamper the electronic transport, since the electron does not contribute to the electronic conductivity while occupying a localized defect state. Therefore, the conductivity from the multiple trapping transport model decreases in general with increasing trap state density.

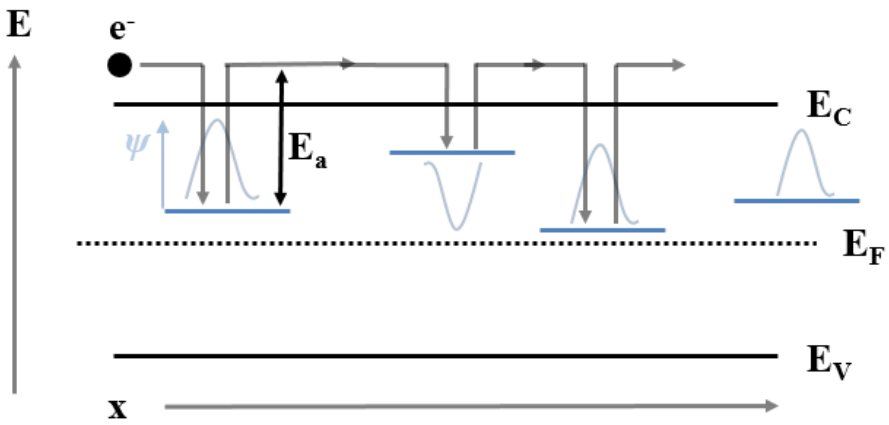

Figure 2.2 ***Multiple-trapping transport model.*** *E_a is the activation energy for electron hopping from a trap state to the band. The localized states in the bandgap trap free carriers from the band, because of which the conductivity is hampered by multiple capture and release processes. If multiple trapping is the main transport channel, the conductivity decreases generally with an increasing number of trap states due to a higher rate of capture processes. (Redrawn after [Luck12])*

2.1.2.3 Hopping Transport (Tunneling between Localized States)

In addition to the transport in the extended states, charge carriers can also conduct by hopping from one localized site to another. Hopping carriers are trapped and detrapped among localization states with the assistance of phonons, instead of being thermally released back to the band. The hopping process of electrons in a semiconductor is shown in figure 2.3. This

transport channel is expected to be dominating at low temperatures, since the activation energy for hopping W is much lower than that for multiple trapping activation energy E_a. There are two types of hopping conduction, i.e. nearest-neighbor hopping near the band tails [KK58, MA60] and variable-range hopping around the Fermi level [Mott69, Schm68].

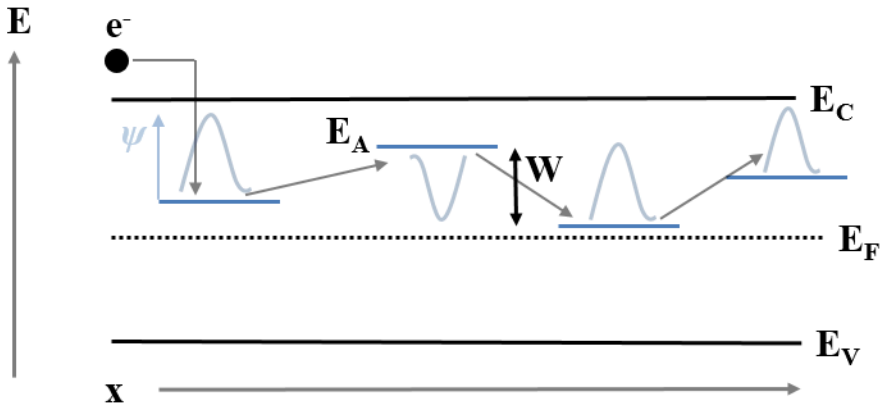

Figure 2.3 ***Hopping transport model****, i.e. carriers jump from trap to trap. It is expected to be the main transport channel at low temperatures. The conductivity increases with increasing number of trap states because the hopping probability increases. (Redrawn after [Luck12])*

In compensated semiconductors, there are a few acceptors in n-type semiconductors and a few donors in the p-type semiconductors near band tails. Electrons hop between these spatially fluctuated distributed levels by emitting or absorbing phonons. This hopping is most probable between nearest neighbors, hence it is called nearest-neighbor hopping. The hopping takes place at low trap concentrations, leading to the following relation for the conductivity [Mori99]:

$$\sigma = \sigma_0 \exp\left(-\frac{\gamma}{\alpha N_0^{1/3}}\right) \tag{2.11}$$

where N_0 is the concentration of randomly distributed trap sites, σ_0, the pre-exponential factor, is concentration independent, α is the localization radius and γ is a numerical coefficient. In the case that the electronic transport is governed by the nearest-hopping processes, a higher number of trap states leads to an increasing conductivity.

In amorphous semiconductors, variable-range hopping conduction occurs through unoccupied localized states near the Fermi level, when the density of states at the Fermi level is finite. According to Mott's law [Mott68], the variable-range hopping shows a characteristic temperature dependence: $\ln\sigma \propto T^{-1/4}$. The Fermi level of chalcogenides is located near mid-gap and appears to be pinned there over a wide temperature range. This gives the major contribution to the current at sufficiently low temperatures. The average hopping distance decreases with increasing temperature. As a higher thermal energy is needed to populate localized states, hopping in the tail states generally occurs at a higher temperature than hopping in defects around E_F.

2.2 Dielectric Function

The dielectric function is a complex quantity, having $\varepsilon_r(\omega) = \varepsilon_1(\omega) + i\varepsilon_2(\omega)$. The real part of the dielectric function, $\varepsilon_1(\omega)$, reveals the energy storage capacity of a material by the polarization of the molecules, while the imaginary part, $\varepsilon_2(\omega)$, reveals the energy dissipation in the medium. They are connected with each other through the Kramers-Kronig relation [Basu05, AS97, Roes65]:

$$\varepsilon_1(\omega) - 1 = \frac{2}{\pi} PV \int_0^\infty \frac{x\varepsilon_2(x)}{x^2 - \omega^2} dx \qquad (2.12),$$

$$\varepsilon_2(\omega) = -\frac{2\omega}{\pi} PV \int_0^\infty \frac{\varepsilon_1(x)}{x^2 - \omega^2} dx + \frac{4\pi\sigma_{DC}}{\omega} \qquad (2.13),$$

where σ_{DC} is the DC conductivity, and the symbol PV denotes the Cauchy principal value of the integral that follows.

The static dielectric constant, ε_{st}, is the dielectric constant under DC electric field or at very low frequency, i.e. $\varepsilon(\omega \to 0)$. It relates to the electronic dielectric constant ε_∞, by [LM70]:

$$\begin{aligned}\varepsilon_{st} &= \int_0^{\infty} \frac{\varepsilon_2(\omega)}{\omega} d\omega \\ &= \int_0^{i.r.} \frac{\varepsilon_2(\omega)}{\omega} d\omega + \int_{i.r.}^{\infty} \frac{\varepsilon_2(\omega)}{\omega} d\omega \\ &= \int_0^{i.r.} \frac{\varepsilon_2(\omega)}{\omega} d\omega + \varepsilon_{\infty}\end{aligned} \qquad (2.14),$$

where the upper limit of the integration (i.r.) means frequencies in the near infrared, beyond the frequencies at which absorption due to the excitation of phonons occurs but below the frequencies at which absorption due to the electronic transitions begins. The ε_∞ in the thesis is defined as the dielectric constant at 0.05 eV, which is above the highest phonon frequency but below the optical bandgap. It arises from the interaction of the radiation field with the bound electrons. The gap between the static dielectric constant and the electronic contribution $\Delta\varepsilon = \varepsilon_{st} - \varepsilon_\infty$, measures the integrated strength of the absorption due to the excitation of phonons.

The dielectric function of a system is mainly concerned with the response of electric polarization as a function of the frequency. The polarization is caused by the movement of electrons or ions or molecules from their equilibrium positions. The total polarization in amorphous materials consist of electronic, ionic and dipolar contributions, which are frequency dependent. Interfacial polarization can be excluded in amorphous chalcogenides because the glasses do not exhibit any microstructure.

2.2.1 Polarization Mechanisms

Polarization arises when a positive charge (e.g. ion) and a negative charge (e.g. electron) in a material leave their equilibrium positions and separate from each other. The polarization density ***P*** of a substance is its net electric dipole moment per unit volume. The charge density vector ***D*** is the sum of the effect of the applied field ***E*** and the polarization. Under the electric field of an electromagnetic radiation, there is:

$$\boldsymbol{E} = \boldsymbol{E}_0 \cos(\omega t) \tag{2.15}$$

$$\boldsymbol{D} = \varepsilon_0 \boldsymbol{E} + \boldsymbol{P} \tag{2.16}$$

$$\boldsymbol{D} = \varepsilon \boldsymbol{E} = \varepsilon_0 \varepsilon_r \boldsymbol{E} \tag{2.17}$$

Then,

$$\boldsymbol{P} = (\varepsilon_r - 1)\varepsilon_0 \boldsymbol{E} \tag{2.18},$$

where ε_0 is vacuum permittivity and ε_r is the relative permittivity.

The dielectric function $\varepsilon_r(\omega)$ connects the electric-field amplitude $\boldsymbol{E}_0$ of an electromagnetic wave of the frequency ω, to the complex amplitude of the polarization wave $\boldsymbol{P}_0$ induced in the solid. The dipole rotates to align with the applied AC electric field. Energy is lost through the generation of heat. The degree of phase difference between the dipole and the incident electric field and the ensued losses determine the imaginary part of the permittivity. The larger the imaginary part, the more energy is dissipated through motion, and the less energy is available to propagate past the dipole.

There are four polarization mechanisms that contribute to the relative permittivity of a material: electronic polarization, ionic polarization, dipolar polarization and interfacial polarization. The net polarizability of a solid will be sum of these four polarizabilities. The masses of the entities to be displaced in the aforementioned mechanisms are getting larger from electronic to ionic to dipolar polarization.

2.2.1.1 Electronic Polarization

Electronic polarization (also known as atomic polarization) is present in all materials, because the individual ions or atoms in a molecule are polarized by the field. It involves the separation of the center of the electrons cloud around an atom with respect to the center of its nucleus

under electric field. This polarization is the fastest and can typically follow the electric field at frequencies between 10^{13} - 10^{15} Hz.

2.2.1.2 Ionic Polarization

Ionic polarization exists in solids with ionic bonding which have dipoles. The net dipole moment arises due to the small displacement of ions from their equilibrium positions with an external electric field. Ionic polarizability exists whenever the substance is either ionic, as in NaCl, or dipolar, as in H_2O, because in each of these classes there are ionic bonds present. But in substances in which such bonds are missing, such as crystalline Si and Ge, ionic polarizability is absent. The ionic polarization is slower than the electronic polarization and typically occurs at frequencies between 10^9 - 10^{13} Hz.

2.2.1.3 Dipolar Polarization

Permanent dipoles in polar molecules are randomly distributed due to thermal randomization, which rotate in the direction of applied field and produce dipolar polarization (also known as orientation polarization), which occurs below 10^9 Hz.

2.2.1.4 Interfacial polarization

Interfacial polarization (also known as space charge polarization) occurs when there is an accumulation of charge at an interface between two regions within a material or between two materials, such as the grain boundaries and electrode-material interface. As a result, interfacial polarization is usually observed in polycrystalline solids. This type of electric polarization is different from orientation and ionic polarization because instead of affecting bound positive and negative charges in ionic and covalent bonded structures, interfacial polarization also affects free charges as well. The insulating properties of dielectric materials cause a charge imbalance, but the mobile charges will migrate over to maintain the charge neutrality, hence produce the interfacial polarization. Those charge dipoles align under an external field below 10^3 Hz.

The Maxwell-Wagner [SK03] polarization, occurs either at inner dielectric boundary layer on a mesoscopic scale, or at the external electrode-sample interface on a macroscopic scale. In both

cases this leads to a separation of charges (such as through a depletion layer). The charges are separated over a considerable distance (relative to the atomic and molecular sizes), and the contribution to dielectric loss can therefore be orders of magnitude larger than the dielectric response due to molecular fluctuations.

2.2.2 Dielectric relaxation

Dielectric relaxation refers to the momentary lag in the dielectric constant of a material, which is caused by the delay of molecular polarization with respect to an external, oscillating electric field in a dielectric medium. Debye relaxation [Deby13] is an ideal model of relaxation response of non-interacting population of dipoles under an alternating external electric field, which can be expressed as a function of the frequency:

$$\varepsilon(\omega) = \varepsilon_{\infty} + \frac{\Delta\varepsilon}{1 + i\omega\tau_D} \tag{2.19},$$

where τ_D is the characteristic relaxation time. Dipolar polarization and interfacial polarization are dielectric relaxation processes, while ionic and electronic polarization behave as resonance or oscillator, which are lossless processes.

Some spurious effects can also give similar relaxation effect. Interfacial polarization is defined as the phenomenon in which the charge carrier, such as electrons or ions, accumulates or becomes depleted at the interface between the specimen and the electrode. This phenomenon occurs usually under “blocking” or “partially blocking” electrodes, where the charge transport in the specimen cannot continue at the electrode. In other words, charges are neither supplied to nor leave the solid. As a result of the interfacial polarization, the apparent DC conductivity increases and the dielectric constant decreases with increasing frequency.

2.2.3 Clausius-Mossotti Relation

The Clausius-Mossotti relation [Bött52] correlates the dielectric constant ε_r of a material with the atomic or molecular polarizability α of its constituent atoms or molecules or a homogeneous mixture thereof.

$$\frac{\varepsilon_r - 1}{\varepsilon_r + 2} = \frac{\rho}{3\varepsilon_0 \sum_i n_i m_i} \sum_j n_j \alpha_j \tag{2.20}$$

where ε_r is the relative permittivity, ε_0 is the vacuum permittivity, m_i is the atomic weight, n_i is the element density and α_i is the polarizability of each element. It is the way to bridge the gap between a directly-observable macroscopic property (ε_r) and a microscopic molecular property (α_i). This relation can be used to fit the ε_∞ values of amorphous PCMs by a sum of constant bond polarizabilities [SKW+08].

2.3 Born Effective Charge

The Born effective charge (Z^*) is referred to as the coefficient of proportionality between a change in macroscopic polarization in one direction caused by an atomic displacement in the perpendicular direction under conditions of zero external field. It is often used for quantifying the coupling between optical phonons and electric fields, which is responsible for the LO-TO optical phonon splitting in polar crystals. The following will introduce how to derive the Born effective charge from macroscopic property.

As is well known that, the electric susceptibility χ_e is defined as the constant of proportionality relating an electric field $\boldsymbol{E}$ to the dielectric polarization density $\boldsymbol{P}$:

$$\boldsymbol{P} = \varepsilon_0 \chi_e \boldsymbol{E} \tag{2.21}.$$

With equation (2.18), one gets the relation between the susceptibility and the relative permittivity ε_r:

$$\chi_e = \varepsilon_r - 1 \tag{2.22}.$$

With the harmonic approximation, the dielectric susceptibility χ_e of a polar (IR active) phonon is a Lorentz oscillator [DG02]:

$$\chi_e(\omega) = \frac{\Delta\varepsilon\Omega_0^2}{\Omega_0^2 - \omega^2 - i\gamma\omega} \tag{2.23}$$

where Ω_0 is the phonon resonance frequency, γ is its inverse lifetime (or damping) and $\Delta\varepsilon$ is its contribution to the dielectric constant. The numerator of equation (2.23) is related to the transverse effective charge q_T involved in the vibration:

$$\Delta\varepsilon\Omega_0^2 = \frac{q_T^2 N}{\varepsilon_0 \mu V} = \Omega_p^2 \tag{2.24}$$

where Ω_p is the plasma frequency, N/V being the density of oscillators, ε_0 the vacuum permittivity, and μ a reduced mass. Generally the plasma frequency can be experimentally determined from the real part of the optical conductivity σ_1:

$$\Omega_p^2 = \frac{2}{\pi\varepsilon_0}\int_{\omega_1}^{\omega_2} \sigma_1(\omega) d\omega \tag{2.25}$$

There are limits in equation (2.25), which includes only the area under the phonon response, and the free carrier or other electronic contributions must be subtracted from σ_1. Supposing that all n_k atoms of the same species (mass m_k) have the same dynamical charge, the Born effective charge Z_k^* of atoms k is related to the optical conductivity through [Scot71, GL97]:

$$\sum_k \frac{n_k Z_k^{*2}}{m_k} = \frac{2V}{\pi}\int \sigma_1(\omega) d\omega \tag{2.26},$$

where V is the volume occupied by all atoms in the left hand side summation. The Born effective charge also respects charge neutrality:

$$\sum_k n_k Z_k^* = 0 \tag{2.27}.$$

It is possible to fully determine the Born effective charges in isotropic binary compounds with equations (2.25) and (2.26). In ternary materials, one has to fix the value of the Born effective charge of one of the atomic species firstly with educated experience.

Experimental Methods

The dielectric properties of amorphous PCMs and other ordinary chalcogenides will be studied in this work by the combination of AC electrical measurement, impedance spectroscopy and FT-FIR spectroscopy. Those measurements spread from low frequency (0.5 Hz – 186.2 Hz), over radio waves (9 kHz – 3 GHz), to infrared region (0.6 THz – 360 THz). Results obtained from the impedance spectroscopy, together with those from AC electrical measurement and FT-FIR spectroscopy, will give a better understanding of these solids. The value of ε_{st} derived from the three methods will be corroborated by each other.

The AC electrical measurement relies on a digital lock-in amplifier (DLIA) in the PPMS, and the impedance measurement employs a Vector Network Analyzer (VNA) as the core setup. The operating principles of the above mentioned three techniques, involving the DLIA, the VNA and the FT-IR, will be introduced briefly in this chapter.

3.1 Techniques for Measuring the Dielectric Function

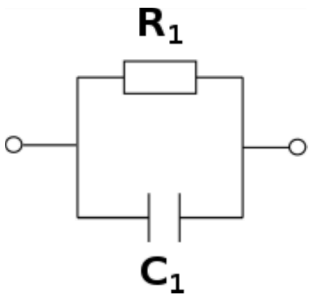

Figure 3.1 ***Ideal equivalent circuit of the PCMs thin film with electrodes as used in the electrical measurement.*** *R_1 and C_1 refer to the resistance and the capacitance of the sample, respectively.*

Impedance spectroscopy enables us to study dielectric properties of the amorphous PCMs in radio frequencies. Those samples employ the plate-capacitor-like structure (i.e. electrode / dielectric / electrode sandwiched structure). The real part and the imaginary part of the conductivity are normally determined by regarding the sample as a resistor and a capacitor in

parallel as shown in figure 3.1 [BM05, BCS88]. The equivalent circuit consists of an ohmic resistor $R_1 = d/A\sigma$ and a capacitor $C_1 = (\varepsilon_0\varepsilon_{st}A)/d$, where A is the cross-sectional area, d is the thickness, σ is the conductivity, ε_{st} is the static dielectric constant of the film, and ε_0 is the vacuum permittivity. The transition frequency f_{RC} between the resistive and the capacitive region

$$f_{RC} = (2\pi R_1 C_1)^{-1} = \frac{\sigma}{2\pi\varepsilon_0\varepsilon_{st}} \tag{3.1}$$

is defined by $R_1 = |Z_C| = (\omega C_1)^{-1}$ and can be observed in the impedance measurement. Above this frequency, the capacitor C_1 becomes dominant and ε_{st} can be determined. Note that f_{RC} is independent of the aspect ratio and depends *only* on the conductivity and the dielectric function of the material under investigation. Experimental difficulties arise when the conductivity of amorphous PCMs is high.

It is well known that the conductivity of amorphous PCMs at room temperature is of the order of magnitude of 10^{-3} S/cm and the optical dielectric constant is about 15 [SKW+08]. *The static dielectric constant* should be larger than *the optical dielectric constant*, if active infrared phonons are found. Supposing the ε_{st} of amorphous PCMs is 30, the relation between the f_{RC} and the conductivity is plotted in figure 3.2, according to equation (3.1). The f_{RC} of the amorphous PCMs at room temperature is between 10^7 Hz and 10^8 Hz. Hence, the impedance measurement system with a VNA covering a broad frequency range (9 kHz – 3 GHz) is desirable.

Figure 3.2 ***Relation between the transition frequency f_{RC} and conductivity*** *of a solid with the dielectric constant about 30.*

Furthermore, it is possible to measure the dielectric permittivity of the amorphous PCMs below kHz, when the conductivity decreases to 10^{-9} S/cm. It can be realized in the cryostat of a Physical

Property Measurement System (PPMS), because the conductivities of the amorphous PCMs drop rapidly at low temperatures. The PPMS offers AC electrical measurement between 0.5 Hz and 186.2 Hz by the Digital Lock-in Amplifier (DLIA) down to 4 K and even lower. It is unnecessary to cool below 4 K and the cooling rate becomes much slower than that above 4 K. Therefore, the capacitive behavior of the amorphous PCMs will be observed under 186.2 Hz above 4 K.

In addition, the FT-IR spectroscopy is extended to the far-infrared range to cover the contribution of all infrared active phonons to derive the static dielectric permittivity.

Three kinds of techniques are combined in this work to study the dielectric function in different frequency regions as summarized in figure 3.3. The working principles of these setups are introduced in detail in section 3.2, 3.3 and 3.4, respectively.

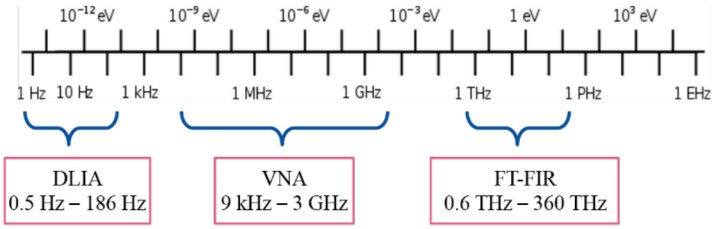

Figure 3.3 ***The measurement range of three methods,*** *i.e. AC electrical measurement by DLIA, impedance spectroscopy by VNA and optical spectroscopy by FT-FIR. The static dielectric permittivity* ε_{st} *of the amorphous chalcogenides will be determined.*

3.2 Low Frequency Method

3.2.1 DLIA in the ETO system

This low frequency measurement system is based on the principle of DLIA [BIS+12] to measure small capacitance with high sensitivity. DLIA uses the technique of phase-sensitive detection to single out the component of the signal at the input reference frequency and phase. A dual-phase lock-in can measure the "in-phase" component (X) and the "quadrature" component (Y).

The signal vector magnitude of resitance (R), phase angle (θ) and noise of the input signal in the frequency range between 0.5 Hz and 186.2 Hz are given in the results. The phase (θ) between the signal and the lock-in reference is determined by $\tan^{-1}(Y/X)$. The voltage drop across the sample can be considered as a superposed sinusoidal of excitation frequency f, also $2f$ (the second harmonic), $3f$ (the third harmonic) and so on. The second and third harmonic strength are given as a relative number dB to the basic frequency f. The DLIA only analyses for the first harmonics.

3.2.2 Two-Wire Mode

In this work, two-wire sample-mounting configuration using a programmable-gain amplifier and a high-impedance amplifier was applied for the high impedance measurement. In the two-wire mode the ETO system applies a voltage excitation across the sample and uses a sensitive ampere meter to measure the current through the sample, shown in figure 3.4. The current input range of the ampere meter of the two-wire mode is limited to 250 nA. If the current is saturated, the ampere meter of the ETO-option will not present an error message. Therefore the second and third harmonics of the measured response are taken as a criteria of the measurement quality. For a good measurement the second and third harmonic contribution should be less than -50 dB.

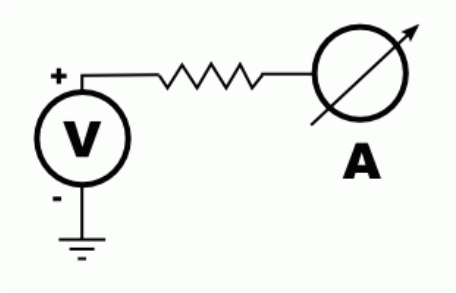

Figure 3.4 ***Equivalent circuit of the two-wire mode in the ETO system.*** *The high impedance mode can operate as an AC voltage source and a nano-ampere meter, allowing for two-wire measurements of sample resistance up to 5 GΩ. Reprinted from [PPMS11].*

In the two-wire mode, the bottom and top electrodes of the DLIA samples are bonded to the terminals “I+” and “V-”, respectively, of the channel 1 on the sample puck shown in figure 3.5.

The channel 2 has the same function as the channel 1. Superior contacts are formed by the wire bonder (TPT HB06). 25 μm gold and aluminum wires are available for bonding. Therefore lead and contact resistance are ignored because they are much less than the sample resistance.

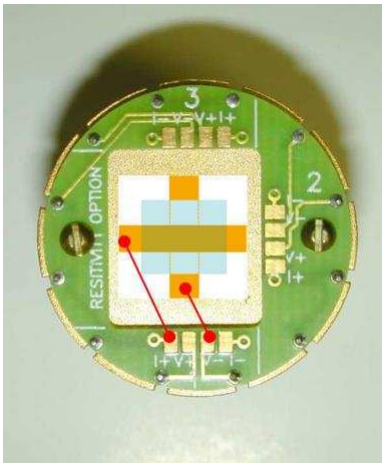

Figure 3.5 ***A sample is bonded in the two-wire mode on a sample puck.*** *Red lines represent the bonding wire Au or Al.*

The upper limit of the ranges in the voltage amplifier varies from 0.5 V to 20 V, and the input minimum voltage is 10 mV. The current that can be perceived by the sensitive ampere meter ranges from 1.3 nA to 250 nA. The high impedance mode of the ETO system is typically used to perform measurements on samples with resistance above 2 MΩ, but below 5 GΩ, which is limited by leakage currents on PC boards.

3.3 Radio Frequency Method

The radio frequency measurement system consists of a VNA (R&S ZVL3), a probe station (H150, Signatone), including an optical microscope and a modified sample holder, a pair of Z-probes (no. 40 K3N GSG 150), handformable microwave cables (HUBER+SUHNER) and Bayonet Neill-Concelman (BNC) connectors. The characteristic impedance of all elements in the system is 50 Ω. The core of the whole system is the VNA, which works between 9 kHz and 3 GHz. A schematic diagram of the whole measurement system is presented in figure 3.6. Z-probes are installed on the contact heads. The metal between the capacitor and the contact head

is called waveguide. The microwave cable is one kind of coaxial cable, which has at least four layers, consisting of a single metal conductor in the center and an insulator layer between the center conductor and a braided metal shield, and an insulating outer jacket. The metal shield blocks all outside signal interference, hence the core can be used as a transmission line for radio frequency signal. The operating frequency of the microwave cables is up to 33 GHz, which covers the VNA working frequency range.

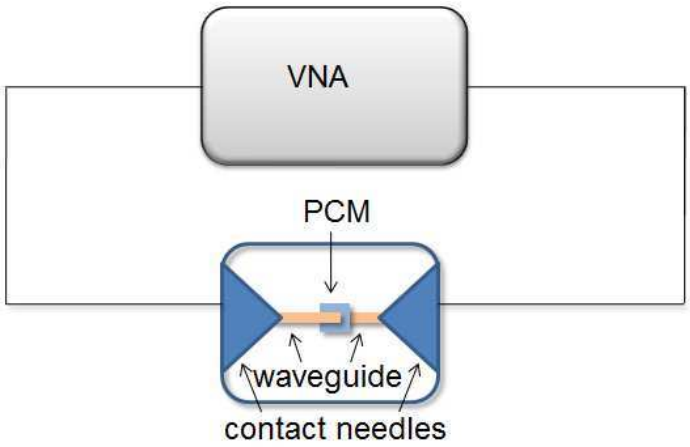

Figure 3.6 ***A schematic diagram of the measurement system*** *with the contact head in blue, the waveguide in orange and the PCM layer in light blue. The investigated sample is located between the two Z-probes. Hence, the sample is connected to the VNA by coaxial cables, BNC Connectors and the Z-probes. Reprinted from [Schl12].*

3.3.1 VNA Basics

As illustrated in figure 3.7, the source of a VNA stimulates a sine wave to a device under test (DUT). The source will rapidly sweep across frequencies to collect the frequency response of the DUT. Each port of the VNA has a directional coupler to separate the incident signal from the reflected signal passing through the test port. There is also a receiver at each port to capture waves, allowing the instrument to measure the phase and magnitude of incident and reflected waves independently.

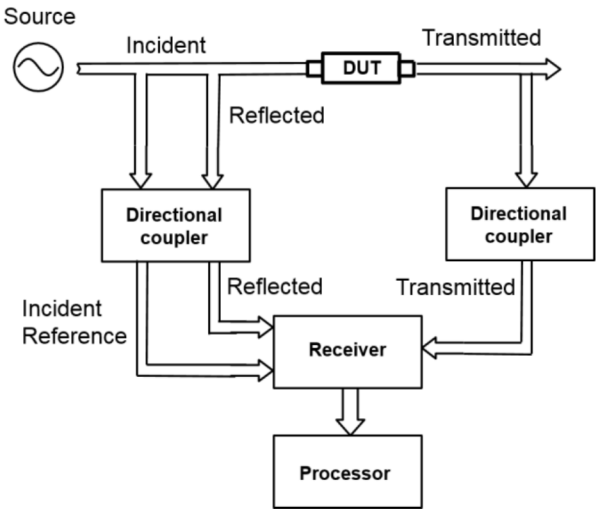

Figure 3.7 ***Generic VNA block diagram****, including four major signal-processing sections: the source for stimulus, the directional coupler (signal-separation devices), the signal receiver and the signal processor. Redrawn after [Agil].*

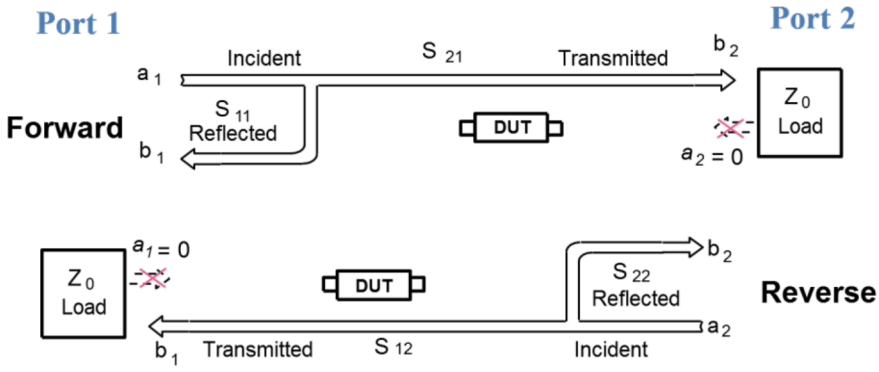

Figure 3.8 ***Schematic diagram of the definition of S-parameters.*** *a_1, a_2 are the incident voltage traveling wave from port 1 and port 2, respectively. b_1, b_2 are the reflected voltage traveling wave at port 1 and port 2, respectively. S_{11} is the forward reflection coefficient (input match), S_{22} is the reverse reflection coefficient (output match); S_{21} is the forward transmission coefficient (gain or loss), S_{12} is the reverse transmission coefficient (isolation). Redrawn after [Agil].*

VNA generally measures the scattering parameters (S-parameters) as a function of the frequency between ports in a multi-port network. In a two-port case, the reflection and transmission signals are described in the form of S_{11}, S_{22}, S_{12}, S_{21}, which can be mathematically

converted to complex impedance parameters in the next section. The impedance spectrum can be presented as: (1) Nyquist diagram, where the imaginary part of the impedance is plotted as a function of its real part; (2) Bode diagram, where the impedance magnitude or phase is plotted as a function of the frequency.

Using a 2-port system the reflection S-parameters S_{11}, S_{22} as well as the transmission S-parameters S_{12}, S_{21} are obtained. As can be seen in figure 3.8, S-parameters are formally defined by the following equations:

$$S_{11} = \left.\frac{b_1}{a_1}\right|_{a_2=0} \qquad S_{21} = \left.\frac{b_2}{a_1}\right|_{a_2=0}$$

$$S_{12} = \left.\frac{b_1}{a_2}\right|_{a_1=0} \qquad S_{22} = \left.\frac{b_2}{a_2}\right|_{a_1=0} \qquad (3.2),$$

S-parameters are complex numbers, including not only the magnitude, but also phases. The forward S-parameters S_{11} and S_{21} are determined by the incident, reflected and transmitted voltage signals when the other output is terminated with a perfect load that equals the characteristic impedance of the test system. This condition guarantees no reflection from that port, i.e. the output of the port is $a_2 = 0$. S_{11} is the input complex reflection coefficient and S_{21} is the forward complex transmission coefficient. In a similar way, S_{22} and S_{12} measurement can be made by placing the source at port 2.

Table 3.2 Basic settings of VNA parameters [Schl12].

Sweep type	**Sweep range**	**Number of points**	**Source power**	**Measurement bandwidth**
Logarithmic frequency sweep	9 kHz – 3 GHz	500	-10 dBm	100 Hz

The VNA is set to the configuration shown in table 3.2. Reduced signal levels can lead to a susceptibility to noise and degraded low frequencies data because the coupler loss is high at low frequencies. In principle, the source power should be set as high as possible to achieve the

lowest uncertainty at a given intermediate frequency (IF) bandwidth. However, it needs to ensure that the PCMs are not switched. Therefore, a power of -10 dBm, i.e. 0.1 mW was chosen. The decrease of the IF bandwidth will reduce the noise but increases the measurement time. The bandwidth of 100 Hz is an ideal compromise.

3.3.2. Derivation of Impedance from S-parameters

There are two ports available for the VNA used in this work. The impedance measurements can be done by two ports or only one port. The impedance and then the dielectric function of investigated materials can be determined by both methods.

3.3.2.1 Two-Port Measurement

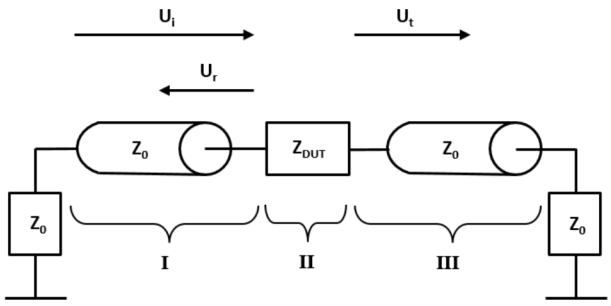

Figure 3.9 ***Equivalent circuit of two-port measurement.*** *U_i, U_r, U_t are the incident, reflected and transmission signals in sequence. U_I, U_{II}, U_{III} are voltages dropped across the left cable, the DUT and the right cable, respectively. Z_0 and Z_{DUT} are the impedance of the system elements and the investigated device, respectively. Redrawn after [Krie10].*

In the two-port case shown in figure 3.9, there are equations [Krie10]:

$$U_I = U_i + U_r \tag{3.3}$$

$$I_I = \frac{U_i}{Z_0} - \frac{U_r}{Z_0} \tag{3.4}$$

$$U_{III} = U_t = I_{III} \cdot Z_0 \tag{3.5}$$

$$U_{II} = U_I - U_{III} = I_{II} \cdot Z_{DUT} \tag{3.6}$$

$$I_I = I_{II} = I_{III} \tag{3.7},$$

where $Z_0 = 50\ \Omega$ is the characteristic impedance of the system elements, including the VNA, the coaxial cables, the contact heads and BNC connectors.

Using equations above, one gets:

$$S_{11} = S_{22} = \frac{U_r}{U_i} = \frac{Z_{DUT}}{Z_{DUT} + 2Z_0} \tag{3.8}$$

$$S_{21} = S_{12} = \frac{U_t}{U_i} = \frac{2Z_0}{Z_{DUT} + 2Z_0} \tag{3.9}.$$

Until now, the relation between S-parameters and the device impedance in two-port measurements has been built up. Hence the complex impedance of the sample Z_{DUT} in two-port measurements can be deduced from the S-parameters by

$$Z_{DUT} = 2Z_0 \frac{1 - S_{21}}{S_{21}} \tag{3.10},$$

or

$$Z_{DUT} = 2Z_0 \frac{S_{11}}{1 - S_{11}} \tag{3.11}.$$

All devices were probed in both reflection (S_{11}, S_{22}) and transmission (S_{21}, S_{12}) modes.

3.3.2.2 One-Port Measurement

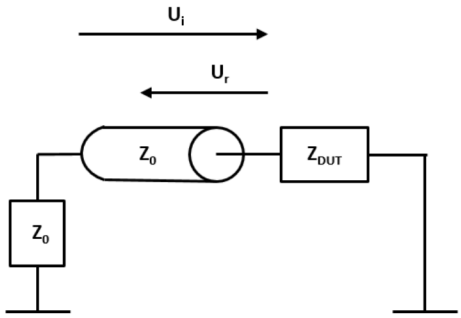

Figure 3.10 ***Equivalent circuit of one-port measurement.*** *U_i and U_r are the incident and reflected signals, respectively. Z_0 and Z_{DUT} are the impedance of the system elements and the investigated device, respectively. Redrawn after [Krie10].*

In the one-port case shown in figure 3.10, there are equations [Krie10]:

$$U = U_i + U_r = I \cdot Z_{DUT} \tag{3.12}$$

$$I = \frac{1}{Z_0}\left(U_i - U_r\right) \tag{3.13}$$

$$S_{11} = \frac{U_r}{U_i} = \frac{Z_{DUT} - Z_0}{Z_{DUT} + Z_0} \tag{3.14}.$$

The relationship between S-parameters and device complex impedance of one-port is given in equation (3.14). And the complex impedance can be further derived from:

$$Z_{DUT} = Z_0 \frac{1 + S_{11}}{1 - S_{11}} \tag{3.15}.$$

Therefore, the impedance spectroscopy of samples can be measured in both configurations of two-port and one-port, and then the dielectric function can be derived. As seen from equation (3.14), the result from reflection measurement is most accurate for DUT impedance near 50 Ω when the one-port DUT is connected to the one port of the VNA. To measure a DUT with impedance very different from 50 Ω, 2-port measurement should be applied. The comparison

of results by these two methods are discussed in chapter 6 with emphasis on the two-port measurements.

3.3.3 Calibration Results

The electromagnetic wavelength at GHz is about 0.3 meter, which is even shorter than the length of coaxial cables used in the measurements. Proper calibration up to GHz before measurements is necessary. The calibration is a procedure integrated in the VNA software instead of a manual process. The TOSM standard, i.e. "Through" ("Thru"), "Open", "Short" and "Match", was chosen. The calibration was done in the ambient environment at room temperature. The deviation of the cold instrument directly after power-up will continuously decrease from 0.05 dB and 2˚ to typically 0.005 dB and 0.1˚ as the instrument is allowed to warm-up for one hour to attain thermal equilibrium [RS17]. Therefore, the setup was warmed up for one hour before starting measurements and it was calibrated every two weeks.

3.3.3.1 Calibration with the CSR-8 Substrate

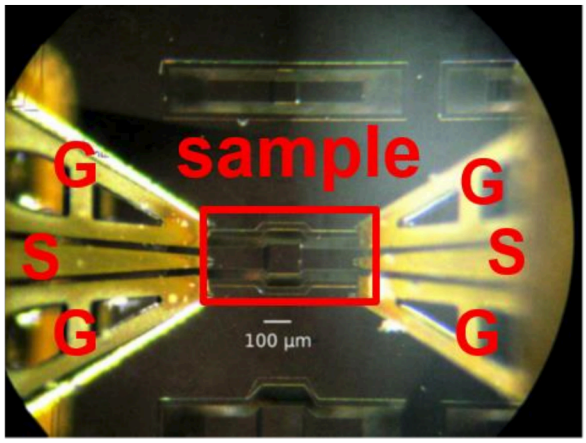

Figure 3.11 ***Z-probes under the optical microscope.*** *Ground, signal, ground needles of Z-probes are labelled with GSG, respectively for short. The signal needles contact with the sample waveguide and the ground needles touch down to the ground plane. The signal transmits from one signal needle to the electrode of the sample and passes through the sample to the signal needle of the other Z probe. All ground needles are connected to the ground. Adapted from [Krie10, CM].*

The pair of Z-probe used in this work is photographed under the optical microscope in figure 3.11. It consists of three needles in sequence as Ground - Signal - Ground (GSG). The planar calibration substrate CSR-8, provided by the manufacturer of the contact heads (Suss Microtec), was adopted to calibrate the measurement system to the end of the probe. TOSM calibration structures are illustrated in figure 3.12. The "Thru" structure belongs to the two-port standard, while other structures "Open", "Short" and "Match" involve only one port. S_{11} equals S_{22} and S_{12} equals S_{21} because the two ports are equivalent with each other.

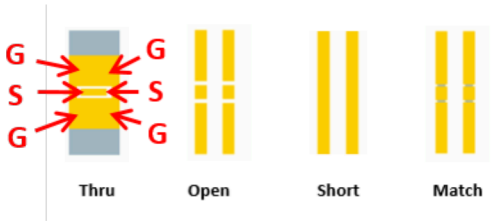

Figure 3.12 ***TOSM calibration structures on the CSR-8 substrate.*** *With the "Thru" structure, two signal tips of Z-probes are short connected. "Open" means there is no connection between the signal tip and ground tips. "Short" denotes the signal tip is short connected to the two ground tips at each port. "Match" represents the signal tip is connected to the ground tips with impedance matching. Adapted from [UMCS].*

In the case of "Thru" calibration, the connection between the two signal needles of Z-probes has a zero impedance. Therefore the magnitude of the reflection S-parameters is zero (i.e. $|S_{11}| = |S_{22}| = 0$) according to equation (3.8), and all the signal should pass through the structure from one port to the other (i.e. $|S_{21}| = |S_{12}| = 1$). In addition, the phase angle of all S-parameters is zero (i.e. $\varphi = 0^{\circ}$).

In the case of "Open" calibration, just as the name "Open" implies, the impedance is infinity. According to equation (3.14), the whole signal is reflected and there is no phase difference between the incident and reflected signal (i.e. $S_{11}| = |S_{22}| = 1$, $\varphi = 0^{\circ}$).

In the case of "Short" calibration, the signal needles of Z-probes are connected to the ground needles, so the signal is completely reflected with a phase jump of 180° (i.e. $|S_{11}| = |S_{22}| = 1$, $\varphi = 180^{\circ}$).

In the case of "Match" calibration, there are a pair of resistors, shown in figure 3.12, between the signal and ground needles of each Z probe. The equivalent impedance of the two paralleled resistors at each port is 50 Ω. Therefore, all signals transmit to the ground and no signal is reflected (i.e. $|S_{11}| = |S_{22}| = 0$).

Deviations from the above ideal expectations due to attenuations and propagation times are corrected after the TOSM calibration. In order to confirm the calibration effect, those four structures on the CSR-8 substrate were re-measured using the impedance measurement system after calibration.

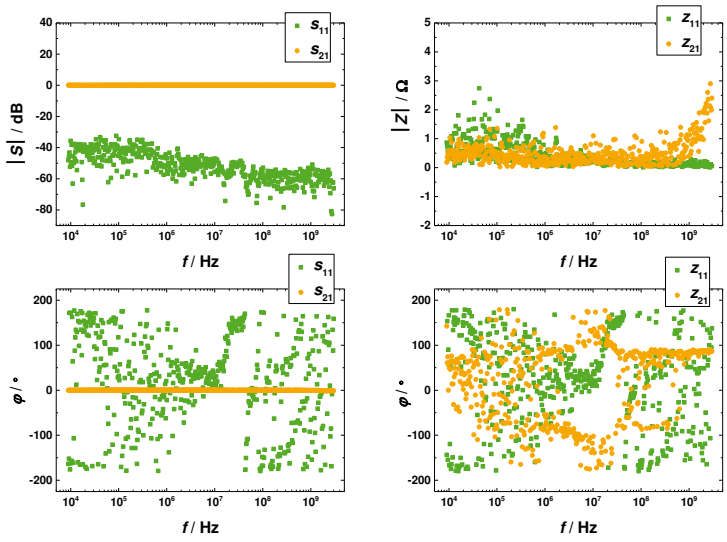

Figure 3.13 ***Impedance measurements on a "Thru" structure of the CSR-8 substrate.*** *From the S-parameters the impedance is calculated and also presented. In green the data determined from the reflectance S-parameters and in orange the data determined from the transmission S-parameters are plotted. The amplitude and the phase angle of S_{21} are 0 dB and 0˚, respectively, as expected and the phase decreases slightly from 0˚ to -1.5˚ at the high frequency end.*

Firstly, measurements were carried out on a "Thru" structure of the CSR-8 substrate. The impedance Z_{11} and Z_{21} are calculated from the reflectance coefficient S_{11} and the transmission coefficient S_{21}, and all are plotted in figure 3.13. The transmission S-parameter S_{21} is around 0

dB as expected, which means that nearly the whole signal gets through from port 1 to port 2. The phase angle maintains at 0˚ and decreases slowly to -1.5˚ at 3 GHz. The impedance derived from S_{21} is around 0.5 Ω, but it increases to 2.5 Ω at the high frequency end because of a phase error. Furthermore, the amplitude of the reflectance coefficient $|S_{11}|$ decreases from -40 dB (i.e. 1%) to -60 dB (i.e. (i.e. 0.1%). The signal is hardly reflected, it is difficult to resolve the phase angle of S_{11} correctly. At the high frequency end, the impedance derived from S_{11} is more accurate than that from S_{21} because there is no phase error in the reflectance measurement.

Secondly, an "Open" structure on the CSR-8 substrate was measured. The results are shown in figure 3.14. The amplitude of S_{11} or S_{22} (i.e. $|S_{11}|$ or $|S_{22}|$) is about 0 dB (i.e. 100%), and the phase angle of S_{11} (or S_{22}) oscillates around 0º, which means that nearly the whole signal is reflected without changing phase. The noise of S-parameters is much less at frequencies higher than 10^6 Hz because the problem of impedance mismatch is decreasing with frequency.

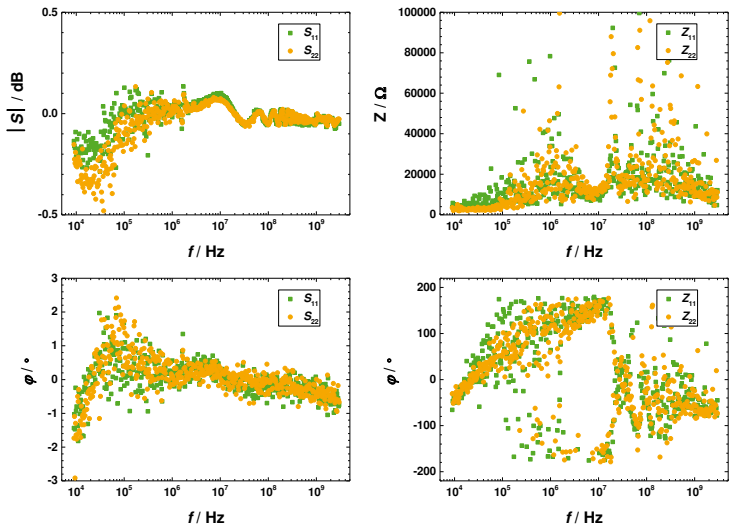

Figure 3.14 ***Impedance measurements on an "Open" structure of the CSR-8 substrate in one-port standard.*** *In green the data determined from the S_{11} and in orange the data determined from S_{22} are plotted. Standing waves formed by the incident and reflected signals are observed in the S-parameters. The amplitude of the reflectance S-parameters are around 0 dB and their phase angles are around 0º as expected.*

Thirdly, measurements were carried out on a "Short" structure of the CSR-8 substrate. The results are shown in figure 3.15. The amplitude of the reflectance S-parameters ($|S_{11}|$ or $|S_{22}|$) oscillates around 0 dB with deviation between ±0.1 dB and its phase angle is distributed between 179˚ and 180˚ as expected. Most of the signal is reflected with a phase jump of 180˚. The impedance determined by S_{11} (or S_{22}) is around 0.2 Ω.

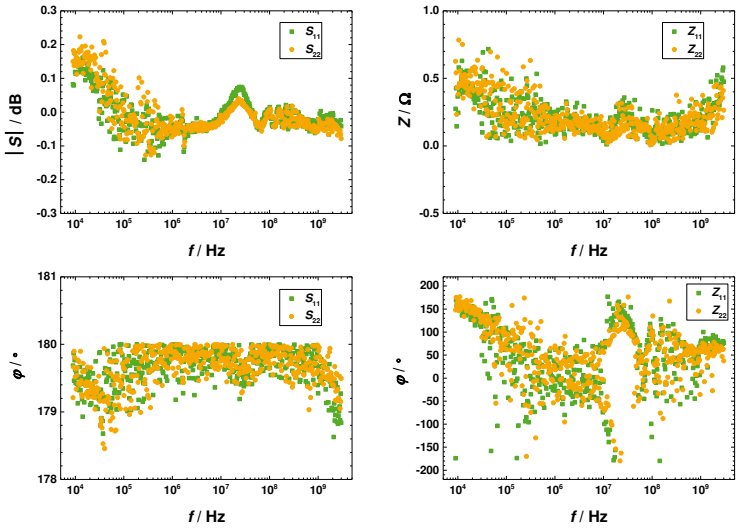

Figure 3.15 ***Impedance measurements on a "Short" structure of the CSR-8 substrate in one-port standard.*** *The color has the same meaning as in figure 3.14. The amplitude of the reflectance S-parameters are around 0 dB and their phase angles are around 180° as expected. Standing waves by the input and reflected signals are observed in the reflectance S-parameters.*

Lastly, measurements were carried out on a "Match" structure of the CSR-8 substrate. The results are shown in figure 3.16. The amplitude of the reflection S-parameters decrease from -40 (i.e. 1%) to -60 dB (i.e. 0.1%) with frequency. There is less noise at the high frequency end because of better impedance matching. It is impossible to obtain the phase angle of reflectance S-parameters correctly, because nearly no reflected signal is detected. The impedance of the "Match" structure determined by the reflectance S-parameters is 50 Ω, which is in line with the expectation.

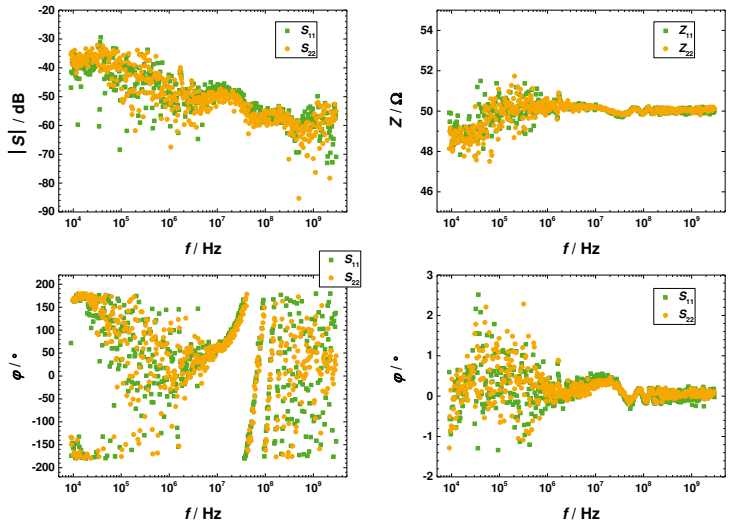

Figure 3.16 ***Impedance measurements on a "Match" structure of the CSR-8 substrate in one-port standard.*** *The color has the same meaning as in figure 3.14. The impedance calculated from the reflectance S-parameters are about 50 Ω as expected. Standing waves are observed in the impedance and their phase angles.*

To sum up, the system after the TOSM calibration is effective for the measurement system. The phase error of the transmission S-parameters increases with frequency exponentially. It is necessary to correct the phase error of S-parameters by multiplying $\exp(i\theta \cdot \Delta f l f)$ after the frequency of 10^8 Hz.

3.3.3.2 Calibration Structures on an Investigated VNA Sample

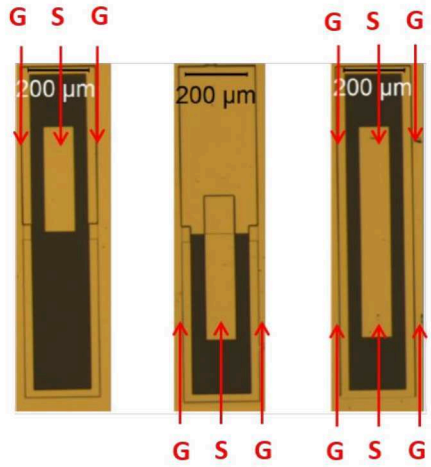

Figure 3.17 ***Calibration Structures on a VNA sample.*** *The label of GSG has the same meaning as in figure 3.11. Calibration structures from left to right in order: "Open", "Short", "Thru". Adapted from [Schl12].*

Figure 3.17 illustrates calibration structures including "Open", "Short", "Thru" on a VNA sample. There are two different composing materials of each calibration structure: one is made out of platinum like the bottom electrode; the other is made out of gold with the same process as the top electrode. In order to evaluate the calibration effect of the CSR-8 substrate for to-be-measured devices, impedance measurements were also carried out on the calibration structures on the VNA sample. The distance between touch-down points of the two contact heads on the calibration substrate is shorter than that on the investigated samples. The varied distance of the waveguide is not included correctly into the calibration process, which contributes to a phase error.

Firstly, the platinum "Thru" structure was measured. The impedance was calculated from S-parameters and shown in figure 3.18. The amplitude of S_{11} ($|S_{11}|$) is about -19.6 dB (i.e. 10.5 %) and the phase angle of S_{11} oscillates around 0º with less noise above the frequency 10^8 Hz. On the contrary, the transmission S-parameters $|S_{21}|$ is about -0.86 dB (i.e. 90.6%). The phase angle of S_{21} scatters around 0˚ and deviates from 0˚ to -5˚ at the high frequency end. The deviation of phase angle is larger than that of the "Thru" structure on the CSR-8 substrate by 3.5º. The varied

distance of two Z-probes between on the CSR-8 substrate and on the VNA sample contributes to the phase error of the transmission S-parameters. The sum of $|S_{11}|$ and $|S_{21}|$ is slightly larger than 1 because of a reasonable amplitude error. Both of the impedance Z_{11} and Z_{21} calculated from S-parameters sustain around 11 Ω, but Z_{21} increases exponentially with frequency up to 15 Ω at 3 GHz due to a phase error.

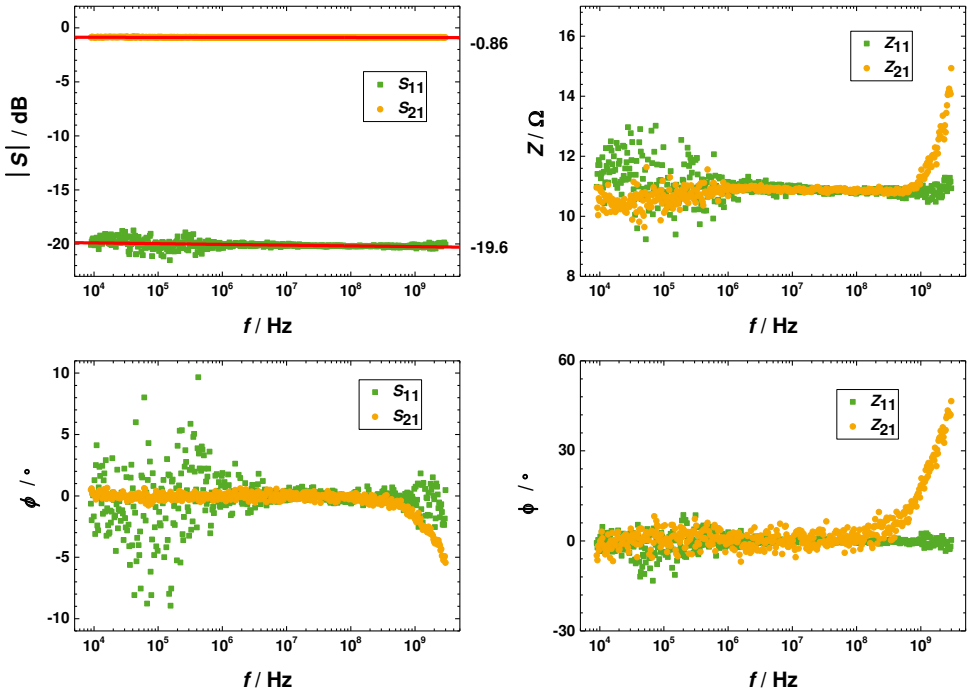

Figure 3.18 Impedance measurements on the platinum "Thru" structure of one investigated sample. S_{11} related parameters are plotted in green and S_{21} related parameters are plotted in orange, with linear fitting data in red. The phase error of S_{21} increases exponentially with frequency, so it becomes more obvious at higher frequencies.

Secondly, measurements were also carried out on a "Thru" structure made out of gold. The amplitude of S_{11} ($|S_{11}|$) is about -32.2 dB (i.e. 2.5 %) and its phase angle oscillates around 0°. On the contrary, the transmission $|S_{21}|$ is close to -0.12 dB (i.e. 98.6 %) with the phase angle around 0°, which deviates to -5° at 3 GHz. The impedance derived from both the reflectance

and transmission S-parameters are around 2 Ω, but Z_{21} increases with frequency up to 9 Ω at 3 GHz.

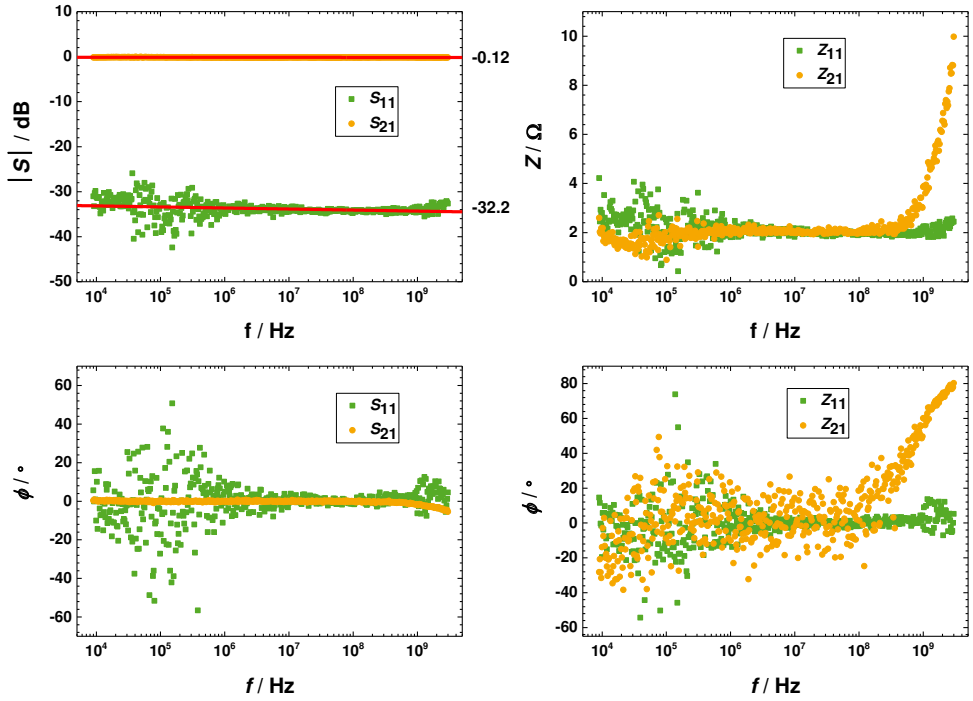

Figure 3.19 ***Impedance measurements on the gold "Thru" structure of one investigated sample.*** *The colors have the same meaning as in figure 3.18. There is more noise of the reflectance S-parameters than that of the transmission S-parameters. A phase error of S_{21} is also observed at the high frequency end. The impedance at frequencies larger than 10^8 Hz deviates from the expectation.*

Thirdly, impedance measurements were carried out on a "Short" structure made out of platinum, shown in figure 3.20. The magnitude of S_{11} is about -1.65 dB (i.e. 82.7%) and its phase angle sustains about 180˚ until 1 MHz and decreases exponentially with frequency to 174˚ at 3 GHz.

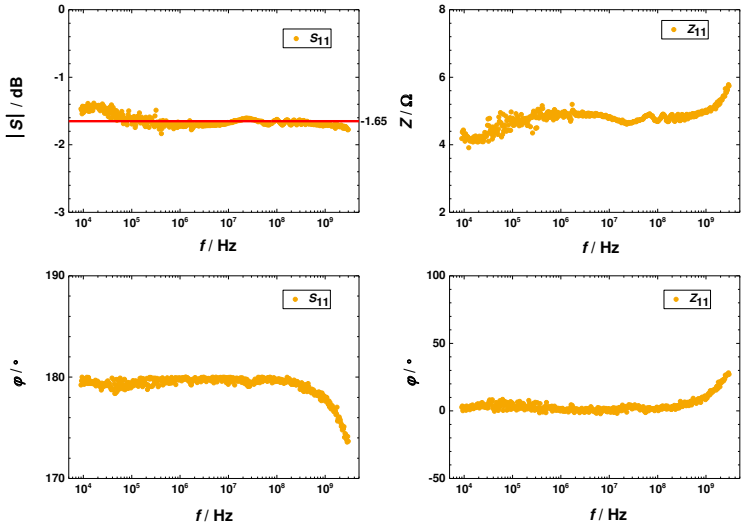

Figure 3.20 ***Impedance measurements on the platinum "Short" structure of one investigated sample.*** *The S_{11} in dB and the impedance determined by S_{11} are plotted along with the frequency.*

From the "Thru" measurements, the transmission S-parameters are more accurate than that of the reflectance S-parameters because of less noise. The phase error of the transmission S-parameters only become obvious above 100 MHz. As the bottom electrode and the top electrode of capacitor devices are made out of platinum and gold, respectively, the impedance of the bottom electrode and the top electrode are not the same because of different conductivities of platinum and gold. The contact resistance of those capacitor devices should be between the resistance of the top electrode and the bottom electrode. It was simulated in the Master thesis of Schlich [Schl12] that the amplitude error of the S parameters cannot change the slope of the frequency dependence of the AC conductivity and the dielectric function, but the phase error of S-parameters do impact the slope of the conductivity and the dielectric function, especially at higher frequencies.

In conclusion, the measurement is only reliable at frequencies below 100 MHz. The transmission S-parameters should be smaller than -0.12 dB. And the reflectance S-parameters should be larger than -32.2 dB and smaller than -1.65 dB.

3.4 Optical Frequency Method

The interaction with light provides a powerful method to probe the electronic and vibrational structure of a solid. The macroscopic optical properties of materials, such as reflectance and transmission are dependent on the complex dielectric function. The FT-IR is a contactless method for determining the dielectric functions of films. With this method the dielectric function of films are deduced from reflectance spectra or transmission spectra with the help of a mathematical algorithm. Hence, the reflectance and transmission spectra of chalcogenides are studied in this thesis. The transmission measurements were conducted by Dr. R.P.S.M. Lobo in the Laboratoire de Physique et d'Étude des Matériaux (LPEM) in Paris. The transmission spectra is more accurate than the reflectance spectra, but its range is limited by the silicon substrate.

3.4.1 FT-IR Reflectance

Reflectance spectra can be measured in the mid-infrared region from 0.05 eV to 1 eV (i.e. 400 cm^{-1} – 8000 cm^{-1}, 12 THz – 240 THz) by a Bruker IFS 66v/s spectrometer with a resolution of 0.24 meV using a globar source. The angle between the incoming beam and the surface normal was kept constant at 10˚. The relative error of the reflectance in the range of the measurement is 0.2%.

It can be seen from figure 3.21 that the reflectance of gold and silver are slightly closer to 1 than that of aluminum above the wavelength of 1 μm. Hence, a gold mirror shown on the left part of figure 3.22 is used as the reference for the light intensity normalization. However, aluminum was chosen as the reflector of investigated samples, shown on the right part of figure 3.22, because aluminum does not diffuse into the PCM layer as gold or silver. A very thin compact layer of aluminum oxide on the surface works as a good anti-diffusion layer. The material under investigation was deposited on an aluminum coated glass substrate to obtain the optimal reflectance spectra [HRC+93, CLS14]. The aluminum layer acts as an ideal reflector in the measurement range. The optical properties of the aluminum thin film have been determined in advance. At the first surface, some of the incident light is reflected, and some transmitted. This transmitted light passes through and some reflected from the rear side back to the first surface.

The rest is reflected, and then bounces back and forth between front and back, with a fraction leaking out of the surface each time.

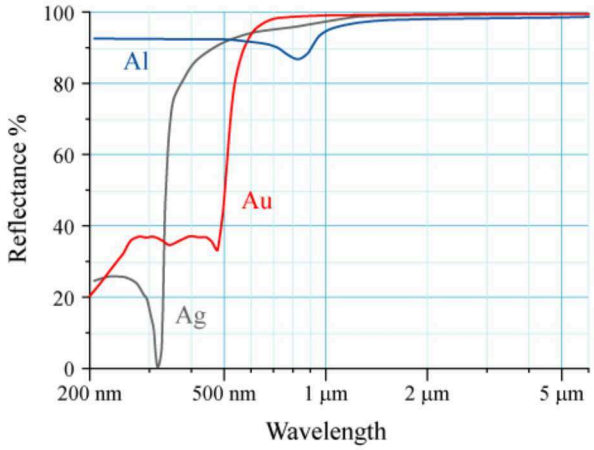

Figure 3.21 ***Reflectance of Al, Ag, and Au metal mirrors at normal incidence as a function of wavelength at room temperature.*** *The reflectance of gold is greater than 98% in the region from 700 nm to 10 µm (i.e. 0.124 eV – 1.77 eV). Reprinted from [Wiki].*

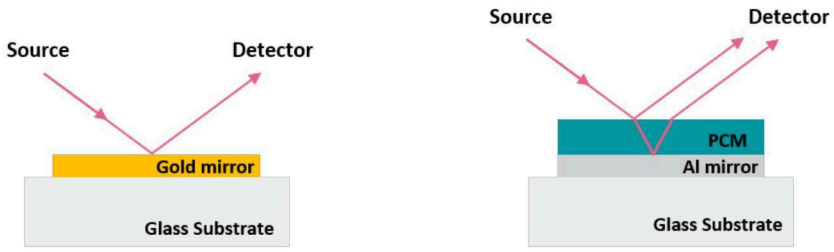

Figure 3.22 ***The cross-section view: (Left) Gold mirror as the reference.*** *The light with the wavelength above 1 µm is almost completely reflected by the gold mirror.* ***(Right) To-be-investigated PCM sample.*** *The transmitted light interact with the PCM and is reflected by the aluminum reflector and interfere with the reflected light on the surface of the PCM.*

The measurement on the gold reference provides the source intensity, which drifts a little with the time, therefore the reference reflectance is rerecorded every five measurements. Every reflectivity spectrum is normalized through dividing by the reference spectrum. In the following equations:

$$I_R(\omega) = I_0(\omega) R_R(\omega) \tag{3.16}$$

$$I_S(\omega) = I_0(\omega) R_S(\omega) \tag{3.17},$$

$I_R(\omega)$ and $I_S(\omega)$ are the reflection intensity of the reference and the sample, respectively. $I_0(\omega)$ is the intensity of the light source. $R_R(\omega)$ and $R_S(\omega)$ are the reflectance coefficient of the reference and the sample, respectively.

Divide equation (3.17) by equation (3.16), one gets

$$\frac{I_S(\omega)}{I_R(\omega)} = \frac{R_S(\omega)}{R_R(\omega)} \tag{3.18}.$$

The reflectivity of the reference spectrum $R_R(\omega)$ is taken as 1, the sample reflectance $R_S(\omega)$ can be derived. The reflectance spectra were analyzed with simulation tool SCOUT (W. Thess Hard- and Software). The dielectric function of samples from 0.05 to 1 eV was analyzed using the model as follows [Jell98, Fox01]:

$$\varepsilon_r(\omega) = \varepsilon_{const.} + \varepsilon(\omega)_{Tauc-Lorentz} \tag{3.19}.$$

The permittivity has the relation with the electric susceptibility χ,

$$\varepsilon_r = 1 + \chi = 1 + \chi_i + i\chi_j \tag{3.20},$$

where χ_i, χ_j are the real and imaginary part of the susceptibility. As there are nearly no free charges in amorphous PCMs, the Drude contribution is left out in equation (3.20). The first constant term of the equation represents the contribution of core electrons to the polarizability in the deep-UV. The Tauc-Lorentz model is widely used to simulate the interband transition of the PCMs [SKW+08]. It gives the following expression for the imaginary part of the susceptibility [Jell98]:

$$\chi_j(\omega) = \frac{1}{\omega} \frac{S^2 \omega_0 \omega_\tau (\omega - \omega_{Gap})^2}{(\omega^2 - \omega_0{}^2)^2 + \omega^2 \omega_\tau{}^2} \Theta(\omega - \omega_{Gap}) \quad (3.21),$$

where S is the oscillator strength, and ω_0, ω_τ and ω_{Gap} are resonance frequency, damping constant and Gap energy, respectively. The Tauc-Lorentz oscillator model with four parameters to adjust will do an excellent job in this work. The peak of the imaginary part of the susceptibility occurs at the resonance frequency and there is no absorption below the gap, i.e. the imaginary part is zero.

3.4.2 FT-FIR Transmission

FT-FIR transmission spectra ranges from 0.0025 eV to 1.49 eV (20 cm^{-1} – 12000 cm^{-1}, 0.6 THz – 360 THz) by a Bruker IFS 66/v Fourier transform infrared spectrometer. The upper limitation can even go up to 20000 cm^{-1}, which, however, is limited by the silicon substrate. The setup consists of a 4 K bolometer, far and mid infrared DLTGS detectors, as well as a liquid nitrogen cooled InSb photoconductor and a Si photodiode in combination with Hg-arc, globar and tungsten lamps. Three beam splitters, Ge on Mylar, Ge on KBr, and Quartz were utilized to achieve such a broad spectral range.

Films were prepared on the silicon substrate. The thickness of the silicon wafer is 380 μm, which is much larger than the film thickness. Both of the silicon substrate and films have optical quality parallel surfaces, which work as two parallel highly reflecting mirrors. With a spectral resolution of 5 cm^{-1}, the spectrum of the silicon wafer is fringe free, but the Fabry-Perot interferences of thin films are clearly discernible in the data. Although the FT-FIR neglects the interference features of the substrate, but preserves phonon spectral signatures of the film. In the analysis of the data, the substrate was treated as a material with incoherent light propagation. The incident angle is close enough to 0˚ within a couple of degrees. The angle of incidence has limited effect except for a slight shift in the frequencies of the interference fringes. Hence, the angle of incidence is assumed to be normal in all measurements.

The beam paths in the transmission mode of FT-FIR measurements on the bare silicon substrate and the sample are illustrated in figure 3.23. The spectra show the response of the sample has a

light propagation on the PCM layer sitting on top of a substrate. The incoming wave with normal incidence was reflected and transmitted at the interface and then absorbed by the layer of PCM and silicon wafer. The detector will receive the remaining light. The bandgap of monocrystalline silicon is 1.1 eV, which limits the higher frequency range of the transmission spectra. The spectra were subsequently analysed by approximating the dielectric function by a regular array of oscillatory terms. Each term abides by the variational Kramers-Kronig relation. Details of derivation can be found in literature [Kuz05, CLS14].

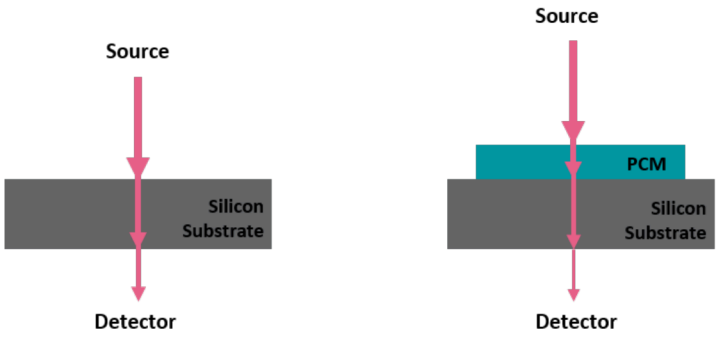

Figure 3.23 ***The cross-section view of (left) bare substrate; (right) to-be-investigated Sample.*** *The response of the bare substrate and a sample under the light of normal incidence is plotted. Without drawing the reflectance light.*

Sample Preparation

This chapter explains how to prepare samples for different experimental methods based on the measurement requirements. Sample types are referred to as DLIA samples, VNA samples, FT-IR samples and FT-FIR samples, according to their employment in the respective measurement techniques. It took most endeavor to produce VNA samples among those three types.

The first section introduces the film deposition techniques, and then the second section elaborates the common feature of DLIA samples and VNA samples. Furthermore, the process of producing DLIA samples and VNA samples are illustrated in detail in section 4.3 and 4.4, respectively. DLIA samples and VNA samples are compared in section 4.5. In the last section, both FT-IR samples and FT-FIR samples are presented.

4.1 Deposition Methods

4.1.1 Magnetron Sputter Deposition

Magnetron sputter deposition [Mart05] is a physical vapor deposition method. Conductive materials can be deposited using a DC power supply. The DC electric field is applied between the target (cathode) and the walls of a vacuum chamber (anode). An initial population of electrons in a low-pressure gas (typically an inert gas like argon) are accelerated by the field and collide with other gas atoms and ionize them. Thus, a plasma consisting of electrons and ions is formed, which is known as DC glow discharge. The DC field accelerates the gas ions towards the target. On striking the target, the gas ions knock out atoms and secondary electrons from the surface of the target. This is called DC sputtering.

In DC magnetron sputtering, a magnetic field originating from the permanent magnets below the target is present in addition to the electric field. Because of the Lorentz forces, the trajectories of electrons are some extent confined to the region close to the target surface along the direction of $\boldsymbol{E}\times\boldsymbol{B}$, which improves the ionization efficiency of gas atoms and produces more

secondary electrons. Hence the plasma can be sustained at a lower gas pressure, which reduces energy losses of escaped target atoms through gas collisions. The ejected target atoms are deposited on the substrate located opposite to the target (sputter deposition). At the target, gas ions rebound back towards to the substrate. They hit the surface of the growing film only after deceleration by gas atoms collisions and the electric field, which decreases the impact of ion bombardment on the microstructure and morphology of the growing films. The energy of secondary electrons will be drained after collisions with background gas atoms, and then they will depart from the target surface and flow to the substrate and the chamber wall. The schematic diagram of the sputtering process is shown in figure 4.1.

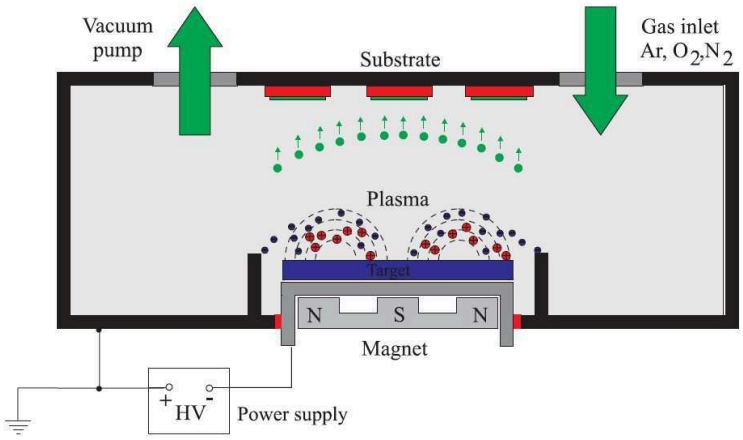

Figure 4.1 ***A schematic diagram of a magnetron sputtering chamber.*** *The substrates (red) on the sample holder are located right above the target (blue). Positive argon ions (red) and negative electrons (black) constrained around the target, from which target atoms (green points with arrows) are knocked out and deposited onto the substrate. Reprinted from [Kalb06].*

Since the same chamber is used for thin film deposition of a variety of material compositions, the sample holders and racks used in the chamber were cleaned before sample preparation by sand blasting each time in order to avoid contamination. PCMs were deposited from stoichiometric targets of 99.99% purity, which were prefabricated, polycrystalline and compressed powder. The DC magnetron sputtering in the system LS 320S (PFEIFFER / VON ARDENNE) was not started before reaching base pressure of $\leq 2\times10^{-6}$ mbar. The argon flow was set to 20 sccm argon flow and the DC power generator to a constant power of 20 W. The

argon pressure during the sputtering process was typically 3.4×10^{-3} mbar and the distance between the target and substrate was 4 cm.

The thickness of the films was determined according to the deposition rate for each target in the sputtering system and afterwards verified with a profilometer. The structure of materials under investigation were determined using X-ray diffraction (PANalytica, Copper Kα, λ=1.5418 Å) under grazing incidence geometry. With the sputter chamber used in this work, as-deposited GeTe, $Ge_8Sb_2Te_{11}$, $Ge_3Sb_2Te_6$, $Ge_2Sb_2Te_5$, $Ge_1Sb_2Te_4$ are amorphous, while as-deposited $Ge_1Sb_4Te_7$ and Sb_2Te_3 are partially crystalline. However, amorphous $Ge_1Sb_4Te_7$ films could be successfully obtained by cooling the substrate with liquid nitrogen during the deposition, and amorphous Sb_2Te_3 films were prepared with defects of cracks.

4.1.2 Vacuum Thermal Evaporation

A thermal evaporator is used to fabricate the metallic electrodes of all samples. There are two tungsten crucibles at the bottom of the evaporator, right above which the sample substrates are fixed to the sample holder with a cooling system. Electrode materials are put in the two tungsten crucibles separately and heated by two individual electric circuits. The thickness of the films was calculated in real time during the evaporation with the assistance of a quartz crystal microbalance, which is placed close to samples at the same height. The evaporation started at the base pressure of $\leq 2\times10^{-6}$ mbar. 5 nm of chromium as the adhesion layer and 100 nm of gold are deposited sequentially onto the substrate with a rate of 1 Å/s and 3 Å/s, respectively.

4.2 Common Specification for the DLIA and VNA Samples

Figure 4.2 illustrates the two contact geometries which can, in principle, be used for electrical measurements on thin films. It can be readily seen that the two geometries differ significantly with respect to the distribution of electrical field lines: In the in-plane geometry as shown in figure 4.2 (left), only an insignificant portion of the field lines run through the PCM. The dielectric response being dominated by a mixture of the dielectric constants of substrate and air is essentially insensitive to the dielectric constant of the phase-change layer. However, as the

current is confined to the phase-change film in both cases, both geometries, in-plane and sandwich, can be employed to study the real part of the AC conductivity $\sigma_1(\omega)$. Consequently, experiments utilizing the in-plane geometry - such as [PGL+13, SPH+10] - are suitable for deriving $\sigma_1(\omega)$, but they *must not* be employed for obtaining the real part of the dielectric function $\varepsilon_1(\omega)$. Therefore, the sandwich geometry in figure 4.2 (right), where a thin layer of amorphous PCM is inserted between two metal electrodes, is employed for electrical measurements by DLIA and VNA in this thesis.

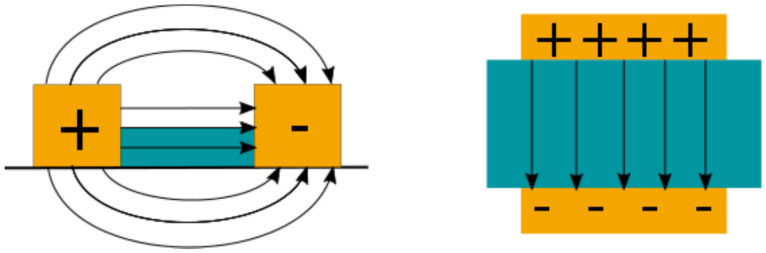

Figure 4.2 ***Electric field distribution in in-plane structures (left) and in sandwich structures (right),*** *not to scale.*

In order to not influence the current-voltage characteristics of the device significantly, the interfacial junction between the electrode and the PCM in figure 4.2 (right) is required to have a low resistance even in the limit of small electric fields. In other words, contacts which are not only thermally stable, but also have a linear current-voltage curve (Ohmic contacts) are required. Platinum and gold are often used as electrodes for devices of p-type semiconductors. Previous works have ruled out the influence of Schottky-emission when contacting amorphous PCMs using gold [Jost12], chromium [LKK+11] or tungsten [WM64] electrodes, because no variations of the activation energy for conduction of amorphous PCMs were observed. Therefore, with a clean and smooth interface between the PCM and the metal, the applied voltage is expected to drop nearly completely across the PCM layer.

However, contamination such as residues of photoresist on the bottom electrode, stemming from the lithographic process (see further below), will result in a high interface resistance. Besides that, such residues may also causes the formation of pinholes in the PCM layer, which will lead to a short circuit between the top and bottom electrode. In summary, the surface of the bottom electrode and the PCM layer must be clean.

4.3 DLIA Samples

The sample structure shown in figure 4.4 (a) was firstly used in this work, but practically there are always misalignments between the top and the bottom electrodes as shown in figure 4.4 (b). The effective areas of the capacitors had to be determined for each device. Consequently, the shadow masks were changed to produce a cross-bar structure in figure 4.4 (c). The complete sample has the stacked structure as 100 nm Au / 5 nm Cr / PCM / 100 nm Au / 5 nm Cr / glass.

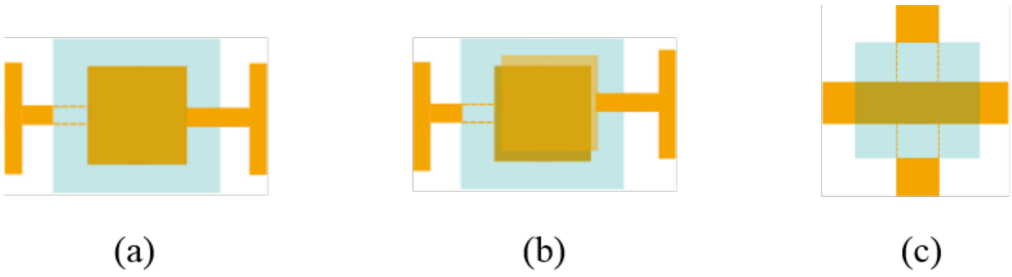

Figure 4.4 ***Schematic diagrams of DLIA samples:*** *(a) an ideal DLIA sample without area-misalignment; (b) a DLIA sample with unavoidable area misalignment; (c) a DLIA sample in cross-bar structure. Electrodes are shown in orange and the layer of PCMs in turquoise.*

DLIA samples were kept and transferred in the ambient environment after the deposition of each layer. Samples with smaller overlapping area are preferred because of lower probability of defects induced by dust grains. But the uncertainty of the areas due to the low precision of the shadow masks becomes problematic as the areas decrease. The minimum resistance can be measured by the DLIA in the PPMS is 25 kΩ. Supposing that the thickness of the PCM layer is 100 nm and its conductivity has the order of magnitude 10^{-9} S/cm at low temperatures, the area should be smaller than 40 mm^2. Following these considerations, the thickness of the PCM layer was varied from 100 nm to 1000 nm, and capacitor areas of 1 mm^2 and 2 mm^2 were used. The thickness of samples was determined within an uncertainty of 5 %.

To fabricate the samples, glass substrates were carefully cleaned successively with acetone and propanol in an ultrasonic bath for 10 minutes and subsequently blow-dried with nitrogen gas.

Each layer of the DLIA samples were patterned with metal shadow masks, which are templates with pattern features.

4.4 VNA Samples

The fabrication of VNA samples is labor-intensive operation requiring some measure of skill and experience. Those samples were prepared on (11-20)-oriented sapphire substrates with the size of 20×20×0.53 mm^3. The polished side of the sapphire was used because of its better surface flatness. Substrates were cleaned successively with acetone and propanol in an ultrasonic bath for 10 minutes and subsequently blow-dried with nitrogen gas.

*Table 4.1 Capacitor areas [μm^2] of devices labeled with the position (row number*column number) on the lithography mask designed by Kathrin Krüger [Krüg10].*

2-port	9*1	9*2	9*3	9*4	9*5	9*6	9*7	9*8	9*9	9*10
	3*11	3*12	3*13	3*14	3*15	3*16	3*17	3*18	3*19	3*20
1-port	10*1	10*2	10*3	10*4	10*5	10*6	10*7	10*8	10*9	10*10
	4*11	4*12	4*13	4*14	4*15	4*16	4*17	4*18	4*19	4*20
Area	10^2	15^2	30^2	50^2	70^2	100^2	140^2	190^2	230^2	400^2

There are 20 two-port-devices and 20 one-port-devices on one VNA sample designed for the two-port and the one-port impedance measurements, respectively. The layer structure of the two-port-device and one-port-device is the same, but the top electrode of the one-port device is short connected to the ground. Ideally the impedance of some devices are close to the characteristic impedance of the measurement system, i.e. 50 Ω. Given the electrical properties of amorphous PCMs at room temperature, this condition can only be met by adjusting the thickness and area of the device. In order to achieve the impedance matching, the photolithography technique was applied to pattern smaller devices with larger number. The photolithography process described below makes sample preparation more efficiently, however, as it involves a lift-off step, it limits the film thickness up to 200 nm. Therefore, combining the

limited thickness and the known resistivity of amorphous PCMs, the optional areas of sandwich capacitors are varied from 10^2 m to 400^2 m given in table 4.1. It is noteworthy that the misalignments between the positions of the top and bottom electrodes in smaller samples become more problematic. Figure 4.5 depicts the cross sectional structure of a device on a VNA sample. Bottom electrodes (100 nm Pt / 5 nm Cr) and top electrodes (100 nm Au / 5 nm Cr) were grown by thermal evaporation, and the layer of PCM was sputter-deposited. Platinum substitutes gold as bottom electrode because gold would diffuse upon heating during the lithography process (bake at 95 ˚C for 1.5 minutes and 115 ˚C for 4.5 minutes). Macroscopic defects like pin holes caused by dusts can be avoided in VNA samples because the lithography steps are processed in the cleanroom and the capacitor areas are small. Furthermore, the sharpness of the edges of the structures made by photolithography is superior to the shadow mask technique.

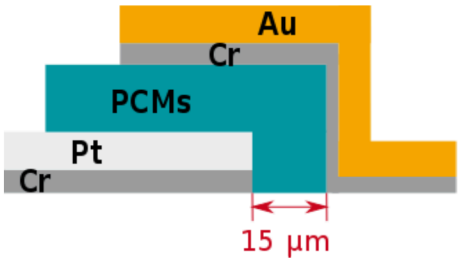

Figure 4.5 ***Cross sectional structure of a device on a VNA sample*** *(not to scale). The thickness of the PCMs layer is between 100 nm and 150 nm. The parasitic capacitance at the side of the sample can be ignored because the side distance labeled in the sketch (15 µm) is much larger than the film thickness.*

4.4.1 Photolithography Process

The photolithography process transfers a geometric pattern from a photomask to a light-sensitive chemical "photoresist" on the substrate using UV light. The process was done in the cleanroom. The universal photoresist AR-U 4040 (ALLRESIST) was employed in this work. This normally positive photoresist (UV-exposed parts of the resist are soluble in a developer) can be reversed into the negative one with two additional steps, reversal bake (i.e. baking at 110 ˚C for 4.5 min) and the flood exposure (i.e. exposure to the UV light without the photomask), namely image reversal process. In this case, the unexposed part of the resist is soluble in the

developer, while the exposed area stays after developing. Hence, the desired material remains on the substrate where the resist was unexposed. After preparing the desired material onto the substrate with structured resist, the substrate was put into the acetone for lift-off because the photoresist is dissolved in acetone.

The experimental parameters of both lithography processes are listed in table 4.2. The positive lithography process is simpler than the image reversal process, but it tends to cause high walls at the edge of the film as explained in [Schl12]. The height of those walls can reach up to several hundred nanometers, thus the positive photolithography process is unsuitable for the bottom electrode and the PCM layer as it frequently leads to electrical shorts with the top electrode.

Table 4.2 Comparison between the positive and negative lithography processes of the AR-U 4040 photoresist.

Process steps	**Positive process**	**Negative process**
Spin coater	4000 rpm (program 9)	4000 rpm (program 9)
Soft bake	1.5 min at 95 ˚C	1.5 min at 95 ˚C
UV – exposure	20 s	20 s
Reversal bake	NO	4.5 min at 110 ˚C
Flood exposure	NO	1 min
Development	35 s	35 s
Development solution AR 300-47 : DI-water	1:2	2:3

The above mentioned structuring method is known as the lift-off method, which removes the whole film above the resist and nothing more. The photolithography needs to be done before preparing the material onto the substrate. There are also other structuring methods, such as dry etching (eg. ion etching) and chemical wet etching, both of which need to prepare the desired material before the photolithography process. Only the material uncovered by the resist is etched away. It is difficult to control the etching rate of dry etching and chemical wet etching, hence the lift-off method is simpler and more efficient. But the lift-off method also has disadvantages. Firstly the film thickness is limited. Secondly, the film does not rip off laterally,

and consequently too many parts were left on the sample or others peel off together with the rest.

4.4.2 First Layer (Bottom electrode)

At the beginning of this work, the layer stack (from top to bottom: Au / Cr / PCMs / Au / Cr / sapphire substrate) from reference [Schl12] was used. For the fabrication of the bottom electrode of Au and Cr, a lift-off process with the negative photoresist was employed to avoid the formation of walls (see above). To overcome this problem, two approaches were investigated: The integration of an additional anti-diffusion layer made of titanium nitride created in an optimized sputter-deposition process (Approach 1) and the replacement of gold by platinum and further optimizations (Approach 2), which are described in the following.

Approach 1: A layer of 15 nm TiN/Ti film was introduced as an anti-diffusion layer between the bottom electrode and PCMs, because gold diffuses seriously at the elevated temperatures required during the lithography process. TiN / Ti films were sputter deposited onto the gold layer after transferring from the thermal evaporator to the sputtering chamber. The magnetron sputtering method is more likely to form high walls than the evaporation method, because sputtered particles can reach the substrate from wide directions, while only vertically moving evaporated particles have enough energy to arrive at the substrate. The surface roughness and edges of the bottom electrodes were measured by the Atomic Force Microscope (AFM, Digital Instruments Dimension 3100).

Representative AFM graphs of the bottom electrode are shown in figure 4.6 (a), in which high walls were obvious. For this reason, a home-made metal collimator (a hollow cuboid made of metal) is introduced between the target and substrate during sputtering. The collimator can block all particles moving not perpendicular to the substrate, which sacrifices a lot of sputtering rate, but indeed removes high walls at the film edges, as shown in figure 4.6 (b). Although high walls at edges were effectively avoided with the collimator, impedance measurements of samples with such bottom electrodes were defective. The obtained dielectric permittivity and AC conductivity of investigated samples were dependent on the sample geometry size (i.e. the

thickness and the capacitor area), which may be attributed to the oxidation of the TiN / Ti film. Therefore, this approach was discarded.

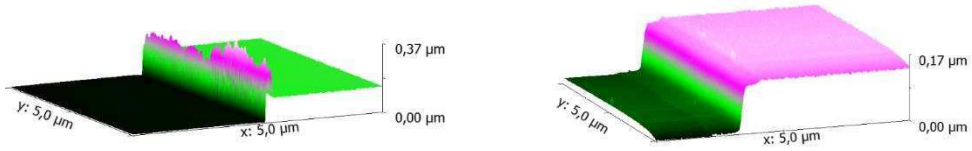

Figure 4.6 ***AFM graphs of the bottom electrode*** *(TiN / Ti / Au / Cr / Sapphire): without collimator (left), with collimator (right).*

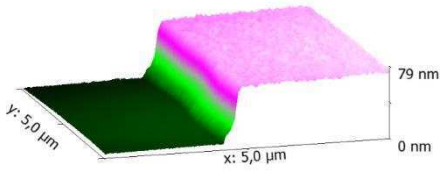

Figure 4.7 ***AFM graph of the bottom electrode*** *(Pt / Cr / Sapphire) after argon ion etching.*

Approach 2: During the course of this work, evaporated platinum thin films became available in the cleanroom of the Jülich Research Center with the help of Marvin Kaminski. Platinum films are a good choice for electrodes because platinum does not oxidize in the air at room temperature and it is less prone to diffision at elevated temperatures. Hence the gold film was substituted by the platinum film for the bottom electrode. However, AFM measurements show that the surface of platinum bottom electrodes, is rougher than that of gold electrodes and even has spikes. Argon ion etching of 5 to 10 minutes was introduced after the preparation of the lift-off mask for the PCM layer (see below) to get rid of the spikes and to make sure there are no resist residues. The edges of platinum bottom electrodes after ion etching were scanned by AFM, as shown in figure 4.7. Neither high walls at the edge nor spikes on the surface were observed. Therefore, this approach was considered successful.

4.4.3 Second Layer (PCM)

In previous works [Schl12, Krüg10], a positive lift-off process was used to pattern the PCM layer, which influenced the quality of the top electrode due to high walls. For this reason a negative lift-off process was used in this work to pattern the PCM layer. Another issue to consider is that the PCMs tend to oxidize when they are taken out of the sputtering chamber. Therefore, a step was introduced in which, samples were etched in a hydrogen fluoride (HF) solution of 1 wt% for 30 seconds after preparing the mask for the top electrode. Afterwards, samples were transferred to the evaporator chamber immediately for evaporation of the top electrode.

4.4.4 Third Layer (Top Electrode)

This layer was patterned by a positive lift-off method. Although platinum works well for the bottom electrode, it is not a good choice for the top electrode. The Young's Modulus of the platinum thin film is 139.7 GPa, which is nearly twice the modulus of the gold thin film (i.e. 69.1 GPa) [VSC04]. In other words, the platinum is more brittle than the gold. In repeatedly attempts with various process parameters, the top electrodes always peeled off in large pieces after the process of lift-off. Figure 4.8 depicts the bad quality of the top electrodes made of platinum with the Optical Microscope (Leica DM2500 M).

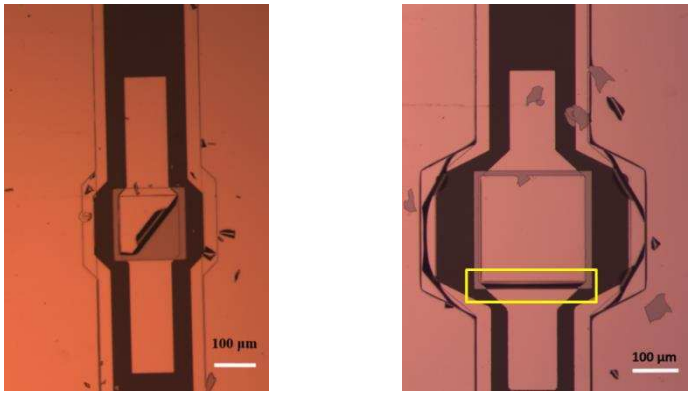

Figure 4.8 ***Optical microscopic images of two broken devices with Pt / Cr as both the top and the bottom electrode.*** *Left picture: the top electrode layer peeled off from the top of the PCM layer. Right picture: the layer of PCM in the yellow frame was pulled off together with the Pt / Cr layer after lift-off. The PCM layer at this position is deposited directly onto the substrate and the adhesive force of PCMs to the sapphire substrate is not strong enough.*

However, gold is completely appropriate for the top electrode because heating is no longer needed after the evaporation of top electrodes. Gold diffusion does not have to be considered at room temperature. Figure 4.9 shows an image of an intact device with a platinum bottom electrode and a gold top electrode.

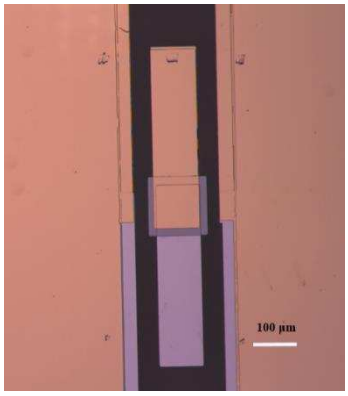

Figure 4.9 ***Optical microscopic image of an intact device with Pt/Cr as the bottom electrode and Au/Cr as the top electrode.*** *Both the top and bottom electrodes are intact. A small misalignment about 5 µm between the top and bottom electrodes can be observed and is quite typical, because the resolution of the mask aligner is 2 µm.*

4.4.5 VNA Sample Preparation: Summary

After the aforementioned improvements, high-quality samples could be prepared. The process of sample preparation is summarized and illustrated in figure 4.10. Based on the work of Franziska Felicitas Schlich [Schl12] and Kathrin Krüger [Krüg10], further optimization of the sample preparation was achieved in this work. High-quality samples were obtained after implementation of four extra steps:

(a) To cope with the problem of gold diffusion into the PCM layer, gold was substituted by platinum as the bottom electrode material.

(b) The image reversal was adopted not only to the layer of bottom electrode, but also for the layer of PCM to prevent high walls at the edges of the PCM layer. This step guarantees good quality of top electrodes.

(c) Argon ion etching was introduced to clean the surface of the bottom electrode after the preparation of the second optical mask;

(d) HF dip was introduced to clean the oxide of PCMs and contaminations left by the process of lithography process.

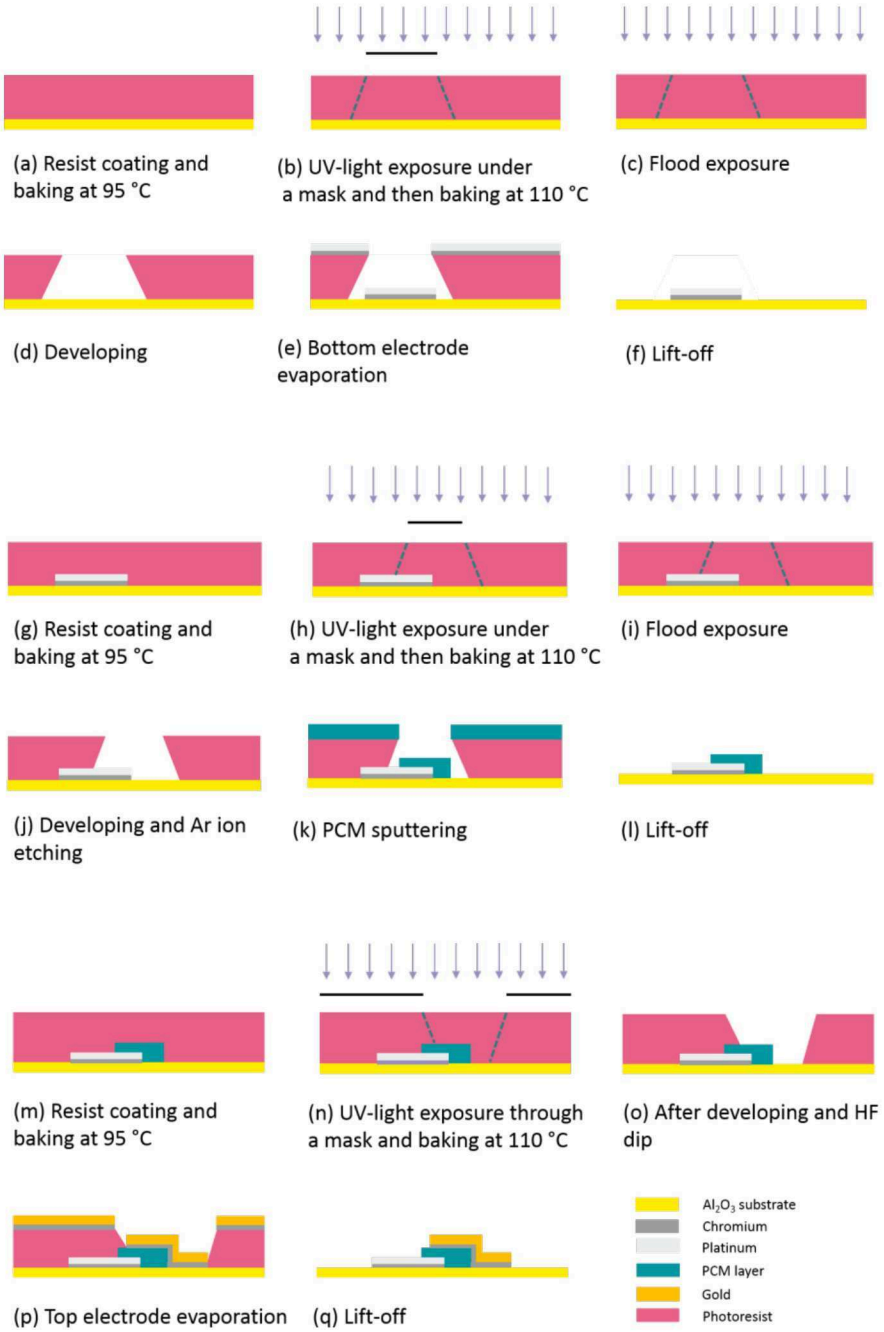

Figure 4.10 ***The fabrication process of VNA samples.*** *For the bottom electrode layer and the PCM layer, the image reversal process was applied, while the top electrode layer used the positive photolithography process. (a) A sapphire substrate was coated with resist (about 1.5 μm) by a spin coater and then baked on a hot plate at 95 ℃ for 1.5 minutes; (b) The coated substrate was exposed to the UV light through the mask for the bottom electrode for 20 seconds and then post-baked on a hot plate at 110℃ for 4 minutes;*

(c) It was flood exposed by the UV light for 1 minute; (d) It was developed in the developing solution AR300-47:H_2O (2:3) for 35 seconds; (e) 5 nm chromium and 100 nm platinum were evaporated onto the substrate; (f) The resist and films on the resist were washed away after lift-off with acetone and propanol; (g)Same as (a);(h) The coated substrate was exposed to the UV light through the mask for the PCMs layer for 20 seconds and then post-baked on a hot plate at 110ºC for 4 minutes; (i) Same as (c);(j) The sample was developed in the developing solution AR300-47:H_2O (2:3) for 35 seconds, and it was etched by argon ions for 5 minutes after developing; (k) A layer of PCMs was sputtered onto the argon cleaned surface; (l) The sample was lift-off with acetone and propanol;(m) Same as (a);(n) The coated substrate was exposed to the UV light through the mask for the top electrode for 20 seconds and then post-baked on a hot plate at 110ºC for 4 minutes; (o) The sample was developed with developing solution and then etched in 1 wt% HF solution; (p) 5 nm chromium and 100 nm gold were evaporated onto the substrate; (q) The resist was lifted off in acetone in ultrasonic bath. Finally the sample was cleaned in propanol and blow-dried with nitrogen gas.

4.5 Comparison between the DLIA Sample and the VNA Sample

The comparison between the DLIA sample and the VNA sample are listed in table 4.3. They are designed for measurements in different frequency regions. The preparation of the VNA samples involves lithography processes, which are more time-consuming than that of the DLIA sample, but results in better defined device geometry.

Table 4.3 Comparison between the DLIA sample and the VNA sample.

	DLIA sample	**VNA sample**
Substrate	glass	sapphire
Bottom electrode		
Material	Au/Cr	Pt/Cr
Size	1×1 mm^2, 2×2 mm^2	10×10 μm^2…400×400 μm^2
Thickness	100 nm	100 nm
Patterning	Metal shadow mask	Negative photolithography
PCMs layer		
Material	PCMs	PCMs
Thickness	100 nm – 1000 nm	90 nm – 200 nm
Patterning	Metal shadow mask	Negative photolithography
Top electrode		
Material	Au/Cr	Au/Cr
Size	1×1 mm^2, 2×2 mm^2	10×10 μm^2…400×400 μm^2
Thickness	100 nm	100 nm
Patterning	Metal shadow mask	Positive photolithography
Application range	0.5 Hz – 186.2 Hz	9 kHz – 3 GHz

4.6 FT-IR and FT-FIR Samples

Proper consideration must be given to potential sample restrictions such as appropriate substrates and the sample thickness for respective modes. For infrared reflection measurements the substrate needs to be infrared-reflective, such as aluminum film, whereas for transmission measurements an infrared-transparent material is required, such as silicon with high resistivity. The abovementioned sputter tool in section 3.1 was employed to fabricate also samples for the optical measurements. The layer of PCMs and non-PCM chalcogenides were deposited from stoichiometric targets using DC magnetron sputtering. The optical dielectric functions of chalcogenides $Ge_{15}Te_{85}$, GeSe, $Ge_2Sb_2Te_5$ were investigated by both FT-IR reflectance and FT-FIR transmission for comparison. Other amorphous PCMs were studied only with FT-FIR transmission spectra.

4.6.1 Samples for FT-IR Reflectance

Glass substrates were cleaned sequentially with acetone and propanol in an ultrasonic bath and then blow-dried with nitrogen gas. A layer of aluminum thin film works as a reflector for optimal reflectance. The aluminum thin film of 100 nm and the amorphous chalcogenide of 300 nm were sputter-deposited sequentially onto glass substrates, forming a layer stack of "chalcogenide / Al / glass". The optical thickness, which is defined as the product of the film thickness (d) and the refractive index (n), should be comparable to the light wavelength. For a fixed film thickness the reflectance oscillates periodically as the optical frequency changes. There should be at least one complete oscillation present in the considered frequency range. The refractive index of the amorphous chalcogenide is about 4 and the sample thickness is fixed at around 300 nm. The wavenumber difference between fringes of the reflectance spectra can be estimated by

$$\Delta\nu = \frac{1}{2nd} \qquad (4.1),$$

which equals 4167 cm^{-1}. As the measurement range of the FT-IR varies from 400 cm^{-1} to 8000 cm^{-1} (0.05 eV to 1 eV), 300 nm is thick enough to obtain interference fringes in the reflection spectra of the sample.

4.6.2 Samples for FT-FIR Transmission

For transmission measurements the amorphous PCMs were deposited onto the highly resistive (> 5000 kΩ·cm) silicon (100) wafers, forming a layer stack of "PCM / Si". The high-resistivity silicon was chosen to avoid infrared absorption by free carriers. Both sides of the silicon substrates are polished.

The FT-FIR transmission was recorded from 20 cm^{-1} to 12000 cm^{-1} (0.0025 to 1.5 eV). The highest signal-to-noise ratio is achieved when the sample has the proper thickness. The thicker the sample, the more information about the sample can be gotten from the measurement, but too thick samples lead to total absorbance. In a similar way as described in the last section the sample thickness is fixed around 800 nm, which is thick enough to distinguish the transmission spectra of the PCMs from that of the bare substrate.

AC Electrical Measurement

In this chapter, an integrated lock-in amplifier in the PPMS realizes capacitance measurements between 0.5 Hz and 186.2 Hz from 4 K to 170 K. The first section presents the interior structure in the cooling chamber of the PPMS. Afterwards, the reliability and accuracy of this method are assessed in a pre-study, where surface-mount devices (SMD) of known resistance and capacitance were measured. In the third section, the temperature dependent behavior of the dielectric functions of amorphous PCMs as well as non-PCMs are presented. Moreover, the aging effect on the dielectric properties of GeTe is discussed.

5.1 PPMS Chamber

In order to observe the capacitive behavior of amorphous chalcogenides at frequencies below 186.2 Hz, the conductivity should have the order of magnitude for a maximum of 10^{-9} S/cm according to equation (3.1) with the assumption of $\varepsilon_{st} = 30$. The conductivities of amorphous PCMs are around 10^{-3} S/cm at room temperature, hence 5 to 6 orders of magnitude above this limit. However, a substantial decline of the conductivities of amorphous PCMs can be realized in a cryostat, since they are strongly temperature dependent. Therefore, a Physical Properties Measurement System (PPMS) by Quantum Design was used, which includes both the required cryostat and the equipment for performing electrical measurements ("ETO" for electro-transport option). The operating temperature of the PPMS is controlled by several heaters and thermometers can vary from 1.9 K to 400 K. In this work, the measurement was only conducted between 4 K and 170 K. The highest measurable temperature of the capacitive behavior varies with the conductivity of the material studied.

The samples reside in a chamber, shown in figure 5.1, which in this work was evacuated with an integrated Cryo-pump to a vacuum of $< 10^{-4}$ Torr. Details of the sample preparation for the AC electrical measurement at low frequencies was described in section 4.3.

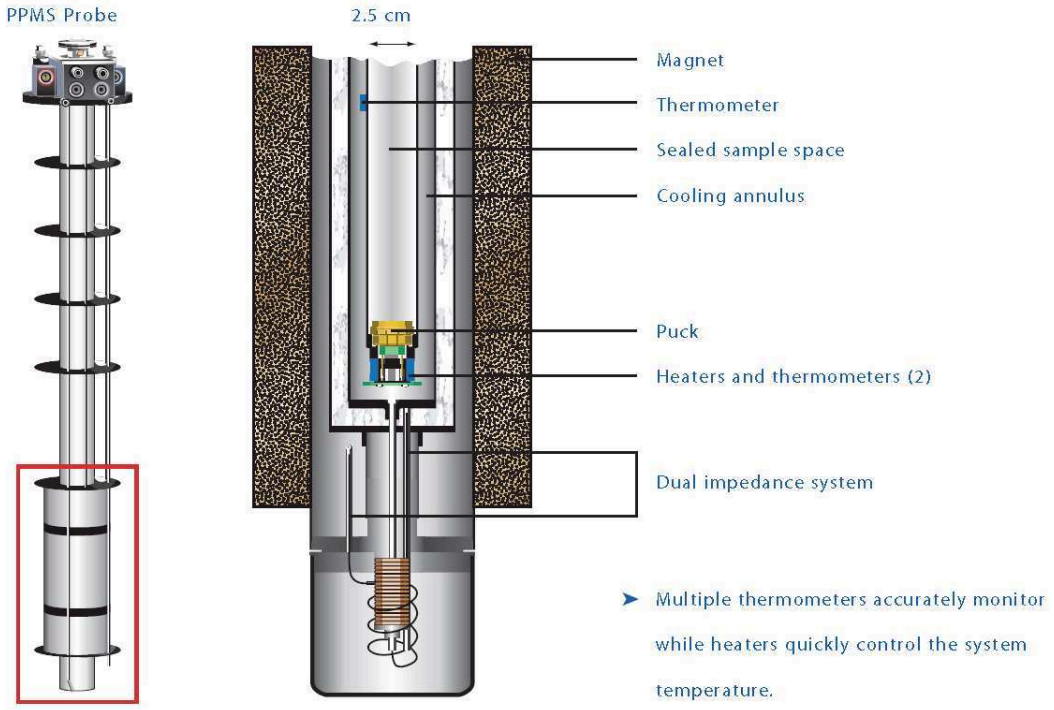

Figure 5.1 ***Cross-section diagram of the PPMS chamber****. A sample was fixed on the top surface of the puck by double-side adhesive tape and it was bonded with the puck by gold or aluminum wire. The puck was put into the PPMS chamber through a pipe of 2.5 cm width. The puck is connected to the outside ETO head through the twisted pair cables at the bottom of the chamber. Reprinted from [Norr12].*

5.2 Validation Experiments

The two-wire mode of the ETO system is designed for measuring high impedance instead of low capacitance, so it is necessary to prove its validity for measuring capacitance at the beginning. Four surface-mount devices with known resistance and capacitance were employed. Two resistors and two capacitors were soldered in parallel connection, i.e., 100 MΩ // 1 nF and 100 MΩ // 100 nF. The tolerance of the resistance and capacitance of the SMD parts is within 1%. Capacitors of 1 nF and 100 nF were chosen because the capacitance of PCMs samples were estimated to be in the range. The resistance of PCMs samples is larger than 100 MΩ at 4 K.

The voltage of 0.01V was applied to the AC electrical measurements of both SMD and PCMs samples. The ETO system measures the AC resistance at 9 discrete frequencies: 0.5 Hz, 1.0 Hz,

6.1 Hz, 12.2 Hz, 15.3 Hz, 21.4 Hz, 58.0 Hz, 143.4 Hz and 186.2 Hz in sequence. Results are the average of 10-time measurements at each frequency. The current amplitude, the in-phase and quadrature current, the reciprocal of conductance, phases and other parameters are given in the data file. Results were analyzed with the equivalent circuit (RC model) shown in figure 3.1. R_1 and C_1 refer to the sample resistance and capacitance, respectively. The contact resistance is only several Ohms, which is neglected because it is far less than the sample resistance. The wire self-inductance is also insignificant.

The impedance of the equivalent circuit in figure 3.1 is:

$$Z_{DUT} = \frac{R_1}{1 + i2\pi f R_1 C_1} \tag{5.1}.$$

This leads to

$$\mathrm{Abs}(I) = \sqrt{\left(\frac{U}{R_1}\right)^2 + (2\pi f U C_1)^2} \tag{5.2}$$

$$\mathrm{Im}(I) = i \cdot 2\pi f U C_1 \tag{5.3}$$

$$\theta = \arctan(2\pi f R_1 C_1) \tag{5.4},$$

where Im(I) is the quadrature current, Abs(I) is the amplitude of AC current, f is the frequency, U is the applied voltage and θ is the phase angle. On the one hand, R_1 and C_1 can be obtained by a nonlinear fitting of the amplitude of current using equation (5.2). On the other hand, the quadrature current is linear to the frequency, so the sample capacitance can be calculated from the slope using equation (5.3). The results from those two analytical methods are compared in the next section, which can also be seen in the bachelor thesis of Norrman [Norr12].

5.2.1 100 MΩ // 1 nF

In the case of 100 MΩ // 1 nF, the characteristic frequency is $f_{RC} = (2\pi R_1 C_1)^{-1} = 1.59$ Hz, which is lower than the upper limit of the frequency range (186.2 Hz), but higher than the lower limit of the frequency range (0.5 Hz). Still, the circuit is mostly dominated by the capacitive element and is in favor of the capacitance measurement. The magnitude of the AC current is obtained from the measurement. It is fitted with the RC model using equation (5.2). As can be seen in figure 5.2, the Abs(I) is fitted very well with the RC model. Through the nonlinear fitting with Abs(I), there are $R_1 = 99.87$ MΩ, $C_1 = 1.04$ nF. The deviation of the resistance from the correct value is 0.13% and that of the capacitance is 4%. There is a phase error at high frequencies when the impedance declines to about 1 MΩ at 143.4 Hz, which needs to be attributed to the measurement electronics: the high impedance mode is designed for measuring impedance higher than 2 MΩ.

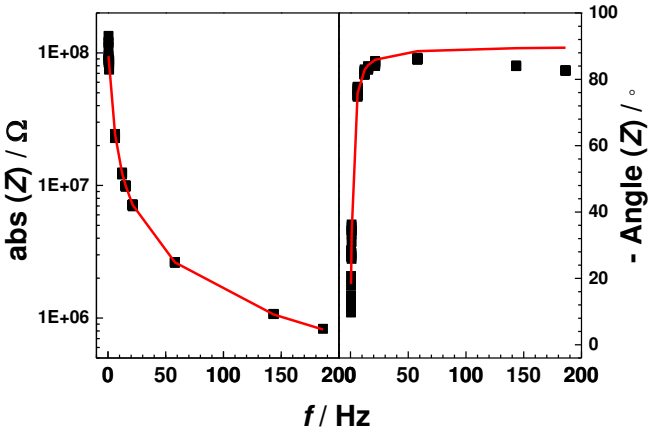

Figure 5.2 ***AC electrical measurements on the parallel circuit of a capacitor (1 nF) and a resistor (100 MΩ).*** *(Left) the amplitude of the impedance, abs (Z), as a function of the frequency; (Right) the opposite number of the phase angle of the impedance, -Angle (Z), as a function of the frequency. The experimental and fitting data (according to equation 5.2 and 5.4 with R_1 = 99.87 MΩ, C_1 = 1.04 nF) are shown in black dots and red lines, respectively.*

The complex current is dominated by the quadrature current, so the in-phase current deviates seriously even if a small phase error arise at higher frequencies. Hence, in this case the measured

quadrature is much more reliable than the in-phase current. Through linear fitting of the quadrature current, shown in figure 5.3, the capacitance is calculated to be 1.02 nF, the deviation of which from the correct value is 2 %.

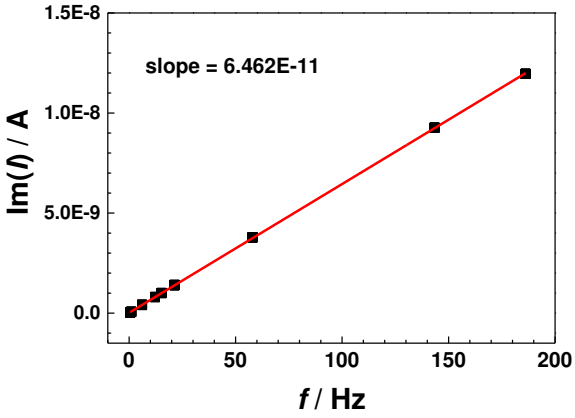

Figure 5.3 ***AC electrical measurements on the parallel circuit of a capacitor (1 nF) and a resistor (100 MΩ) at room temperature.*** *The imaginary part of current, Im(I), is plotted as a function of the frequency. The experimental and fitting data (according to equation 5.3 with C_1 = 1.02 nF) are shown in black dots and the red line, respectively. The slope of the fitted line is given in this figure.*

5.2.2 100MΩ // 100 nF

In the case of 100 MΩ // 100 nF, the characteristic frequency is f_{RC} = 0.02 Hz, which is far less than 186.2 Hz and even significantly less than 0.5 Hz. The device is completely dominated by the capacitive behavior in the frequency range, which facilitates the capacitance measurement. However, the current exceeds the limit of 250 nA as frequency increases above 21.4 Hz, so only the data below 58.0 Hz was analyzed. R_1 = 83.5 MΩ, C_1 = 97.3 nF were obtained by the nonlinear fitting, shown in figure 5.4. The fitted phase deviates from the measured phase because the impedance is smaller than 2MΩ. The deviation of the resistance from the correct value is as high as 16.5%. Such a high deviation is not unexpected because the device is nearly shorted by the capacitor, which is adverse to the resistance measurement. The deviation of the capacitance, which is what will give us the dielectric constant in the measurement of 'real' samples, is 2.7%.

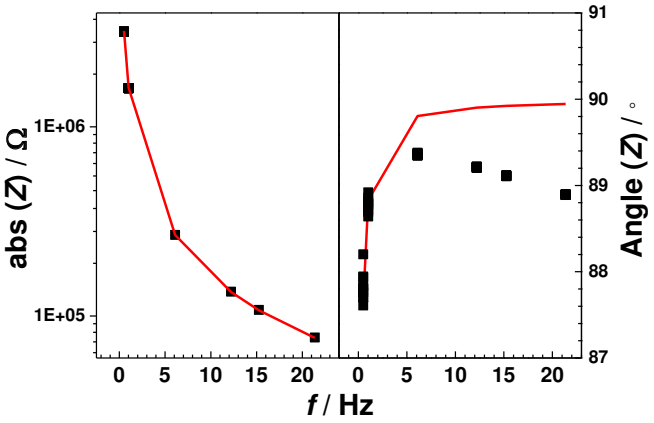

Figure 5.4 ***AC electrical measurements on the paralleled circuit of a capacitor (100 nF) and a resistor (100 MΩ).*** *The labels of the X- and Y-axis have the same meaning as in figure 5.2. The experimental and fitting data (according to equation 5.2 and 5.4 with R_1 = 83.5 MΩ, C_1 = 97.3 nF) are shown in black dots and red lines, respectively.*

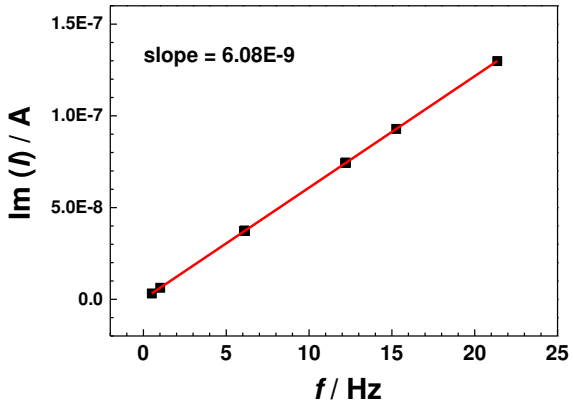

Figure 5.5 ***AC electrical measurements on the parallel circuit of a capacitor (100 nF) and a resistor (100 MΩ).*** *The imaginary part of current, Im(I), is plotted as a function of the frequency. The experimental and fitting data (according to equation 5.3 with C_1 = 96.8 nF) are shown in black dots and red lines, respectively. Reliable results could be obtained only up to 21.4 Hz because the sample impedance was too small and the current exceeds the range of the ampere meter at higher frequencies. The slope of the fitted line is given in this figure.*

The current in the measurement beyond 21.4 Hz is saturated. The linear fitting of the quadrature current below 21.4 Hz is shown in figure 5.5. The capacitance was calculated to be 96.8 nF. The deviation of the capacitance from the correct value is 3.2%, which is slightly larger than that of nonlinear fitting.

In conclusion, the above measurements on the SMD circuits indicate that the two-wire mode of the ETO system is appropriate for the AC electrical measurement of capacitance of devices with the resistance at least 100 MΩ and the capacitance around 1 nF. If the contact resistance of PCMs samples is as good as the SMD, this method should work well for measuring the dielectric constants of amorphous PCMs. The systematic accuracy of the capacitance is within 5%, which is accurate enough to determine not only the order of magnitude of the static dielectric constant, but also resolve trends in it.

The resistance of PCMs samples at 4 K is over 5 GΩ, which is impossible to be measured by the system. But it does not influence the accuracy of the capacitance measurement: As the capacitance is already the dominant part over most of the frequency range here, a higher resistance should not have any adverse effects.

A too high capacitance will eventually cause the current limit of the ETO to be exceeded, but the expected capacitance of real samples is expected to be of the order of 1 nF, which will not lead to such problems. Therefore, only capacitance is analyzed for PCMs samples to calculate the static dielectric constants.

5.3 AC Electrical Measurements on Amorphous Chalcogenides

The applied voltage in AC electrical measurements on amorphous chalcogenides is 0.01 V, which is the same as that in measurements of SMD samples. The thickness of amorphous chalcogenides vary from 100 nm to 1000 nm. Hence, the applied electric field on these materials is at maximum 0.1 V/μm, which is far less than their threshold electric fields, eg. GeTe (143 V/μm) and $Ge_2Sb_2Te_5$ (56 V/μm). It was mentioned in section 5.1 that AC electrical measurements on amorphous PCMs samples were conducted below 170 K, at temperatures above which the capacitive behavior of the PCMs cannot be well observed.

Two non-PCMs materials ($Ge_{15}Te_{85}$, GeSe) and five PCMs materials (GeTe, $Ge_8Sb_2Te_{11}$, $Ge_3Sb_2Te_6$, $Ge_2Sb_2Te_5$, $Ge_1Sb_2Te_4$) were studied in this section. As the capacitance is designed to be around 1 nF, all data are analyzed with the linear fitting of Im (*I*) using the RC model. Those results will be compared with the impedance measurement by VNA in Chapter 6.

5.3.1. Non-PCMs

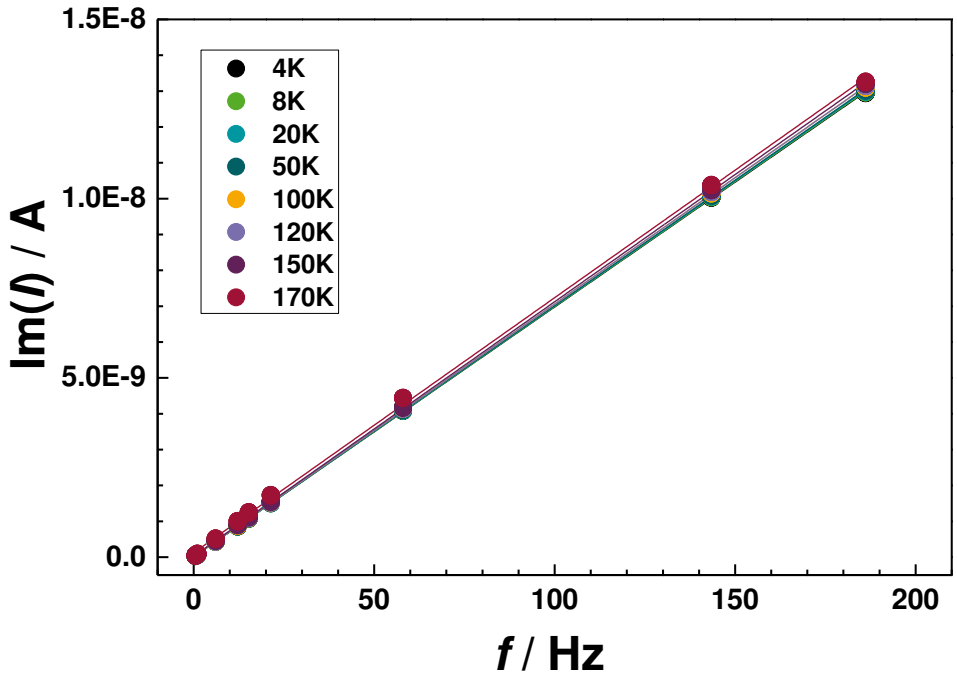

Figure 5.6 ***AC electrical measurements on the $Ge_{15}Te_{85}$ sample from 4 K to 170 K.*** *The thickness of the sample is 510 nm and the capacitor area is 2 × 2 mm^2. The imaginary part of current, Im(I), is plotted as a function of the frequency. The experimental and fitted data (according to equation 5.3) are shown in dots and lines, respectively.*

The results of AC electrical measurements on the $Ge_{15}Te_{85}$ sample are illustrated in figure 5.6. The layer stack of the sample is: Au / Cr / $Ge_{15}Te_{85}$ / Au / Cr / glass. The linear fitting looks very good. The capacitance of the $Ge_{15}Te_{85}$ sample measured at different temperatures are summarized in table 5.1.

Table 5.1 Capacitance of the amorphous $Ge_{15}Te_{85}$ sample measured at different temperatures by AC electrical measurements.

T / K	C / F
4	1.109E-9
8	1.111E-9
20	1.113E-9
50	1.115E-9
100	1.122E-9
120	1.126E-9
150	1.130E-9
170	1.133E-9

According to the capacitance in table 5.1 and the geometry size of the sample, the static dielectric constant of amorphous $Ge_{15}Te_{85}$ is calculated and plotted along with the temperature in figure 5.7. The data suggest an upward trend of the dielectric constant with increasing temperature. However, as this trend is very small (compared to the errors determined in the tests with SMD circuits), it cannot be ruled out that this is, at least partly attributed to the accuracy deterioration when the impedance approaches to 2 MΩ. On the other hand, the phonon frequencies are supposed to shift to lower frequencies at elevated temperatures [KE15]. According to the f-sum rules of phonons [Moli91]:

$$\sum_j \Delta\varepsilon_j \omega_{0j}^2 = \sum_j \frac{n_j q_j^2}{m_j} = const \qquad (5.5),$$

where ω_{0j} represents the phonon frequency, m_j is the effective mass and n_j is the number of phonons. Clearly, $\Delta\varepsilon_j$ increases if the phonon frequencies decrease. This is consistent with the experimental results.

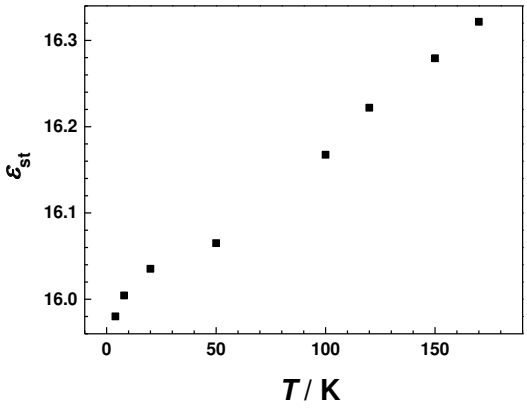

Figure 5.7 ***The dielectric constant of amorphous $Ge_{15}Te_{85}$ as a function of temperature****. It possesses an increasing trend with the temperature from 4 K to 170 K.*

In a similar way, the AC electrical measurements on GeSe were analyzed and summarized in the appendix A.

5.3.2 PCMs

While for the DLIA samples of non-PCMs, the electrodes were made of gold (and chromium), this metal is well known to easily migrate into chalcogenides. Since some of the PCM samples had to be heated for annealing studies, alternatives have been investigated. TiN thin film is frequently used to prevent gold diffusion, as it turned out to be conductive enough to work as an electrode. Therefore, TiN was inserted between the PCMs and gold layer as an anti-diffusion layer, with Ti as the adhesion layer. As a consequence, the samples were structured, from the top to the bottom, as Au / Cr / Ti / TiN / PCM / TiN / Ti / Au / Cr / glass substrate.

This following discussion will focus on the GeTe sample with the classic gold electrode and a reference sample of the new electrode stack. Other PCMs have been studied as well, they are briefly discussed in the summary with more data shown in the appendix A. Capacitances of amorphous GeTe samples measured by AC electrical measurement at varied temperatures are listed in table 5.2. Combining the capacitances and the geometry size of two samples, the static dielectric constants ε_{st} are calculated and plotted in figure 5.8.

Table 5.2 Capacitances of amorphous GeTe samples measured by AC electrical measurement at selected temperatures between 4 K and 120 K. One sample has gold electrode (thickness: 204 nm, area: 2 × 2 mm^2) and the other has the new electrode stack (thickness: 463 nm, area: 2 × 2 mm^2).

***T* / K**	***C* / F (Au)**	***C* / F (TiN)**
4	3.521E-9	1.815E-9
10	3.539E-9	1.839E-9
20	3.572E-9	1.866E-9
50	3.655E-9	1.912E-9
80	3.749E-9	1.946E-9
100	3.861E-9	1.969E-9
120	4.136E-9	1.997E-9

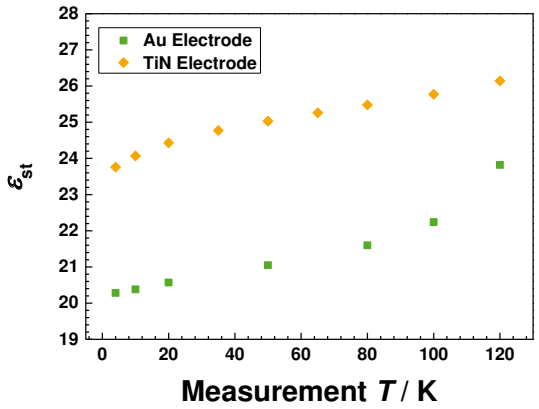

Figure 5.8 ***The static dielectric constants ε_{st} of amorphous GeTe from 4 K to 120 K.*** *The ε_{st} of GeTe sample with the new electrode stack at 4K is larger than that of the sample with classic gold electrode by 17%. The difference of ε_{st} between the two samples is attributed to the oxidation problem of the TiN /Ti layer and mismatched electrodes.*

Firstly, the temperature dependence of the dielectric permittivity of amorphous GeTe samples with the classic gold electrode is discernible. The ε_{st} of amorphous GeTe increase by 17.5% from 4 K to 120 K, while that of amorphous $Ge_{15}Te_{85}$ only increase by 1.5% in the same temperature range. The conductivity of amorphous GeTe is much larger than that of amorphous

$Ge_{15}Te_{85}$ at the same temperature, which means the transition frequency of amorphous GeTe is larger than that of amorphous $Ge_{15}Te_{85}$. Hence, the dielectric constant of amorphous GeTe can only be measured in a lower temperature region.

Secondly, the static dielectric constant of amorphous GeTe samples determined from the sample with TiN anti-diffusion layer is higher than that of normal samples. It is noteworthy that, after the preparation of TiN/Ti layer in the bottom electrode, the sample needs to be taken out of the chamber to change the shadow mask for the layer of PCMs. After sputtering the layer of Ti/TiN for the top electrode, the sample is also exposed to the atmosphere during transfer from the sputtering chamber to the evaporation chamber. Hence, on the surface of TiN in the bottom electrode and Ti in the top electrode there is a very thin oxidation layer. In addition, there is little mismatch between the layer of TiN/Ti and gold because the incidence direction of sputtered particles is wider than that of the evaporation process, although they use the same shadow mask. The mismatch makes the effective area of capacitors larger than the expected value. Both of the abovementioned defects will contribute to the gap between the dielectric constants of GeTe samples with classic gold electrode and with the new electrode stack.

5.3.3 Aging Effect

All glasses possess aging phenomena, and the aging process is accelerated at elevated temperatures. As a prototypical PCM, the property changes of amorphous GeTe thin films that accompany aging have been studied by the density functional theory (DFT) calculations [RZL+15] and the photothermal deflection spectroscopy [Luck12]. Here it is elucidated by the AC electrical measurement. For this purpose, samples of GeTe thin films were annealed for one hour at successively higher temperatures and studied by AC electrical measurement at temperatures from 4 K to 120 K. Those annealed samples are in the amorphous state. The obtained dielectric permittivity of GeTe is plotted as a function of the annealing temperature in figure 5.9. The aging process possesses a monotonous decrease of the static dielectric constant measured at the same temperature.

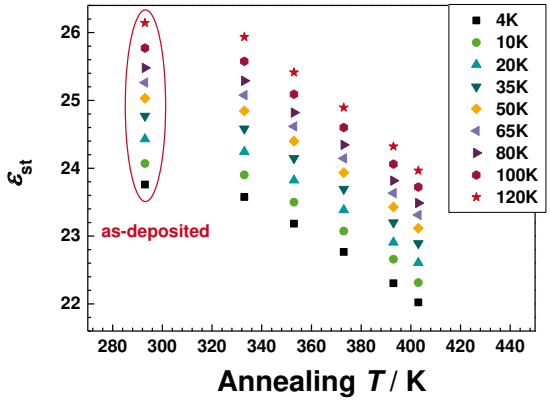

Figure 5.9 ***The static dielectric constants of the amorphous GeTe sample with the new electrode stack*** *measured by AC electrical experiment from 4 K to 120 K are plotted as a function of the annealing temperature. The sample was annealed for one hour at successively higher temperatures, i.e. 333K, 353 K, 373 K, 393 K, 403 K. The values measured at different temperatures are labeled with different symbols in the legend.*

In the thesis of Stephan Kremers [Krem09], the optical dielectric function of the amorphous GeTe thin film after heating treatment was studied and shown in figure 5.10. The value of ε_∞ (ε_1 at 0.05 eV) decreases with the increasing annealing temperature. This trend is consistent with the aging mechanism revealed by the DFT calculation [RZL+15], in which the ε_∞ of GeTe decreases from 22.6 to 16.7 after aging. The Peierls distortion becomes more prominent in the relaxed state after annealing, which leads to a larger bandgap [RZL+15, KBJ+14]. Through the Penn model, see equation (5.6), the optical dielectric constant and the band gap are linked [Penn62].

$$\varepsilon_\infty = 1 + \left(\frac{\hbar \Omega_p}{E_g} \right)^2 \qquad (5.6),$$

where Ω_p is the plasma frequency defined by harmonic oscillators from (2.24). The larger the bandgap E_g, the smaller the optical dielectric constant ε_∞.

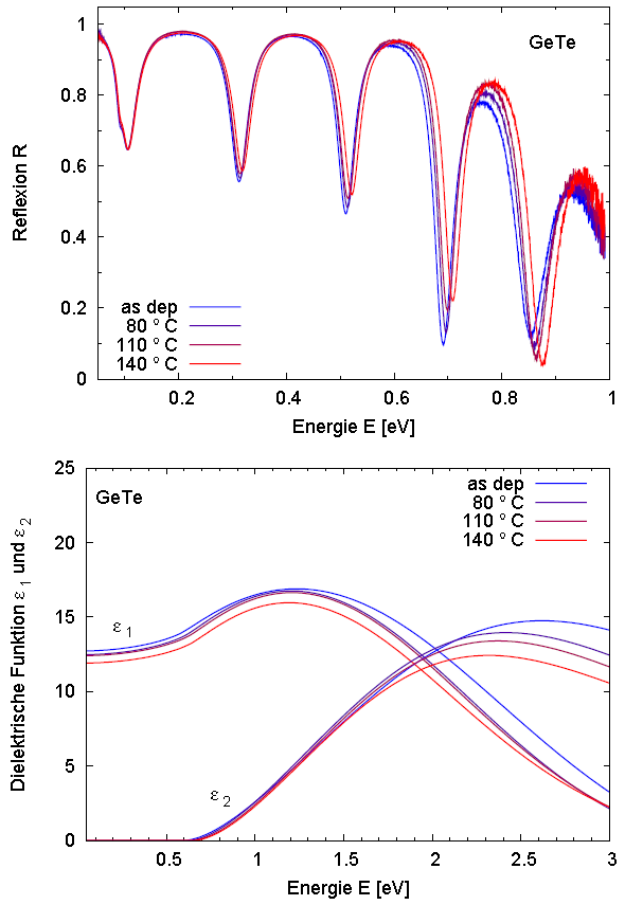

Figure 5.10 ***Top: Reflection spectra at room temperature of GeTe thin films*** *(layer thickness: 0.81 µm, Substrate: Aluminum) show a dependence on the thermal treatment T (heating rate 5 ˚C/min, heating time 30 min).* ***Bottom: The dielectric functions****, derived from fitting the model in equation (3.19) to the FT-IR spectra and additional ellipsometry spectra (65˚ and 75˚), shows the effect on the interband transitions and the optical dielectric constant. Reprinted from [Krem09].*

Furthermore, the static dielectric constant ε_{st} of one material is related to its optical dielectric constant ε_{∞} using the formula [GL97],

$$\varepsilon_{st} = \varepsilon_{\infty} + \frac{4\pi}{\Omega}\sum_{i}\frac{(Z_i^*)^2}{\omega_i^2} \qquad (5.7),$$

where the sum extends over all polar vibrational modes i, ω_i is the frequency of the mode and Z^* is the Born effective charge of the corresponding vibrational mode. Ω is the unit cell volume. The definition and derivation of the Z^* have been introduced in section 2.3.

The significant decrease of the static dielectric constant was attributed to changes in bonding [RZL+15]. DFT calculations show that the aging process of GeTe is not only characterized by the disappearance of tetrahedral Ge (Ge^T) bonds, but also the transition from four-fold coordinated octahedral Ge (Ge^H) bonds to three-fold coordinated Ge (Ge^{III}) bonds with three rigid bond angles around 90°. This phenomena indicates the local coordination is more crystal-like on aging. The bond around Ge^H is more polarizable than the bond around Ge^{III}, which is again more polarizable than the bond around Ge^T. As the bonds around Ge^T atoms are shorter and less polarizable than that around Ge^H and Ge^{III} atoms, the disappearance of Ge^T leads to an increase of Z^*, which however is overwhelmed by the decrease of Z^*caused by the transition from Ge^H to Ge^{III}.

Therefore, the decrease of ε_{st} originates from both the reduction of ε_∞ and Z^*. It is revealed by the DFT calculation [RZL+15] that the simulated ε_{st} of the melt-quenched GeTe decreases from 34.1 to 25.6 for the more relaxed GeTe. The ε_{st} determined by the DFT calculations decreases by around 28%, while it drops by about 9% from the AC electrical experiments. The disparity between the theoretical calculation and the experiments is attributed to different aging stages. The DFT calculations generate only the representative amorphous model of the various aging stages, which have no access to the time scale of the relaxation process.

To sum up, both DFT calculations and experiments show that the dielectric properties of the amorphous phase on aging become increasingly dissimilar from those of the crystal, in other words, the amorphous state ages away from the crystal.

5.4 Conclusions

AC electrical measurement using the high impedance mode of the ETO option in the PPMS is demonstrated to be a valid method for the low-capacitance measurement. Low-frequency dielectric constants, ε_{st}, of five amorphous PCMs as well as two non-PCMs over the temperature

range from 4 K to 120 K have been determined by AC electrical measurement and summarized in table 4.4.

The ε_{st} of amorphous PCMs along the pseudo-binary line between GeTe-Sb_2Te_3 climbs up with the increasing content of Sb_2Te_3, because Sb-Te bond is more polarizable than Ge-Te bond. In addition, the trend of ε_{st} rising with the measurement temperature is observed, which was discussed together with the temperature dependent behavior of ε_{∞}. The ε_{st} increase with temperature is mainly because the polar phonon contribution is strengthened at enhanced temperatures, while the increase of ε_{∞} is attributed to the shrinkage of bandgap. Hence, measured variations of ε_{st} with temperature should be attributed to variations in the energy of infrared phonons.

Lastly, contrast to Zachariasen glasses, the dielectric property of amorphous GeTe drifts away from the crystalline state, which is consistent with the DFT calculations. The aging process of amorphous GeTe is characterized with more prominent Peierls distortion and the decrease of ε_{st}.

Table 4.4 Static dielectric constants ε_{st} of amorphous chalcogenides measured at selected temperatures between 4 K and 120 K from 0.5 Hz to 186.2 Hz.

	GeTe	**Sb_2Te_3**	**ε_{st}**
GeSe	–	–	14.7 – 15.6
$Ge_{15}Te_{85}$	–	–	16.0 – 16.2
GeTe	**1**	**0**	20.3 – 23.8
$Ge_8Sb_2Te_{11}$	**0.89**	**0.11**	21.7 – 23.1
$Ge_3Sb_2Te_6$	**0.75**	**0.25**	24.9 – 26.4
$Ge_2Sb_2Te_5$	**0.67**	**0.33**	25.8 – 27.3
$Ge_1Sb_2Te_4$	**0.5**	**0.5**	32.7 – 35.2

VNA Impedance Measurement

The impedance measurement in this thesis is based on the previous work of Kathrin Krüger [Krüg10] and Franziska Schlich [Schl12]. From their work, the AC conductivity and dielectric function were dependent on the device size, which hinted at sample defects. In this work, samples are optimized in section 4.4.5 and more PCMs along the pseudo-binary line between GeTe-Sb_2Te_3 are studied by the impedance measurement.

This chapter starts with the derivation of the dielectric function and the AC conductivity from the impedance spectroscopy. The validity of the impedance measurement on the amorphous PCMs is demonstrated in considerable detail in section 6.2. The third part of this chapter is most important for this work. The AC conductivities and dielectric permittivities of amorphous PCMs are derived from the two-port impedance measurements from 9 kHz to 3 GHz at room temperature. The electrical transport mechanism of amorphous PCMs thin films at room temperature is concluded from the frequency dependence of the AC conductivity. The permittivities of amorphous PCMs at room temperature will be compared with the results of FT-FIR spectroscopy in the next chapter. Afterwards, the results of temperature dependent impedance measurements are analyzed. The temperature dependence of the permittivity in radio frequencies is investigated for comparison with the result of the AC electrical measurements at frequencies close to DC in the previous chapter. Furthermore, the activation energy is derived from the temperature dependent AC conductivity.

6.1 Equivalent Circuit of the VNA Samples

The technique of the impedance measurement in radio was explained in section 3.3. The finite conductivity of the electrode accounts for a small contact resistance R_0 with a few Ohms. Different to the equivalent circuit of PPMS samples in the AC electrical measurement in figure 3.1, R_0 of VNA samples involved in the impedance measurement should not be ignored. It is included in the equivalent circuit in figure 6.1.

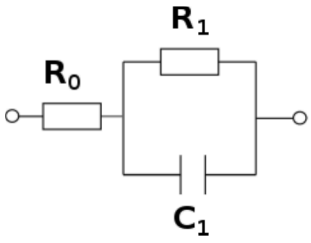

Figure 6.1 ***Equivalent circuit for VNA samples with the sandwich structure****. R_1 and C_1 refer to the resistance and the capacitance of PCMs, respectively, whereas R_0 denotes the contact resistance.*

Thus, the complex impedance of the equivalent circuit in figure 6.1 can be expressed by

$$Z_{DUT} = R_0 + \frac{R_1}{1 + i\omega R_1 C_1} \tag{6.1}.$$

Then the AC conductivity and the dielectric permittivity can be derived as follows:

$$\sigma_{AC} = \frac{d}{A} \cdot \mathrm{Re}\left(\frac{1}{Z_{DUT} - R_0} \right) \tag{6.2}$$

$$\varepsilon_r = \frac{d}{A} \cdot \mathrm{Im}\left(\frac{1}{Z_{DUT} - R_0} \right) \cdot \frac{1}{2 \cdot \pi \cdot f \cdot \varepsilon_0} \tag{6.3}.$$

The RC transition frequency of the above equivalent circuit is the same as equation (3.1).

6.2 Validation Experiments

As was already mentioned in the introduction, impedance spectroscopy can be easily distorted by sample imperfections such as insulating interlayers (e.g. oxide layers, lithography residuals), non-ohmic contacts, or pinholes. Indeed, the sample preparation was revised to eliminate the formation of highly-resistive interface layers. The presence of interlayers, broken contacts, or pinholes adds extra elements to the equivalent circuit shown in figure 6.1 and, thus, renders equations (6.1) and (6.2) invalid. As a consequence, erroneous results for $\varepsilon(\omega)$ and $\sigma(\omega)$ are

obtained. The following validation experiments, however, demonstrate that the revision of the sample preparation process was successful, i.e. that data in this work are not affected by such shortcomings.

6.2.1 DC Conductivity

The DC conductivity of the sandwich structures were probed using a source measure unit (Keithley SCS 4200) and a temperature controlled probe station. Figure 6.2 depicts the DC conductivity and its temperature dependence for a $Ge_3Sb_2Te_6$ sandwich structure. The data nicely follow the Arrhenius law

$$\sigma(T) = \sigma_0 e^{\frac{-E_A}{k_B T}} \tag{6.4},$$

where the activation energy E_A and the pre-factor σ_0 are 0.38 eV and 1236 S/cm, respectively. The room-temperature conductivity is $\sigma_{20°C} = 3\times10^{-4}$ S/cm. From *in-plane* samples, $E_A = 0.37$ eV was obtained, and depending on the thermal history of the film (resistance drift), $\sigma_{20°C} = 3.6\times10^{-4}$ S/cm [Schl12]. It is an excellent agreement between the sandwich structures and the in-plane samples. There can be no doubt that in-plane samples are less prone to be influenced by interface effects or contact effects. In addition, pinholes should not matter due to the lateral current flow. The fact that the electrical properties obtained from both geometries are in line is, therefore, strong evidence that the sandwich structures are *not* affected by these shortcomings. Hence, it is confirmed that the DC resistivity as well as its temperature dependence is perfectly in line with data obtained independently from in-plane measurements.

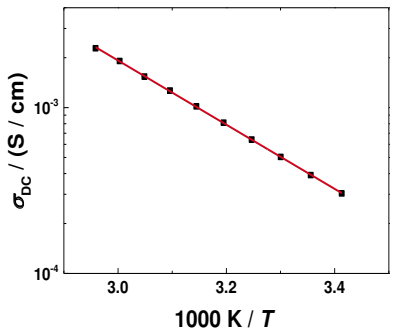

Figure 6.2 ***Temperature dependence of the DC conductivity σ_{DC} derived from an amorphous $Ge_3Sb_2Te_6$ sandwich structure****. The activation energy E_A and the pre-exponential factor σ_0 according to equation (6.4) are 0.38 eV and ~ 1236 S/cm, respectively.*

6.2.2 One-Port Impedance Measurement

The principle of the one-port impedance measurement has already been introduced in section 3.3.2.2. The one-port impedance measurement is made as a reference for the two-port impedance measurement. For the one-port impedance measurement, except for the less number of points (i.e. 201), other adjustments are the same as those of the two-port impedance measurement listed in table 3.2. The results of four devices with varied capacitor areas on the amorphous $Ge_3Sb_2Te_6$ sample are presented for the one-port impedance measurement. The real part of the impedance on the X axis and the imaginary part of the impedance on the Y axis constitute the Nyquist plots in figure 6.3. The complex impedance of those devices are obtained through fitting the Nyquist plots with semicircles. Given the geometry of the devices, the AC conductivity of the amorphous $Ge_3Sb_2Te_6$ film is determined by the real part of the impedance. The AC conductivity is plotted along with frequency and averaged to be 3×10^{-4} S/cm in figure 6.4. Furthermore, the permittivity of the amorphous $Ge_3Sb_2Te_6$ film is calculated with the imaginary part of the impedance and plotted as a function of frequency in figure 6.5. The dielectric permittivity of amorphous $Ge_3Sb_2Te_6$ stabilizes at different frequency ranges for devices with different areas and it is averaged to be 28.5. It can be seen from the result in figure 6.5 that the number of points is not enough for the one-port impedance measurement. The degree of accuracy of the one-port impedance measurement is less than the two-port impedance

measurement when the impedance is not close to 50 Ω. The two-port impedance measurement with larger number of points is recommend for this work.

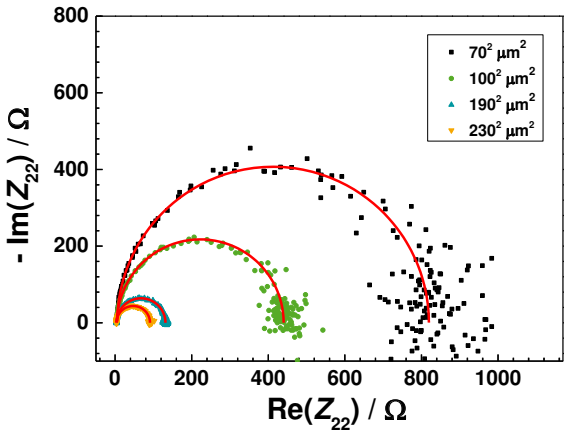

Figure 6.3 ***Nyquist plots of impedance of the amorphous $Ge_3Sb_2Te_6$ sample with a thickness of 150 nm.*** *Results of four devices with varied capacitor areas are plotted in different symbols labeled in the legend and fitted with semicircles in red lines. Data points of each device distribute around the corresponding semicircle. The complex impedance of different devices are obtained from the fitting curves.*

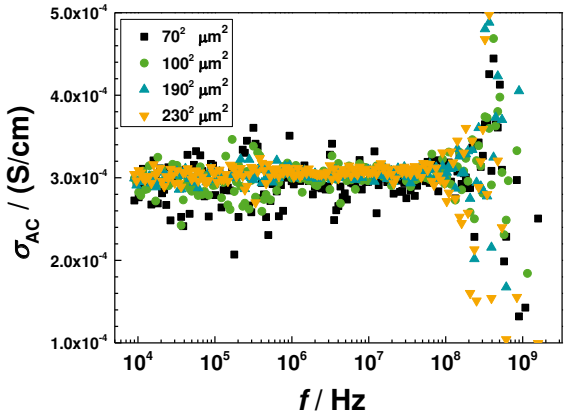

Figure 6.4 ***AC conductivity of the amorphous $Ge_3Sb_2Te_6$ sample as a function of frequency.*** *The σ_{AC} is frequency independent below 10^8 Hz. The σ_{AC} coincides over different areas and is averaged to be 3 × 10^{-4} S/cm. The independence of σ_{AC} with the capacitor area rules out interface problem.*

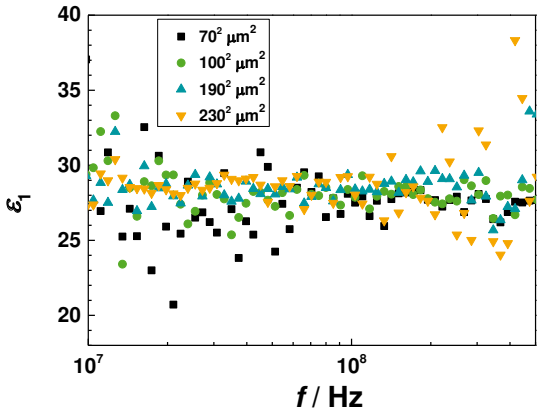

Figure 6.5 ***The permittivity of amorphous $Ge_3Sb_2Te_6$ sample as a function of frequency.*** *The larger the capacitor area, the lower the frequency that the permittivity becomes stable. The measurement noise of the device with 190^2 µm^2 and 230^2 µm^2 is fewer than that of the device with 70^2 µm^2 and 100^2 µm^2 because the device impedance of the larger areas are closer to 50 Ω.*

6.2.3 Applied Electric Field

Threshold switching will happen in the amorphous PCMs, if the applied electric field reaches the threshold fields of the PCMs. To exclude a non-linear behavior of PCMs during the two-port impedance measurement, the applied electric field on the PCMs is calculated from the applied power P_{in} and S-parameters [Schl12]. Firstly the absorbed power of the device P_{abs} is calculated by

$$P_{abs} = P_{in}\left(1 - |S_{11}|^2 - |S_{21}|^2\right) \tag{6.5}.$$

Substitute equations (3.8) and (3.9) into (6.5), one gets

$$P_{abs} = P_{in}\left(1 - \frac{Z_{DUT}^2}{(Z_{DUT} + 2Z_0)^2} - \frac{4Z_0^2}{(Z_{DUT} + 2Z_0)^2}\right) \tag{6.6},$$

where Z_{DUT} denotes the impedance of the device. The applied power P_{in} is an averaged effective power instead of the maximum power, so the peak of the absorbed power should be $P_{max}=2P_{abs}$, from which the peak of the applied voltage U_{max} can be derived by

$$U_{max} = \sqrt{P_{max} Z_{DUT}} = \sqrt{2P_{abs} Z_{DUT}} \tag{6.7}.$$

And then the peak of the applied electric field can be obtained

$$E_{max} = \frac{U_{max}}{d} = \frac{\sqrt{2P_{abs} Z_{DUT}}}{d} \tag{6.8},$$

where d is the thickness of the PCMs. Substituting equation (6.6) into equation (6.8), one gets

$$E_{max} = \frac{\sqrt{8Z_0 P_{in}}}{d} \frac{Z_{DUT}}{Z_{DUT} + 2Z_0} \tag{6.9}.$$

Supposing P_{in} = 0.1 mW, Z_0 = 50 Ω, d = 150 nm, then the peak of the applied electric field is always below 1.33 V/µm, independent of the device impedance. The threshold electric field of $Ge_2Sb_2Te_5$ is known to be 56 V/µm [KRR+09] and that of GeTe is 143 V/µm [RCD+11]. The threshold electric field of other PCMs and non-PCMs studied in this work are likely to have the same order of magnitude. Hence, the applied electric fields in the measurement are expected to be safely below the threshold fields of the investigated materials and all devices should stay in the linear region. In figure 6.6 the maximum electric fields applied to the $Ge_2Sb_2Te_5$ sample are plotted along with frequency for four devices with different capacitor areas.

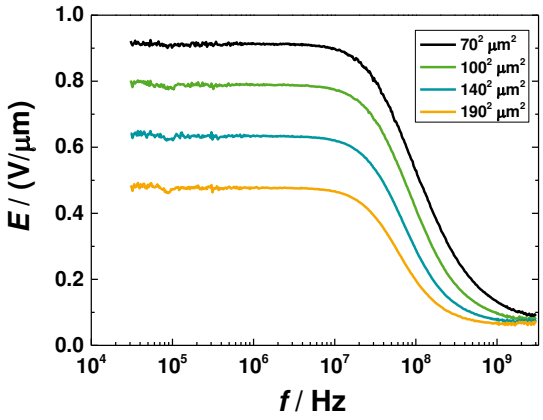

Figure 6.6 ***The maximum electric fields applied to the amorphous $Ge_2Sb_2Te_5$ sample with four different capacitor geometry sizes as a function of frequency.*** *The smaller the capacitor area is, the larger the electric field is dropped on the device. The maximum applied electric field on the sample is far less than the threshold field of $Ge_2Sb_2Te_5$.*

6.2.4 Phase Error

From the two-port impedance measurement on the calibration structures of the investigated samples, it is known that there was inevitable miniscule phase error in the transmission mode at the high frequency end. However, owing to the superior signal-to-noise ratio, we resorted to the transmission data in the course of the analysis. As is exemplarily shown for a device of amorphous $Ge_3Sb_2Te_6$ in figure 6.7, the impedance $|Z_{11}|$ derived from the reflection S-parameters S_{11} are in line with the impedance $|Z_{21}|$ obtained from the transmission S-parameters S_{21}. The phase error becomes prominent only above 100 MHz and reaches 60° at 3 GHz. It is reasonable to conclude that the impedance measurements are reliable below 100 MHz. In addition, the analysis of the transmission signals in the two-port measurement using equation (3.10) is preferred because it is less noisy.

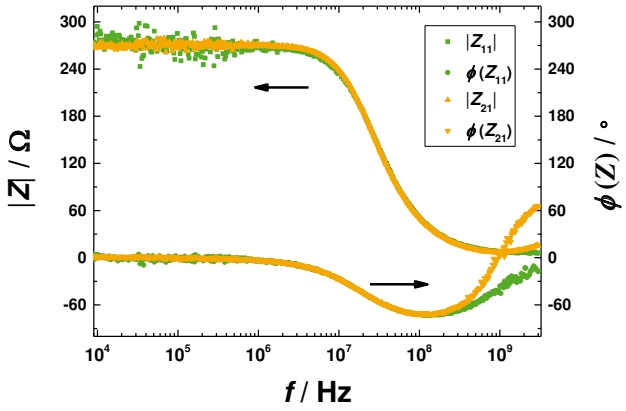

Figure 6.7 ***The comparison between the impedance of an amorphous $Ge_3Sb_2Te_6$ device determined by the reflection S-parameters and the transmission S-parameters: (Left) Impedance magnitude; (Right) Impedance phase angles.*** *The thickness of the amorphous $Ge_3Sb_2Te_6$ thin film is 150 nm and the capacitor area is 140^2 μm^2. The impedances from both S-parameters coincide with each other, except for the deviation of the phase angle above 100 MHz.*

6.2.5 Interfacial Defects

This section presents an example of the impedance spectroscopy obtained from a sample without optimization steps where shortcomings in the device fabrication lead to extremely pronounced interface effects. A single RC element produces a semicircle in a Nyquist plot [MJ05], which is expected from equation (6.1) and figure 6.1. However, in striking contrast to figure 6.3, two semicircles are clearly discernible in the Nyquist plot for the impedance of the amorphous $Ge_3Sb_2Te_6$ sample in figure 6.8. This pattern can be understood in terms of a two-RC model shown in figure 6.9, where the additional RC circuit comprised by R_2 and C_2 represents highly resistive interface layers at the electrodes. The impedance of the equivalent circuit employing the two-RC model is expressed as equation (6.10).

$$Z_{DUT} = R_0 + \frac{R_1}{1 + i\omega R_1 C_1} + \frac{R_2}{1 + i\omega R_2 C_2} \tag{6.10}$$

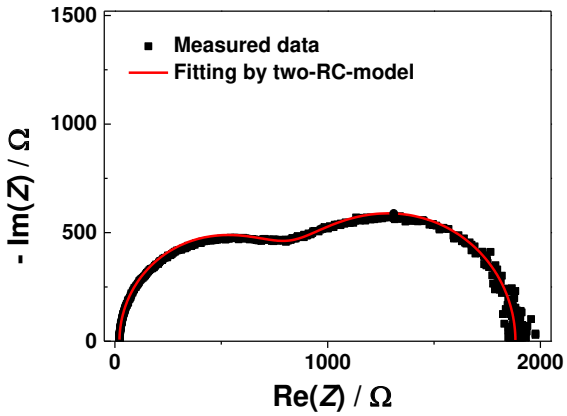

Figure 6.8 ***Nyquist plot of the impedance of amorphous $Ge_3Sb_2Te_6$.*** *The thickness and the area of the capacitor device are 150 nm and 70^2 um^2. The dot denotes the measured data and the red line represents the fitting result by the two-RC model.*

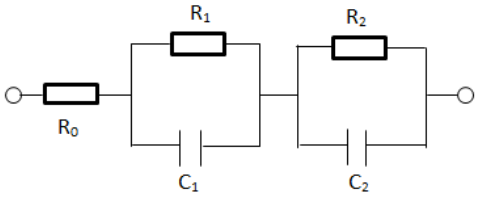

Figure 6.9 ***Equivalent circuit of samples with interface defects****. R_0 denotes the contact resistance, R_1 and C_1 refer to the capacitance and the resistance of PCMs, whereas R_2 and C_2 represent the capacitance and the resistance of the contamination layer.*

The conductivity and permittivity derived from the two-RC model are much different to the values analyzed in terms of the one-RC model, i.e., if the interface layer is simply neglected, the curves of the AC conductivity and the permittivity are calculated from equation (6.2) and equation (6.3), respectively. The conductivity is plotted in figure 6.10 and the permittivity is plotted in figure 6.11. The data determined by the one-RC model and the two-RC model are presented in the color of green and orange, respectively. The orange curves were obtained from a different procedure: First, reasonable fit parameters for R_2 and C_2 were determined. Then, the impedance of the 2nd RC element was subtracted from Z_{DUT} prior to the application of equation (6.2) and (6.3). Apparently, this correction can at least partially remove the erroneous trends

introduced by the interface layer. These data strikingly demonstrate that correct material properties can only be obtained if interface effects are absent. Please note that, in order to highlight the effect of interface layers, a rather extreme example was presented here. Prior to the revision of the sample preparation process, several cases where shortcomings in the sample preparation lead to much weaker interface effects have been encountered. In these less extreme cases, the fingerprints of the interface effects were less obvious: The Nyquist plot displayed a slightly deformed semicircle rather than two distinct semicircles and the apparent $\varepsilon(\omega)$ became frequency dependent. Thus, interface problems are not always as easy to detect as the Nyquist plot above suggests. Therefore, the verification experiments in this section were clearly mandatory.

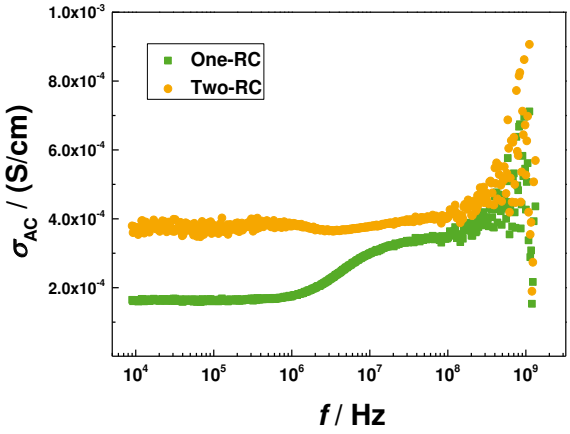

Figure 6.10 ***Comparison of the AC conductivity of amorphous $Ge_3Sb_2Te_6$ thin films determined by the one-RC model and two-RC model.*** *The AC conductivity by the one-RC model is frequency dependent and smaller than the value by the two-RC model, which however, is independent over the frequency.*

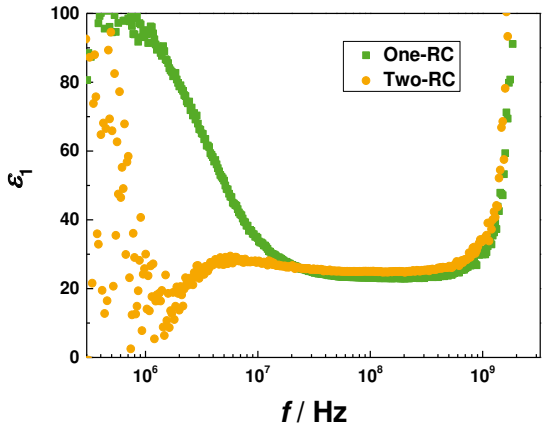

Figure 6.11 ***Comparison of the dielectric permittivity of amorphous $Ge_3Sb_2Te_6$ thin films determined by the one-RC model and the two-RC model.*** *The colossal dielectric permittivity by one-RC model at low frequencies is caused by the interfacial defects.*

Obviously, the interface layers lead to an *apparent* increase in the dielectric permittivity at low frequencies. The origin of the large values at the low frequency end is attributed to extrinsic contact effects, because they are dependent on the geometry size of the device. The importance of low frequency saturation dielectric constant in differentiating the spurious phenomenon from the bulk phenomenon is pointed out. A satisfactory model for the two mechanisms of $\sigma(\omega)$ in conventional band diagram of amorphous semiconductors is lacking. The boundary layer between the sample and electrode produces an electrode-polarization capacitance that must be removed from the measurement result. The model for spurious phenomenon can be extended by taking a combination of several capacitances and resistances to get any desired frequency dependence over a few decades of the frequency range. The resistance of electrode material and contact resistances also become very important at high frequencies in giving a frequency dependent conductivity.

6.2.6 Thickness Series

It was shown in the last subsection that the dielectric properties of the materials studied were seriously distorted by the interfacial effect. To ensure that the measured values represent the

bulk values, measurements should be made on samples with different thicknesses. The field throughout the bulk of the material should not be electrode limited but essentially uniform. If the permittivity is dependent on thickness, which suggests that the voltage drop occurs predominantly at one or both electrodes. If the surface barrier of electrode polarization effects dominate, usually the barrier capacitance is very large as compared to bulk, and then the numerical values of dielectric constant are also a good indication of the presence of barriers on a single thickness sample.

Three samples of amorphous $Ge_2Sb_2Te_5$ thin films with different thicknesses, i.e. 92 nm, 157 nm, and 184 nm, are prepared for the impedance measurement. There are 20 two-port-devices with different capacitor areas listed in table 4.1 on one substrate. The impedance measurement was conducted on those samples with different thicknesses and varied capacitor areas. As can be seen from figure 6.12, the impedance scales properly with film thickness and device area, i.e. ε_{st} shown in figure 6.13 does not depend on the particular thickness and area of the sandwich device. Furthermore, the linear relation between C/ε_0 and A/d, i.e. $C/\varepsilon_0 = \varepsilon_r (A/d)$ is displayed in figure 6.14. Data points are fitted with a line. The small variation of the dielectric permittivity discernible in figure 6.14 amounts to 5%. The error of the geometry size can readily account for this variation.

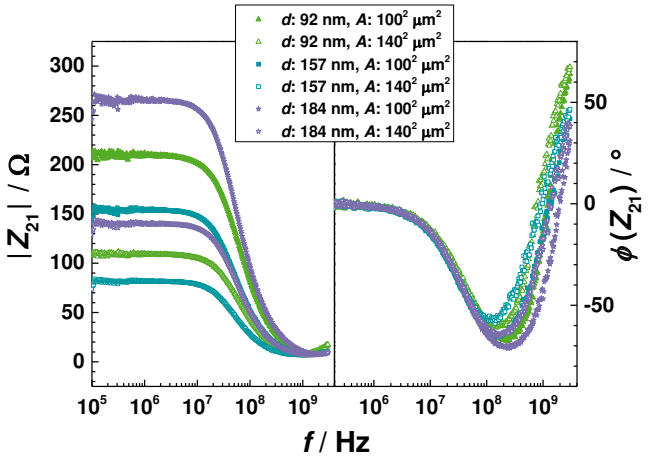

Figure 6.12 ***The magnitude (left) and phase angles (right) of the impedance determined by the transmission S-parameters.*** *Results are compared among six devices of amorphous $Ge_2Sb_2Te_5$ with different capacitor areas and thicknesses.*

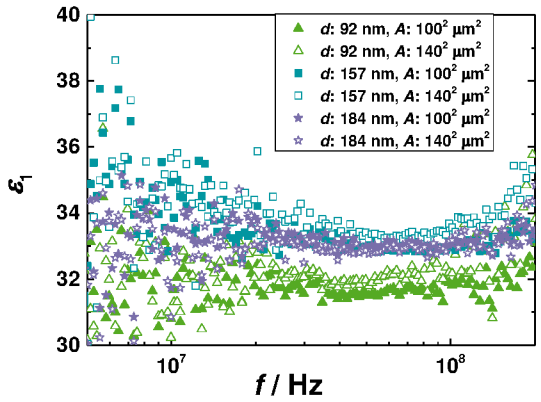

Figure 6.13 ***Dielectric permittivity of amorphous $Ge_2Sb_2Te_5$ in the frequency range between 5 MHz and 200 MHz.*** *Neither doubling the layer thickness d nor doubling the capacitor area A has a significant impact on the obtained permittivity.*

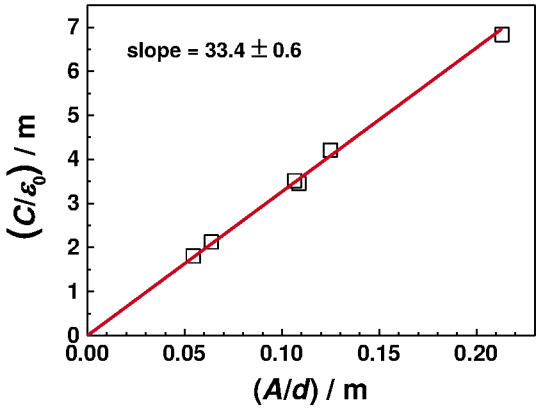

Figure 6.14 ***The graph displays C/ε_0 vs. A/d.*** *As expected, the data points obtained from different sample sizes are located on a straight line through the origin, where the slope of 33.4 ± 0.6 corresponds to ε_{st}.*

Similar to the approach behind figure 6.14, figure 6.15 verifies the scaling behavior of the resistance *R* of various $Ge_2Sb_2Te_5$ devices with different capacitor areas *A* and different thicknesses d of the PCM layer. It is demonstrated in figure 6.15 that the device resistance scales properly with thickness and area. However, owing to the already mentioned resistance drift, the error bars are slightly larger in this case. If the data were distorted by interface effects or contact

problems, the results should depend on the film thickness. The good agreement between data obtained from devices with different thicknesses of the PCM layer again indicates the absence of interface and contact problems. Therefore, the device properties scale as expected with film thickness and device area, which indicates that the measurements are not affected by interface effects, non-ohmic contacts or pinholes.

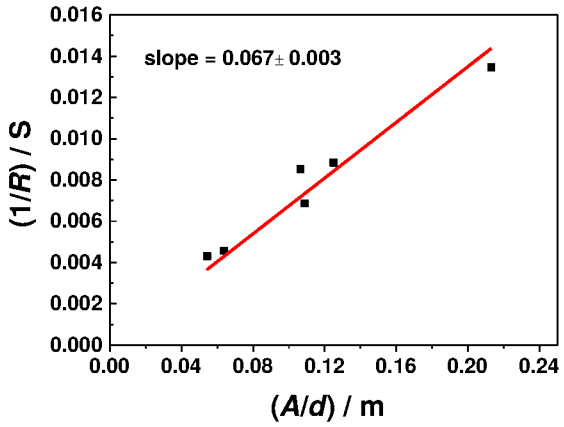

Figure 6.15 ***The graph displays 1/R vs. A/d.*** *As expected, the data points obtained from different sample sizes are located on a straight line through the origin, where the slope of 0.067±0.003 corresponds to the value of the AC conductivity.*

As could be expected from the relation $R^{-1} = \sigma A/d$, the plot of device conductance R^{-1} vs. geometry aspect ratio A/d yields a straight line through the origin, where the slope corresponds to the conductivity σ. Although both, the conductance data above and the capacitance data in figure 6.14, display the proper scaling behavior, there seems to be more scatter in the conductance data than in the capacitance data. This is most likely a consequence of the unavoidable variations in the resistivity of PCMs arising from the already mentioned phenomenon of resistance drift.

So far, the two-port impedance measurement has been verified to be an effective method to study the dielectric properties of amorphous PCMs.

6.3 Two-Port Impedance Measurement on Amorphous PCMs

The two-port impedance measurements were carried out on five amorphous PCMs along the pseudo-binary GeTe-Sb_2Te_3 line at room temperature. The thickness of all samples is 150 nm, except that of the $Ge_1Sb_2Te_4$ sample is 110 nm. Measurement results on devices with appropriate impedance are chosen to be presented in this section: devices with the area of 100^2 um^2 are chosen for the $Ge_1Sb_2Te_4$ sample, and devices with the area of 140^2 um^2 for all other materials. The amplitudes and phase angles of the transmission coefficients S_{21} are shown in figure 6.16 for the five amorphous PCMs.

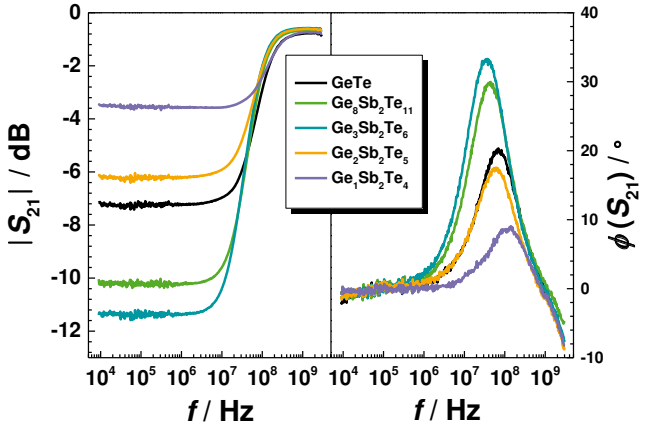

Figure 6.16 ***The transmission coefficients S_{21} in decibel and the phase angles of S_{21} for the five amorphous PCMs as a function of frequency.*** *The phase angles below 0˚ at the high frequency end indicates phase errors.*

From the transmission S-parameters, the impedances were calculated with the one-RC model using equation (3.10). The magnitude of the impedances over frequency are illustrated in the left half and the phase angles in the right part of figure 6.17. The impedances maintain a constant at low frequencies, because the resistor plays a leading role. As the frequency increases, the capacitor comes into play gradually and the impedance decreases with the frequency to until 6 Ω, which corresponds to the contact resistance. However, the impedances climb up slightly at the rightmost end. This rise results from an uncalibrated phase error in the system. The phase

error is attributed to the different lengths of waveguides between the two Z-probes. The phase error is obvious only at the highest frequency end and reaches around 60˚.

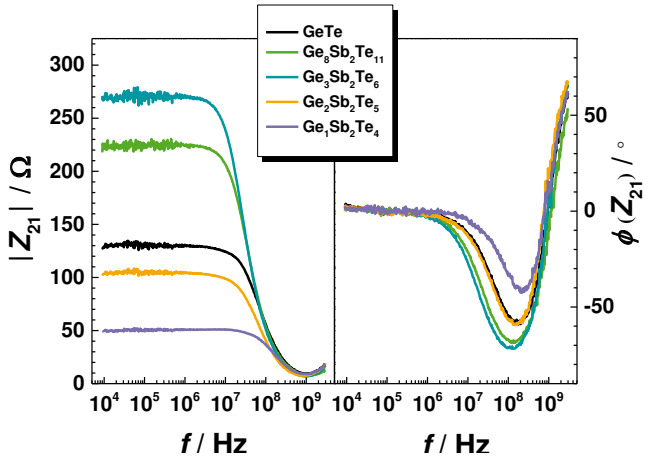

Figure 6.17 ***Bode plots of the impedance for the five amorphous PCMs.*** *(Left) the frequency response of impedance magnitude. (Right) the frequency response of the impedance phase angles.*

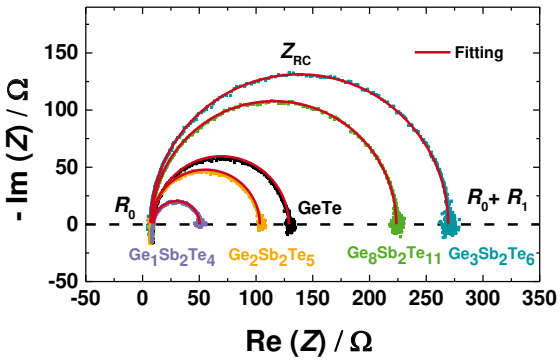

Figure 6.18 ***Nyquist plots of the impedance of the five amorphous PCMs.*** *X-axis: the real part of the complex impedance Re(Z). Y-axis: the imaginary part of the complex impedance Im(Z). The curves change from the rightmost point to the leftmost point as the frequency increases. Data points are fitted by semicircles in red lines.*

Figure 6.18 depicts Nyquist plots of the impedance spectroscopy data derived by equation (3.10) from the transmission coefficient S_{21}. Apparently, the data points are located on semicircles. Following the equivalent circuit described by figure 6.1 and equation (6.1), three cases are identified in terms of the frequency regimes: In the DC limit, the impedance is dominated by the resistance of the PCM layer R_1 and is, therefore, purely ohmic. If a contact resistance R_0 (in this case about 6 Ω) is taken into account, the DC limit reads: $Z_{st} = R_0 + R_1$. This corresponds to the rightmost point of the semicircle in figure 6.18. With increasing frequency, the transition to capacitive behavior sets in as the capacitor C_1 becomes conductive. The transition frequency f_{RC} (see equation (3.1)) corresponds to the topmost point of the semicircle: $Z_{RC} = R_0 + (1\text{-i})\, R_1/2$. Here, the equal contributions of R_1 and C_1 to the current flow result in a phase angle of $-\pi/4$. In the high frequency limit, the contact resistor R_0 predominates and the behavior becomes ohmic again: $Z_\infty = R_0$.

The red lines in figure 6.18, representing fits to equation (6.1), indicate that the very simple model already offers a very accurate description of the data. The finding of the Nyquist diagram displaying only one semicircle is in striking contrast to literature data, where two semicircles are observed and consequently models comprised of two RC elements are invoked to interpret the data [PGL+13, LZZ+13]. The additional RC element is typically attributed to highly resistive contacts [MJ05] or to highly resistive grain boundaries [PGL+13, SKM+13, HHH12], where the latter of course only makes sense in crystalline systems. As the explanations for the additional RC element are somewhat awkward, it is comforting that the data reveal just one RC element.

The agreement with the one-RC model in figure 6.18 already suggests that $\sigma(\omega)$ is fairly frequency independent. In figure 6.19 and figure 6.20, the frequency dependence of $\sigma(\omega)$ and $\varepsilon(\omega)$ are derived by employing equations (6.2) and (6.3) from the experimental data. Figure 6.20 demonstrates that $\sigma(\omega)$ is frequency independent in the entire measurement range. At frequencies above 10^8 Hz, the capacitance C_1 dominates making the determination of R_1 and, thus, $\sigma(\omega)$ increasingly noisy. The absence of a frequency dependence is by no means trivial since this finding differs from the literature on other chalcogenides such as As_2Te_3 [Elli87]. If a frequency dependent conductivity (often of the type $\sigma \sim \omega^s$) is observed, this phenomenon is usually attributed to hopping transport [FAH05]. The “flat” conductivity spectra are perfectly

in line with charge transport in extended states at the mobility edge ("band transport"). Given the comparably high conductivities of amorphous PCMs, this picture seems plausible.

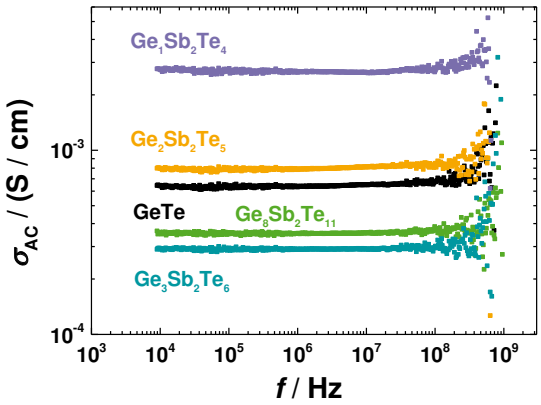

Figure 6.19 ***AC conductivities σ_{AC} of the five amorphous PCMs along with the frequency at room temperature.*** *In the entire frequency range, no frequency dependence is observed. This finding is in line with transport by extended states at the mobility edge.*

The frequency dependence of the AC conductivity $\sigma(\omega)$ and the dielectric permittivity $\varepsilon(\omega)$ are usually explained in terms of hopping transport and dielectric relaxations, respectively. The impedance spectroscopy data can be readily understood in terms of a single RC element comprised of a frequency independent resistor and a frequency independent capacitor, i.e. both, $\varepsilon(\omega)$ and $\sigma(\omega)$, do not display any frequency dependence in the impedance spectroscopy range (kHz to GHz). Hence, no evidence of relaxations or hopping transport was observed. Given the comparably high room-temperature conductivities of amorphous PCMs, the conjecture of transport by extended states at the mobility edge appears plausible.

Figure 6.20 presents the dielectric permittivity as derived from equation (6.3). Far below the transition frequency, the total impedance Z_{DUT} is dominated by the conductivity of the film ($\rightarrow R_1$) and, hence, no determination of the permittivity (C_1) is possible. At frequencies close to 3 GHz, Z_{DUT} is governed by the contact resistance R_0. Small errors in the determination of R_0,

therefore, have a large impact on $\varepsilon(\omega)$ in this region. In addition, miniscule length variations between the waveguide structure employed for calibration and the actual samples can give rise to phase errors in this region. The upturn of $\varepsilon(\omega)$ does, therefore, not reflect the actual frequency dependence. In the frequency range, where reliable data could be obtained, the dielectric permittivity is constant within the margin of error. This result is again not trivial.

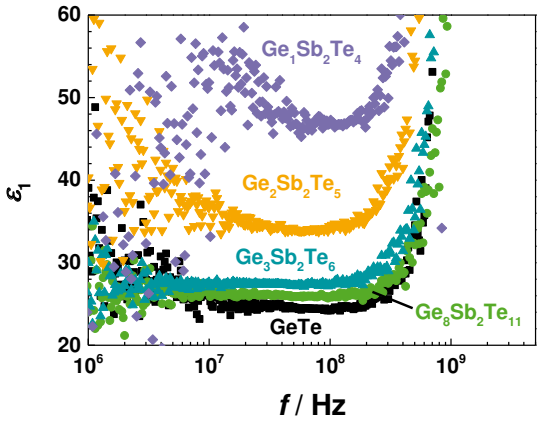

Figure 6.20 ***Dielectric permittivities ε_1 of the five amorphous PCMs along with the frequency.*** *The origin of the noise at low frequencies and the upturn at high frequencies is explained in the text. In the intermediate range, where reliable data could be acquired, no frequency dependence is discernible. The lower the conductivity of the material is, the broader the frequency range the dielectric permittivity can be measured over.*

In striking contrast to the existing literature, the static dielectric constant ε_{st} clearly exceeds the optical dielectric constant ε_∞ in the pseudo-binary GeTe-Sb_2Te_3 system, where ε_{st} increases continuously with increasing Sb_2Te_3 content. This study is the first experimental investigation reporting on the difference between ε_{st} and ε_∞ and the stoichiometry trend in the GeTe-Sb_2Te_3 system. These data on the static dielectric constant are expected to be of great help in modeling capacitive effects in PRAM device simulations or in gauging DFT structure models.

Sosso et al. [SCM+11] computed the Raman spectrum of crystalline and amorphous $Ge_2Sb_2Te_5$ using ab initio phonons and an empirical bond polarizability model. The consistency between the computed Raman spectrum and the experimental data confirms the reliability of the

polarizability model of amorphous $Ge_2Sb_2Te_5$. The bond polarizability model reveals the polarizability of the Sb-Te is much higher than that of Ge-Te bonds and of Ge-Ge/Sb homopolar wrong bonds. On the other hand, from EXAFS analysis, the bond distance of Ge-Te is shorter than that of Sb-Te [Zald12, KKF+11] and the bond strength of Ge-Te (402 kJ/mol) is stronger than that of Sb-Te (277.5 kJ/mol) [SKL+17]. Therefore the increase of the amount of the Sb-Te bond gives rise to higher static permittivities in amorphous PCMs along the pseudo-binary GeTe-Sb_2Te_3 system line.

6.4 Temperature Dependent Impedance Measurement

The impedance measurements on amorphous PCMs at room temperature hint that their AC conductivities are dominated by band transport. However, the hopping-type transport mechanism of the AC conductivity at lower temperatures was widely reported for amorphous chalcogenides, such as As_2Se_3 and In_2Se_3 [LA71, AS03, ABE+00]. Therefore, the impedance measurements were carried out over a wide temperature range to distinguish different electrical transport mechanisms in amorphous PCMs.

The temperature dependent impedance measurements were taken place in a vacuum cryostat (JANIS ST-500-2UHT). The interior structure of the probing station was introduced in the dissertation of Matthias Käs [Käs17]. Instead of one Z-probe connected with one high-frequency-arm used in Matthias' work, two Z-probes fixed onto two high-frequency-arms in the opposite position to the each other were used in this work. The chamber of the probing station is evacuated to pressures below 10^{-4} mbar and can be cooled down to 85 K by the flow of a cryogen (liquid nitrogen). Samples were mounted in the cryostat and connected to the outside VNA through the inside Z-probes and coaxial cables. This measurement was conducted between 220 K and 350 K limited by the temperature tolerance of Z-probes. Both of the rates of heating up and cooling down are 10 K/min and the measurement was carried out after temperature stabilization for 10 minutes. The impedance measurement system was only calibrated at room temperature due to the limited access time of the cryostat.

The AC conductivity of amorphous $Ge_3Sb_2Te_6$ at selected temperatures calculated from the impedance spectroscopy are plotted in figure 6.21, which is remarkable for the upturn of the

conductivity at high frequencies. The similar data of the temperature dependent AC conductivities of other amorphous PCMs are presented in the appendix B. The measured AC conductivity at low frequencies approaches the DC conductivity, while it is substantially higher than the DC conductivity after the upturn. The upturn point moves towards higher frequencies as the temperature increases, in other words, there is a decrease in the frequency dependence with the increasing temperature.

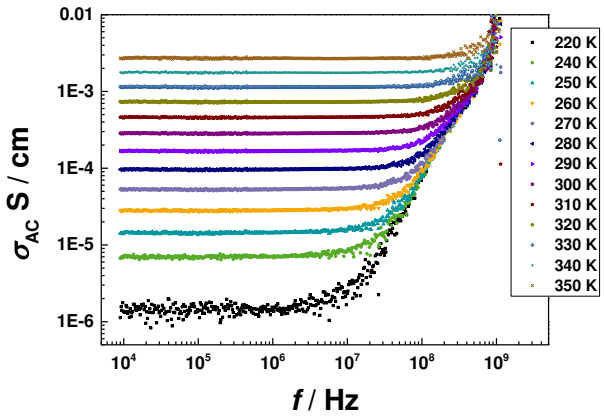

Figure 6.21 ***The AC conductivity of amorphous $Ge_3Sb_2Te_6$ measured by the impedance measurement from 220 K to 350 K.*** *The AC conductivities at different temperatures approach the same value asymptotically at the high frequency end. A decrease in the frequency dependence at higher temperatures was observed.*

It is well known that Z-probes, coaxial cables and the sample stage inside the probing station contract at lower temperatures and expand at higher temperatures, which contributes to the phase drift as temperature changes. Furthermore, the Z-probes are detached from the device every time after the measurement at one temperature. Varied touch-down points lead to varied distance for measurement at different temperatures, which also contributes to the phase error. It is difficult to make a conclusion whether the frequency dependence of the AC conductivity is caused by the systematic phase error, or hopping conduction mechanism. But it is still very interesting to note that the upturn point in figure 6.21 moves regularly to lower frequencies as temperature decreases.

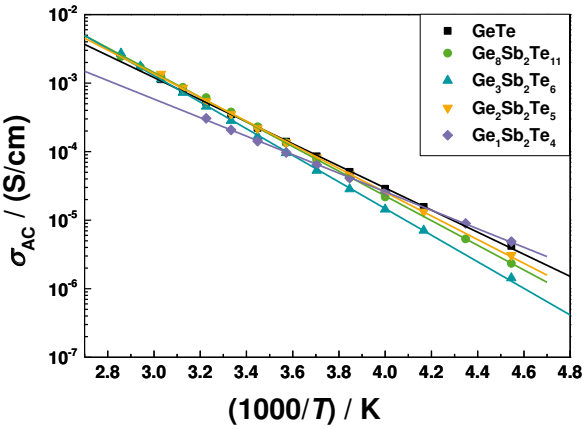

Figure 6.22 ***The temperature dependence of the AC conductivities of amorphous PCMs listed in the legend.*** *Only data meet the Arrhenius plot are presented: the range for $Ge_3Sb_2Te_6$ and $Ge_8Sb_2Te_{11}$ is 220 – 350 K, for GeTe and $Ge_2Sb_2Te_5$ is 220 – 330 K, and for $Ge_1Sb_2Te_4$ is 220 – 310 K. The activation energy of the AC conductivity from GeTe to $Ge_1Sb_2Te_4$ with increasing Sb_2Te_3 are 0.320 eV, 0.358eV, 0.386 eV, 0.343 eV, 0.269 eV, respectively.*

Although the upward trend of the conductivity in figure 6.21 is an open question, the constant part of the conductivity at low frequencies is reliable, because it is not sensitive to the phases of signals in the impedance measurement. The conductivity of each material is averaged in the constant region between 10^5 Hz and 10^6 Hz. The averaged conductivities were plotted as a function of temperature in figure 6.22, from which the activation energies E_A of the conductivity were derived. The Fermi energy of amorphous PCMs [HR10] was assumed to approximately pin at the middle of the energy gap, hence the bandgap can be estimated by $E_g \approx 2E_A$. The activation energy from the DC electrical measurement of the amorphous $Ge_3Sb_2Te_6$ from 293 K to 338 K in figure 6.2 is 0.38 eV, which is nearly the same as its activation energy of the AC conductivity from 220 K to 350 K in figure 6.22. The similar activation energy in different temperature regions hints at the same conductivity mechanism and the hopping transport above 220 K is negligible. However, the reason why the AC conductivity climbs up with frequency is still unclear. Therefore, the mechanism of AC conductivity at low temperatures needs to be further confirmed by adding the calibration process before conducting the impedance measurement at each temperature.

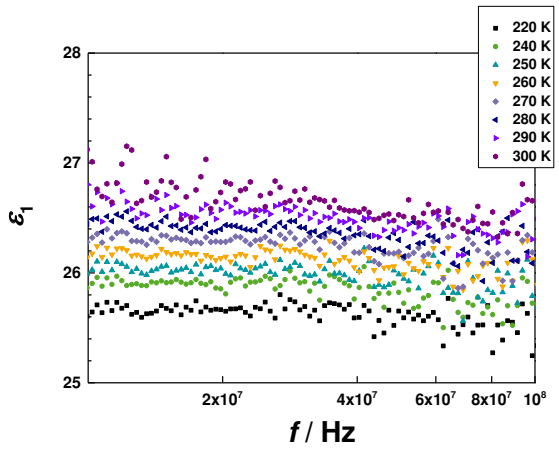

Figure 6.23 ***The temperature dependence of the static permittivity of amorphous $Ge_3Sb_2Te_6$ from 220 K to 300 K is presented between 10^7 Hz and 10^8 Hz.*** *The permittivity climbs up when the temperature increases.*

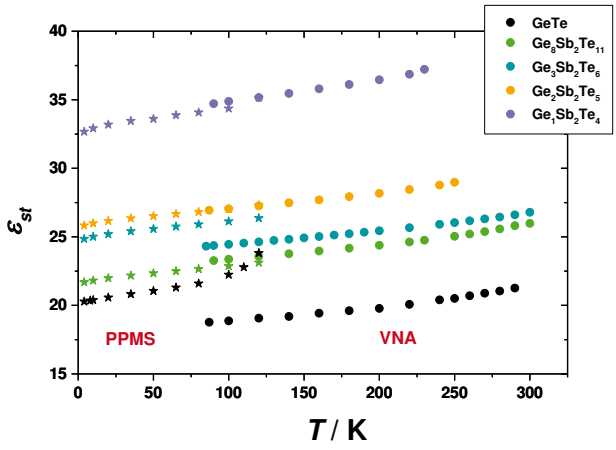

Figure 6.24 ***The temperature dependence of the static dielectric constant of the amorphous PCMs listed in the legend measured by PPMS and VNA.*** *Clearly the ε_{st} of the amorphous PCMs increase with the temperature.*

Moreover, the permittivity of amorphous $Ge_3Sb_2Te_6$ in radio frequencies is derived from the impedance spectroscopy between 220 K and 300 K, shown in figure 6.23. The permittivity increases monotonously with temperature. The permittivity obtained from the impedance measurement above 300 K does not make sense since the impedance is dominated by the

resistive element. The static dielectric constant ε_{st} of amorphous PCMs are averaged from the real part of their dielectric functions ε_1 at frequencies between 10^7 Hz and 10^8 Hz and plotted as a function of temperature in figure 6.24. The ε_{st} of all amorphous PCMs climb up with the increasing temperature. Some permanent dipoles are opposed to align in the field direction at higher frequencies at normal temperatures, while some dipoles will be facilitated at higher temperatures to oscillate at higher frequencies. This trend is consistent with the result in section 5.3.2, in which the temperature dependence of the permittivity was studied by the AC electrical measurement at frequencies close to DC. For comparison, those results are also plotted with the symbol of stars in figure 6.24. PPMS samples of GeTe and $Ge_3Sb_2Te_6$ used the structure in figure 4.4(a), while the structure of PPMS samples of $Ge_8Sb_2Te_{11}$, $Ge_2Sb_2Te_5$, $Ge_1Sb_2Te_4$ was improved to be with smaller error of capacitor areas shown in figure 4.4(c). Therefore, results of AC electrical measurements and impedance measurements on materials of $Ge_8Sb_2Te_{11}$, $Ge_2Sb_2Te_5$, $Ge_1Sb_2Te_4$ are more consistent with each other.

The temperature dependence of the optical dielectric functions of amorphous PCMs was studied by Kremers [Krem09] from 400 cm^{-1} to 8000 cm^{-1} (i.e. 0.05 eV to 1 eV) at selected temperatures between 5 K and 294 K. The results are shown in figure 6.25, in which a slight increase of the optical dielectric function with temperature was observed. By contrast, the increment of the static permittivity with temperature is much larger than that of the optical dielectric constant. According to Lowndes et. al. [LM70], the lattice potential energy of a perfectly harmonic crystal depends only on terms which are quadratic in the displacements of ions from their equilibrium positions, which means the energies of phonons in a perfectly harmonic crystal would be independent of temperature. However, there is always inharmonic effect in real crystals and amorphous states. The contributions of lattice vibrations to the dielectric constant ($\Delta\varepsilon$) would be clear after subtracting the purely electronic polarization, having $\Delta\varepsilon = \varepsilon_{st} - \varepsilon_\infty$. The increase of $\Delta\varepsilon$ with temperature hints the rising of the lattice contribution.

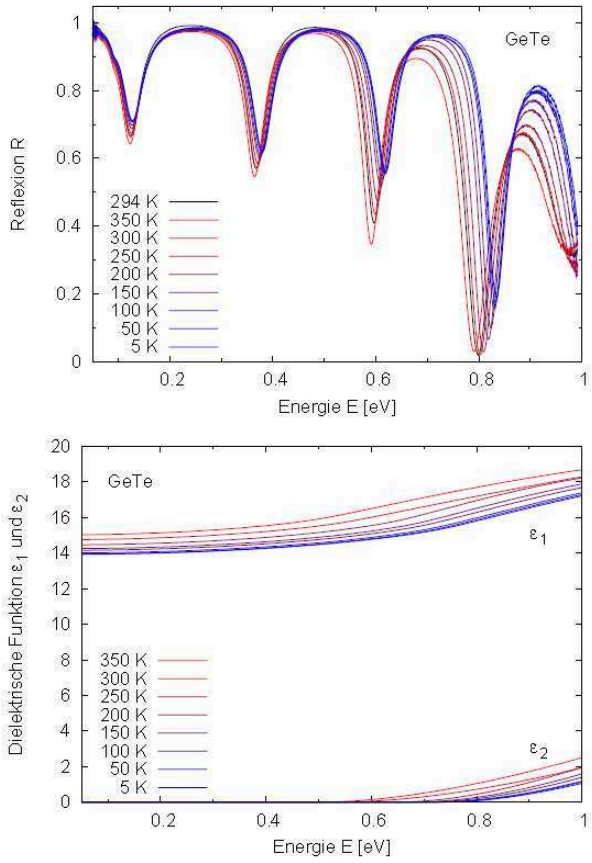

Figure 6.25 ***Temperature dependent infrared reflectance spectra (upper half) and dielectric function (lower half) of an amorphous GeTe film from 0.05 eV to 1 eV measured in a vacuum cryostat.*** *The low-temperature measurements show the purely electronic contribution to the temperature dependence of the optical properties. The sample consists of a PCM layer with a thickness of 640 nm on top of an aluminum reflector. Reprinted from [Krem09].*

6.5 Conclusions

The dielectric functions of amorphous PCMs thin films along the pseudo-binary line between GeTe-Sb_2Te_3 have been well studied by the impedance measurement in radio frequencies at varied temperatures. The impedance measurement fills an important gap in the available data. There is only minor discrepancy between the results of one-port and two-port impedance measurements. It has been pointed out in this chapter that the measurement of real part of the dielectric function ε_1, especially the low frequency saturation value ε_{st}, as a function of sample

thickness and temperature is very important in determining whether the measured dispersion is due to spurious or bulk effect. This work excludes the frequency dependence of the dielectric functions of amorphous PCMs in radio frequencies. Before sample optimization, extrinsic effects such as interfacial polarization attribute to a colossal dielectric permittivity at low frequencies. The results of the measurements on samples without the appropriate optimization can be interpreted more reasonably using the two-RC model.

Furthermore, the AC conductivities of amorphous PCMs at room temperature are dominated by the band transport, because they are frequency independent. The temperature dependence of the AC conductivities gives a deeper insight into the electronic system of the PCMs. The bandgaps of the five amorphous PCMs tend to drop with the increasing content of Sb_2Te_3. There is nearly no variations in the activation energy of amorphous PCMs between 220 K and 350 K being observed. Both of the static dielectric constant and the optical dielectric constant of amorphous PCMs possess a climbing trend with temperature. The increment of the static dielectric constant is larger than that of the optical dielectric constant in the same temperature range, which indicates the phonon contribution increases with temperature.

Finally, the AC conductivities and the dielectric permittivities of five amorphous PCMs by the impedance measurement at room temperature are averaged from the stable range of figure 6.19 and 6.20, respectively. The results are summarized in table 6.1.

Table 6.1 Summary of the impedance measurement results. The DC conductivities σ_{DC} at room temperature from in-plane samples, the DC conductivities and the static dielectric constant from impedance spectroscopy at room temperature of sandwich structures are listed. The energy bandgap is estimated from the activation energy of the corresponding AC conductivities. ([1] from [Volk13], [2] from [Schl12])

Quantity	σ_{DC}	σ_{DC}	E_g	ε_{st}
Unit	**S / cm**	**S / cm**	**eV**	
Structure	**In-plane**	**Sandwich**	**Sandwich**	**Sandwich**
GeTe	$(8\pm2)\times10^{-4}$ [1]	6.2×10^{-4}	0.76	24.4
$Ge_8Sb_2Te_{11}$	$(6\pm1.5)\times10^{-4}$ [1]	3.6×10^{-4}	0.72	25.8
$Ge_3Sb_2Te_6$	3.6×10^{-4} [2]	3.4×10^{-4}	0.66	27.4
$Ge_2Sb_2Te_5$	$(11\pm3)\times10^{-4}$ [1]	7.7×10^{-4}	0.68	34.0
$Ge_1Sb_2Te_4$	$(19\pm5)\times10^{-4}$ [1]	24.5×10^{-4}	0.54	47.0

Optical Measurement

Techniques and analytical methods of FT-IR reflectance and FT-FIR transmission were introduced in section 3.4 and the preparation of samples were described in section 4.6. This chapter is organized as follows.

FT-IR reflectance measurements on amorphous GeSe, $Ge_{15}Te_{85}$ and $Ge_2Sb_2Te_5$ are illustrated in section 7.1. As amorphous PCMs have been well studied by FT-IR reflectance measurements [SKW+08, Krem09], the same measurement is conducted on amorphous $Ge_2Sb_2Te_5$ in section 7.1 in order to clarify the reliability of the reflectance measurement on other amorphous chalcogenides, such as GeSe and $Ge_{15}Te_{85}$.

FT-FIR transmission measurements are carried out on PCMs and non-PCMs for both amorphous and crystalline states in section 7.2. The obtained dielectric permittivities are not only compared between PCMs and non-PCMs but also between amorphous and crystalline states of chalcogenides. The FT-IR reflectance spectra are analyzed with the Scout software, while the FT-FIR transmission spectra are simulated by a variational approach, which is equivalent to the Kramers-Kronig relation. The optical dielectric constants ε_∞ determined by the two methods are consistent with each other, which proves the applicability of both methods. It is reasonable to extrapolate the dielectric function from FT-FIR spectra to zero for the static dielectric constants when the contribution of all phonons is taken into account. The derived static dielectric constant ε_{st} of amorphous PCMs from the far-infrared transmission spectra are compared to the value measured by the impedance measurement in chapter 6.

7.1 Infrared Reflectance Measurement

The infrared reflectance spectra of amorphous GeSe, $Ge_{15}Te_{85}$ and $Ge_2Sb_2Te_5$ from 400 cm^{-1} to 8000 cm^{-1} (i.e. 0.05 eV to 1 eV, 12.1 THz to 241.8 THz) are shown in figure 7.1. The phonon contribution is excluded in the measurement region. The experimental and simulation curves are almost coincident, except for small deviation at the first valley of $Ge_{15}Te_{85}$ and $Ge_2Sb_2Te_5$,

which might come from the small error in the dielectric function of the aluminum mirror. It is difficult to determine the reflectance spectrum of the aluminum in this region exactly, when the reflectance is very close to 1.

The presence of the interference extrema in the reflectance spectra illustrates the structural perfection of the magnetron sputtered films. The reflectance maxima of all samples are close to 1 because there is no absorption by free carriers. The reflectance spectra of amorphous GeSe and $Ge_{15}Te_{85}$ are similar to that of amorphous $Ge_2Sb_2Te_5$, but the interference fringes of the GeSe spectrum extend to a significantly higher photon energy than that of $Ge_2Sb_2Te_5$ and $Ge_{15}Te_{85}$ due to a larger bandgap. The spacing (in frequency space) between the fringes of the reflectance minima is inversely proportional to the product of refractive index and film thickness: $\Delta f \propto 1/(n*d)$, where n is the refractive index and d is the film thickness. It can be seen in figure 7.1, the spacing of the reflectance minima of amorphous $Ge_{15}Te_{85}$ is about 1.2 times of that of amorphous $Ge_2Sb_2Te_5$. With the known thickness and the fringes spacing, the refractive index of amorphous $Ge_{15}Te_{85}$ is calculated to be slightly smaller than that of amorphous $Ge_2Sb_2Te_5$. As $\varepsilon_\infty = n^2$ when the absorption is zero, the optical dielectric constant of amorphous $Ge_{15}Te_{85}$ is supposed to be smaller than that of amorphous $Ge_2Sb_2Te_5$.

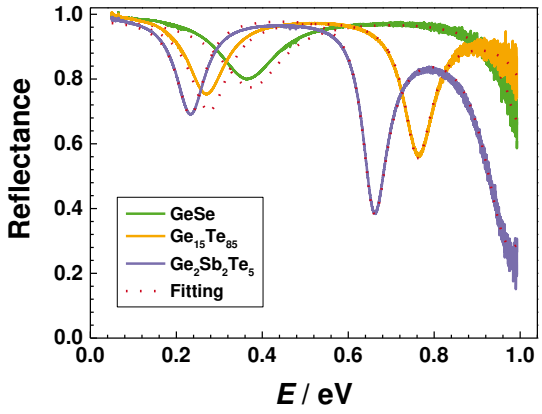

Figure 7.1 ***Reflectance spectra of amorphous GeSe, $Ge_{15}Te_{85}$ and $Ge_2Sb_2Te_5$ on the aluminum coated glass substrates from 0.05 eV to 1 eV.*** *The thickness of GeSe, $Ge_{15}Te_{85}$ and $Ge_2Sb_2Te_5$ films are 265nm, 301 nm and 310 nm, respectively. The solid lines describe the experimental data, whereas the dotted lines represent the simulation results. The superposition of the reflected waves results in interference fringes.*

The real part and the imaginary part of the dielectric functions of amorphous GeSe, $Ge_{15}Te_{85}$ and $Ge_2Sb_2Te_5$ between 0.05 eV and 1 eV derived from their reflectance spectra are displayed in figure 7.2 and figure 7.3, respectively. The optical dielectric constants (ε_∞), i.e. ε_1 at the energy of 0.05 eV, of amorphous GeSe, $Ge_{15}Te_{85}$ and $Ge_2Sb_2Te_5$ are determined to be 8.5, 12.3 and 16.2, respectively. The fact that ε_∞ of $Ge_{15}Te_{85}$ is smaller than that of $Ge_2Sb_2Te_5$, is in line with the speculation in the above. The ε_∞ of amorphous $Ge_2Sb_2Te_5$ is 16.2, which is very close to 16.6, the value reported in [Krem09]. Hence, it is safe to draw conclusion that the FT-IR reflectance spectra of the three materials are correctly interpreted. And the ε_∞ of amorphous GeSe, $Ge_{15}Te_{85}$ are useful for comparison with the ε_∞ obtained by the FT-FIR transmission in the next section.

Moreover, the imaginary part of all the dielectric function below 0.6 eV is zero because their bandgaps are larger than that. The bandgap of GeSe is even larger than the upper limit of the measurement range.

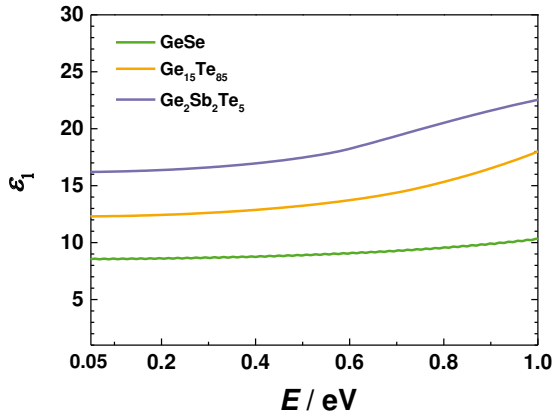

Figure 7.2 ***The dispersion of the real part of the dielectric functions of amorphous GeSe, $Ge_{15}Te_{85}$ and $Ge_2Sb_2Te_5$ from 0.05 eV to 1 eV****. The intercepts at the left Y axis of the three curves are 8.5, 12.3 and 16.2, respectively, which correspond to the optical dielectric constants.*

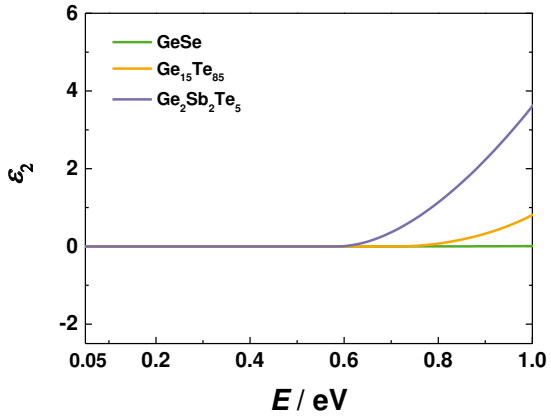

Figure 7.3 ***The dispersion of the imaginary part of the dielectric functions of amorphous GeSe, $Ge_{15}Te_{85}$ and $Ge_2Sb_2Te_5$ from 0.05 eV to 1 eV.*** *Below 0.6 eV, all ε_2 are zero. The upturn point of ε_2 appears firstly for amorphous $Ge_2Sb_2Te_5$ because of its smallest bandgap among the three materials.*

7.2 Far-infrared Transmission Measurement

As the lowest frequency of the transmission measurements was 20 cm^{-1} (i.e. 0.0025 eV), the data obtained from this analysis of the transmission measurements below this threshold frequency are to be considered as extrapolations.

7.2.1 Amorphous State

7.2.1.1 PCMs

Five amorphous PCMs were investigated by the FT-FIR transmission measurement in a wide frequency range from 20 cm^{-1} to 12000 cm^{-1} (i.e. 0.0025 eV to 1.5 eV, 0.6 THz to 360 THz). The transmission spectra of amorphous PCMs are shown in figure 7.4. At frequencies above the optical bandgap, which varies between 0.87 eV in $Ge_8Sb_2Te_{11}$ and 0.78 eV in $Ge_1Sb_2Te_4$, the films are opaque. Below the bandgap, the transmission is periodically modulated due to the Fabry-Pérot interference fringes in the film. As mentioned in the previous section, the difference

in spacing between the fringes depends on the product of the film thickness and the refractive index.

The close-up view of the far-infrared transmission spectra are depicted between 0.0025 eV and 0.12 eV in the right part of figure 7.4. These measurements allow for identifying the IR-active phonons and can, thus, shed more light on the origin of the stoichiometry trend in the pseudo-binary GeTe-Sb_2Te_3 system. As can be seen in the close-up view, absorption originating from IR-active phonons becomes discernible below 0.05 eV. Those phonons are clear to be observed but not well separated. There is a claim that the phonon shift when the Sb_2Te_3 increases could be partially attributed to the mass change. This could be verified by comparing the phonon shift with the square-root of the mass change.

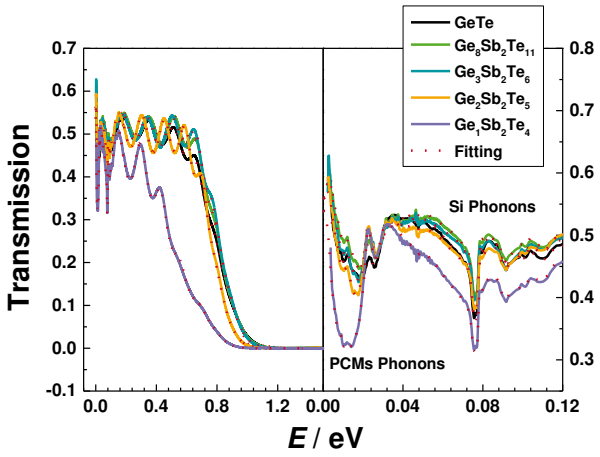

Figure 7.4 (Left) ***Transmission spectra of the amorphous PCMs listed in the legend on the high-resistivity silicon substrates from 0.0025 eV to 1.5 eV;*** *(Right)* ***A close-up view of the spectra between 0.0025 eV and 0.12 eV.*** *The thickness of samples from GeTe to $Ge_1Sb_2Te_4$ are 944 nm, 887 nm, 939 nm, 1002 nm and 932 nm, respectively. Fabry Perot interference fringes are observed below their bandgaps. The absorption is due to significant lattice absorption. Those infrared phonons in amorphous compounds are not well separated. The solid lines describe the experimental data, whereas the dotted lines represent the simulation results.*

The Kramers-Kronig-relations consistent analysis from the transmission spectra mentioned in section 3.4.2 yields the dielectric functions presented in figure 7.5 and figure 7.6. Indeed, the pronounced absorption features discernible in the imaginary parts $\varepsilon_2(\omega)$ below 0.03 eV can

unequivocally be attributed to IR-active phonons. A closer inspection with respect to the stoichiometry trend leads to the following three observations:

Firstly, the absorption spectrum of GeTe appears to be better defined (sharper) than those of the Sb_2Te_3-containing compositions in figure 7.6. The reason for this effect may be that GeTe – as a truly binary alloy – features less disorder than the ternary compounds. Secondly, on increasing the Sb_2Te_3 content, the modes clearly shift to lower frequencies. This effect can be partly attributed to the increase of the reduced mass for Sb-Te vibrations as compared to Ge-Te vibrations. Yet, it is very likely that an additional contribution comes from a weaker bonding in the Sb-rich compounds. Thirdly, the spectral weight of phonons increases continuously from GeTe to $Ge_1Sb_2Te_4$. As it is explained in the following, this means that the increase in ε_{st} is not just a mere consequence of the phonon softening due to the larger mass of the material constituents.

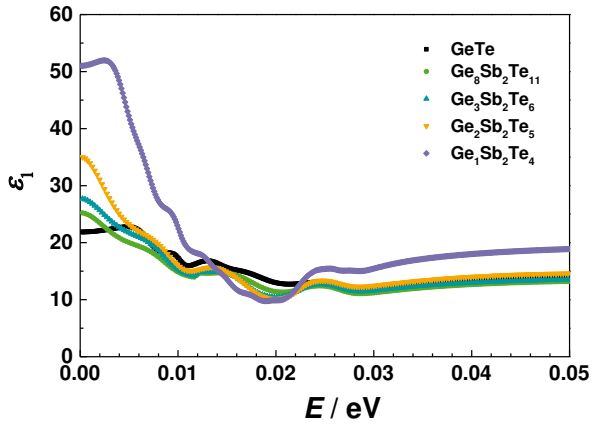

Figure 7.5 ***The dispersion of the real part of the dielectric functions of amorphous PCMs listed in the legend from 0 to 0.05 eV.*** *The data below 0.0025 eV are extrapolations. The extrapolation of the real part of the dielectric function down to zero-frequency reproduces the stoichiometry trend in ε_{st}, i.e. 22.2, 25.3, 27.8, 35.0, 52.0 from GeTe to $Ge_1Sb_2Te_4$.*

The spectral weight of phonons can be obtained by integrating the optical conductivity σ_1 as:

$$SWP = \int d\omega \cdot \sigma_1(\omega) = \frac{\pi}{2} \varepsilon_{vac} \sum_k \Delta\varepsilon_k \Omega_k^2 \tag{7.1}$$

where all non-phononic contribution have been subtracted from σ_1. For phonons that can be described by harmonic Lorentz oscillators, this integral is equivalent to the expression at the right hand side of equation 7.1. There, $\Delta\varepsilon_k$ is the phonon contribution to the dielectric constant and Ω_k is its resonance frequency [CLS+14]. The optical conductivity is related to the dielectric function by $\sigma_1 = \omega\varepsilon_2$. Of course, conservation of phonon spectral weight implies that a reduction of the phonon frequencies induces an increase in the value of $\Delta\varepsilon = \varepsilon_0 - \varepsilon_\infty$, and hence an increase of ε_0. However, the fact that a systematic increase is observed in the spectral weight of phonons, indicates that, in addition to the softening of the phonon frequencies, an enlargement of the dipole moment accounts for the larger values of ε_0. Hence, on increasing the Sb content, also the Born effective charge gets larger.

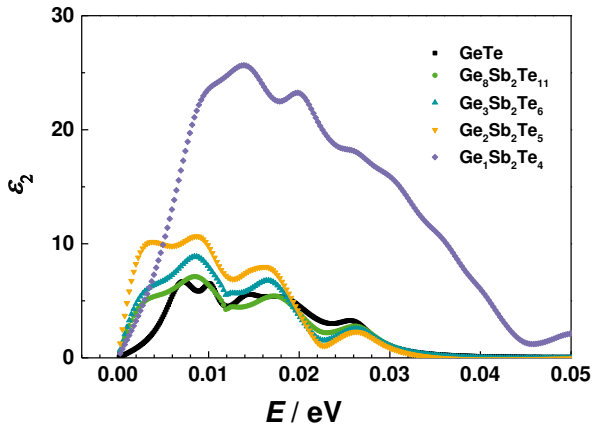

Figure 7.6 ***The dispersion of the imaginary part of the dielectric functions of amorphous PCMs from 0.0025 eV to 0.05 eV.*** *The data below 0.0025 eV are extrapolations. Pronounced phonon absorption is discernible in the range. Adding Sb_2Te_3 in the GeTe-Sb_2Te_3 system induces a reduction of the phonon frequencies and an increase of the spectral weight of phonons. The phonon softening from GeTe to $Ge_1Sb_2Te_4$ is attributed to the mass difference between Ge and Sb.*

In addition, a comparison between the static dielectric constant ε_0 derived from impedance spectroscopy and the optical dielectric constant ε_∞ determined by mid-infrared FT-IR is tempting. The static dielectric constants determined by impedance spectroscopy and FT-FIR

transmission spectra and the optical dielectric constants obtained from FT-FIR and FT-IR spectra are compiled and plotted in figure 7.7. All results are consistent with each other. As discussed before, $\varepsilon_0 > \varepsilon_\infty$ points at the presence of IR-active phonons. Indeed, for the pseudo-binary GeTe-Sb_2Te_3 systems, the impedance spectroscopy-based values of ε_0 ranging from 24.4 to 47.0 clearly exceed the FT-IR-based values of ε_∞, which are always close to 15 in these compositions [Krem09]. Thus, in contrast to literature data, where $\varepsilon_0 \sim 16$ was reported for $Ge_2Sb_2Te_5$ [PGL+13], the evidence of significant IR-active phonons in *all* pseudo-binary PCMs were found by FT-FIR measurements.

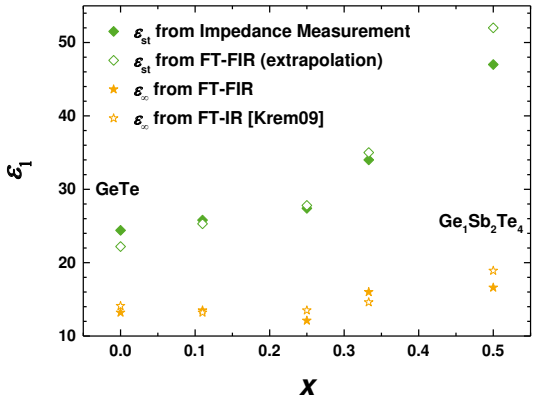

Figure 7.7 ***Comparison of the static and optical dielectric constants of amorphous $(GeTe)_{(1-x)}(Sb_2Te_3)_x$ alloys among different methods.*** *While ε_∞ depends only weakly on the stoichiometry, there is a marked surge in ε_{st} on increasing the Sb_2Te_3-content.*

Given the atomic masses of Ge, Sb, and Te, it is hard to imagine that phonons featuring frequencies below the lower limit of the measurement range (0.0025 eV) exist. Thus, employing the FT-FIR data to extrapolate the dielectric function down to zero frequency is worthwhile. The good agreement between the static dielectric constant obtained from impedance spectroscopy and the FT-FIR-based extrapolation of the static dielectric constant indicates that all significant optical excitations could be detected by FT-FIR.

As the amorphous $Ge_1Sb_4Te_7$ sample is sputtered with a cooling system, the similar data of the FT-FIR spectra and the dielectric function are not discussed together with other PCMs but separately presented in the appendix C.

7.2.1.2 Non-PCMs

Far-infrared transmission spectra of amorphous GeSe and $Ge_{15}Te_{85}$ between 0.0025 eV and 1.5 eV are illustrated in figure 7.8. The bandgap of amorphous GeSe is larger than 1.1eV. It is essentially transparent in the all mid-IR region, hence the interference fringes of amorphous GeSe have a roughly constant amplitude.

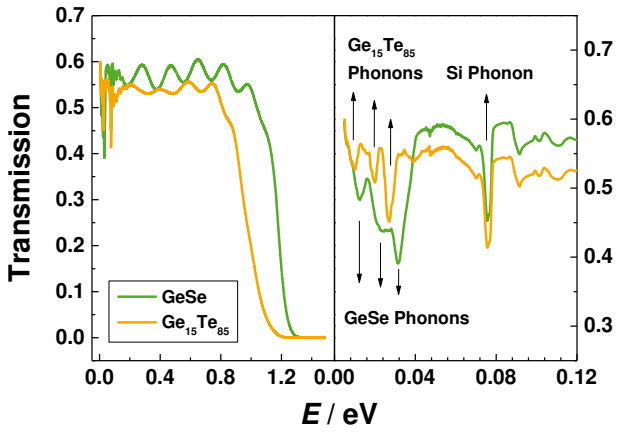

Figure 7.8 ***Transmission spectra of amorphous GeSe and $Ge_{15}Te_{85}$ thin films*** *on the high-resistivity silicon substrates are plotted from from 0.0025 eV to 1.5 eV. The thickness of GeSe and $Ge_{15}Te_{85}$ are 1066 nm and 900 nm, respectively. The infrared phonons of amorphous $Ge_{15}Te_{85}$ have sharper peaks than that of amorphous GeSe.*

Through data analysis of the transmission spectra the real part of the dielectric functions of GeSe and $Ge_{15}Te_{85}$ are presented in figure 7.9, from which the optical dielectric constants of amorphous GeSe and $Ge_{15}Te_{85}$ are estimated to be 8.9 and 11.7, respectively. Those values are very close to the values of GeSe (8.5) and $Ge_{15}Te_{85}$ (12.3) that obtained from the FT-IR reflectance measurement in section 7.1. Hence, the transmission spectra are correctly interpreted. Moreover, the static dielectric constants ε_{st} of amorphous ordinary chalcogenides,

such as GeSe and $Ge_{15}Te_{85}$, are 15.1 and 15.6, respectively, which are much smaller than that of amorphous PCMs along the GeTe-Sb_2Te_3 pseudo-binary line. It can be seen clearly from figure 7.9 that the spectral weight of phonons in GeSe is higher than that in $Ge_{15}Te_{85}$, which contributes to a larger gap ($\Delta\varepsilon$) between the static dielectric constant and optical dielectric constant of GeSe than that of $Ge_{15}Te_{85}$.

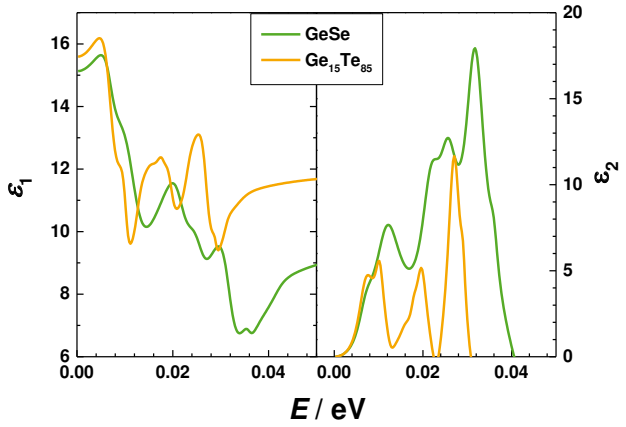

Figure 7.9 ***The dispersion of the real part (left) and the imaginary part (right) of the dielectric functions of amorphous GeSe and $Ge_{15}Te_{85}$ from 0 to 0.05 eV.*** *The lattice absorption in amorphous GeSe is higher than that in amorphous $Ge_{15}Te_{85}$, possibly due to the selection rules.*

7.2.2 Amorphous State vs. Crystalline State

7.2.2.1 $Ge_1Sb_2Te_4$

The as-deposited $Ge_1Sb_2Te_4$ thin film was amorphous and it crystallized after annealing at 155 °C for 30 minutes in the annealing furnace. Both the as-deposited sample and the annealed sample were investigated by the FT-FIR. The far-infrared transmission spectrum of the crystalline $Ge_1Sb_2Te_4$ is plotted in figure 7.10 with comparison to the spectra of the amorphous $Ge_1Sb_2Te_4$ already mentioned in section 7.2.1.1. The experimental data is in line with the fitting data. The interference fringes of the crystalline state shift to lower energy comparing to the amorphous state because of the smaller bandgap in crystalline $Ge_1Sb_2Te_4$.

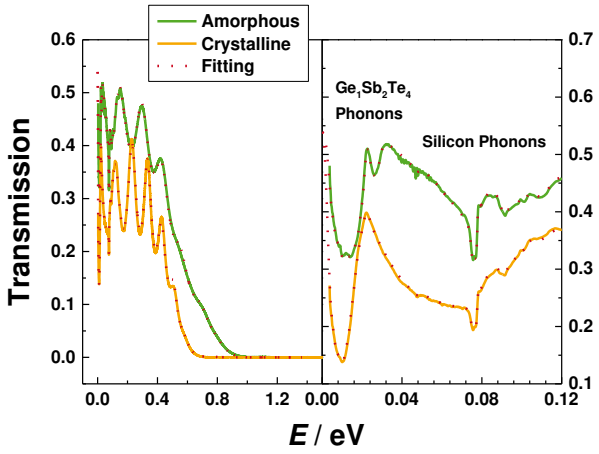

Figure 7.10 ***Transmission spectra of $Ge_1Sb_2Te_4$ thin films in both amorphous and crystalline states on the high-resistivity silicon substrates.*** *The thickness of the amorphous sample decreases from 932 nm to 905 nm upon crystallization. The solid lines describe the experimental data, whereas the dotted lines represent the simulation results.*

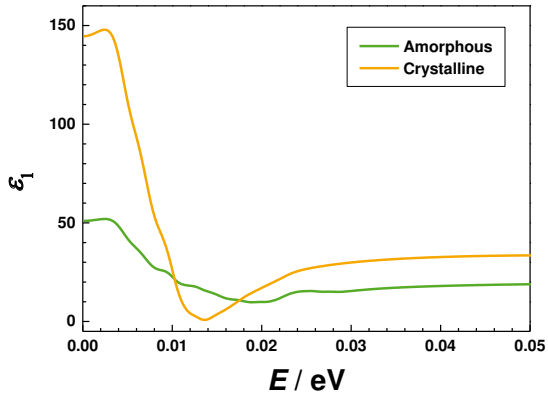

Figure 7.11 ***The dispersion of the real part of the dielectric functions of both amorphous and crystalline $Ge_1Sb_2Te_4$ from 0 to 0.05 eV.*** *There is a significant difference between the static dielectric constant and the optical dielectric constant for both amorphous and crystalline states of $Ge_1Sb_2Te_4$.*

The real part of the dielectric functions of $Ge_1Sb_2Te_4$ in amorphous and crystalline states are derived from the transmission spectra and plotted in figure 7.11. The intercept in the left Y-axis, i.e. the static dielectric constant of $Ge_1Sb_2Te_4$, increases from 52 in amorphous to 147.9 (this

value is not that accurate because of the screening effect of very high carrier concentrations) in crystalline.

In addition, the imaginary part of the dielectric functions of $Ge_1Sb_2Te_4$ in amorphous and crystalline states are presented in figure 7.12. The peaks of lattice absorption in crystalline $Ge_1Sb_2Te_4$ is much sharper and higher than that in the amorphous $Ge_1Sb_2Te_4$. Although the shift of phonon frequencies is not obvious in figure 7.12, the spectral weight of phonons in crystalline $Ge_1Sb_2Te_4$ is much larger than that in its amorphous state. According to equation (7.1), the increase of the spectral weight of phonons indicates an enlargement of the dipole moment accounts for the larger values of ε_0. Hence, the Born effective charge of amorphous $Ge_1Sb_2Te_4$ increases a lot after crystallization.

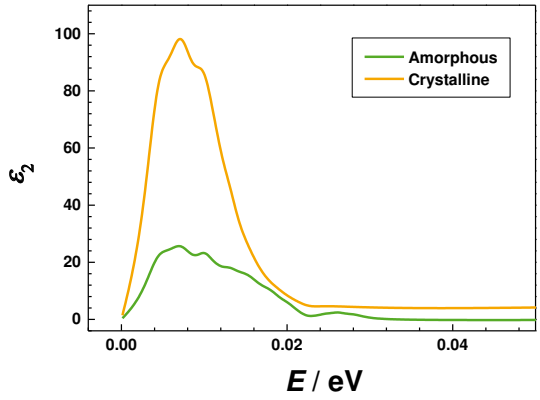

Figure 7.12 ***The dispersion of the imaginary part of the dielectric functions of amorphous and crystalline $Ge_1Sb_2Te_4$ from 0.0025 eV to 0.05 eV.*** *The phonon contribution in the crystalline state is much stronger than that in the amorphous state.*

The derivation of the Born effective charge is mentioned is section 2.3. The determination of Born effective charges using equations (2.27) and (2.28) is possible, if the investigated material is considered as isotropic, so that the dielectric functions is a scalar quantity, with just two different atoms, such as GeTe. For amorphous GeTe, a Born effective charge of around +2 (Ge) and -2 (Te), respectively, is obtained. This number is in good agreement with DFT calculations, which determine the Born effective charge to values of approximately 2 [RZL+15]. Interesting

enough, crystalline GeTe has been calculated to have an average Born effective charge of 4.6 [LSG+08, WSK+03], which depends strongly on atomic arrangement. Hence crystallization leads to a significant increase in the Born effective charge. Since the Born effective charge, as already mentioned above, is a bond indicator, this implies that crystallization of GeTe, as well as the other phase-change materials studied here, has a pronounced effect on the bonding mechanism utilized in this material. We are not aware of any other material class, which shows such a pronounced change of bonding upon crystallization. This phenomenon has recently also been confirmed for $Ge_2Sb_2Te_5$ [MSS+16], where the increase in the Born effective charge upon crystallization is explained by an ionic bonding contribution. Thus, the increase of the Born effective charge upon crystallization seems to be a generic property of phase-change materials. Yet, explaining this finding by an ionic bond contribution is not obvious [MSS+16], given the fact that in GeTe the difference in electronegativity is very small, since Ge (2.01) and Te (2.1) [Gray65] have almost identical values. This is quite different from the scenario encountered in clearly ionic compounds such as $PbTiO_3$ (Pb 2.33, Ti 1.54, O 3.44) [Gray65].

7.2.2.2 $AgInTe_2$

The as-deposited $AgInTe_2$ thin film was amorphous and it crystallized after annealing at 220 $^{\circ}$C for 30 minutes in the annealing furnace. Both the as-deposited sample and the annealed sample were studied by the FT-FIR spectra. The thickness of the as-deposited film was 691 nm, which decreased to 652 nm after crystallization. The structure and phases in the as-deposited and annealed films were investigated by the X-ray diffraction (XRD) measurements. The XRD spectra are shown in figure 7.13.

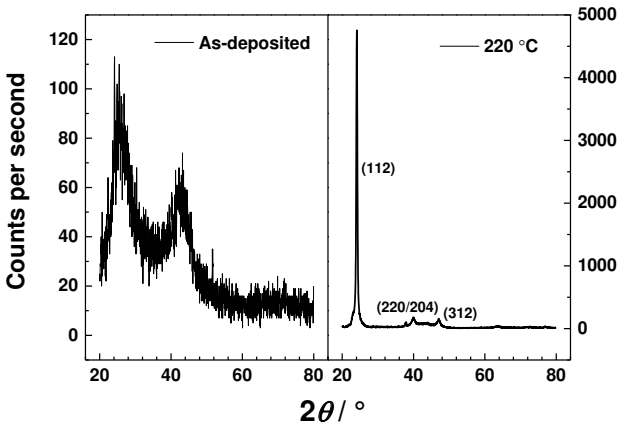

Figure 7.13 ***XRD measurements identify the structure and phases in the $AgInTe_2$ thin film on the silicon substrate.*** *(Left) amorphous state, (right) crystalline state. The indexed peaks result from the four-fold-coordinated chalcopyrite structure [IVK+99]. The diffraction pattern shows a preferred (112)-orientation parallel to the surface of the silicon substrate.*

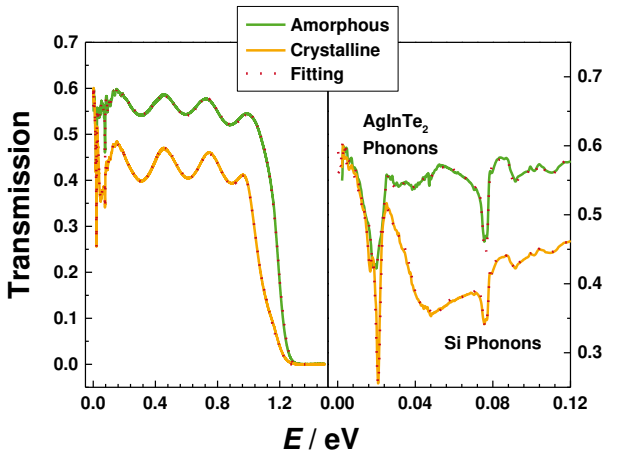

Figure 7.14 ***Infrared transmission spectra of amorphous and crystalline $AgInTe_2$ from 0.0025 eV to 1.5 eV.*** *A close-up view of the spectra below 0.12 eV is presented in the right part of the figure. The solid lines describe the experimental data, whereas the red dotted lines represent the simulation results.*

The comparison of transmission spectra between the amorphous and crystalline $AgInTe_2$ thin films is illustrated in figure 7.14. There is nearly no shift of the interference fringes and no difference in spacing of the reflectance minima between the amorphous and crystalline phases.

Hence, their optical bandgap and refractive index are supposed to be similar. Actually, the bandgap of amorphous and crystalline $AgInTe_2$ are reported in [Krem09] as 1.36 and 1.39, respectively. However, the transmission maxima is much lower for the crystalline $AgInTe_2$ than that for the amorphous state because of free carriers absorption in the crystalline state.

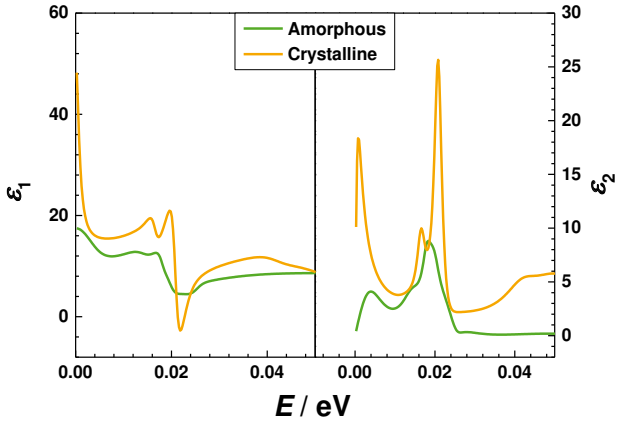

Figure 7.15 ***The dispersion of the real part and the imaginary part of the dielectric functions of $AgInTe_2$ in amorphous and crystalline below 0.05 eV.*** *The real part of the dielectric functions are extrapolated to zero. The infrared phonons are much stronger and better separated in crystalline state than that in amorphous state.*

The dielectric functions of both amorphous and crystalline $AgInTe_2$ derived from the transmission spectra are plotted in figure 7.15 from 0 to 0.05 eV. The static dielectric constant of amorphous $AgInTe_2$ thin film increases from 17.5 to 48 after crystallization, while the optical dielectric constant stays nearly the same for both the amorphous and crystalline states. The static dielectric constant increases in the crystalline $AgInTe_2$ because the phonon contribution is increased in the ordered structure. Phonons absorption is observed to be much stronger in the crystalline state than that in the amorphous state. The optical dielectric constants of both amorphous and crystalline $AgInTe_2$ are consistent with values reported in [Krem09]. There is no difference between the ε_∞ of crystalline and amorphous $AgInTe_2$ because both of them are governed by the same covalent bonding. It was reported in [MVJ13, SGZ95] that all of the $5s^2 5p^1$ valence electrons of indium in $AgInTe_2$ participate in forming sp^3 hybridized bonds with tellurium.

7.3 Conclusions

The FT-FIR transmission spectra of five PCMs and three non-PCMs are analyzed and compared with the results of FT-IR reflectance spectra. It independently corroborates the values of the static dielectric constant and unambiguously attributes the difference between the static dielectric constant and the optical dielectric constant to IR-active phonons in the region between 0.0025 eV and 0.05 eV. The FT-FIR spectra of amorphous PCMs along the pseudo-binary line reveal a shift to lower phonon frequencies on increasing the Sb_2Te_3 content. In addition, the increasing spectral weight of phonons indicates that the strength of the phonons is enlarged at the same time. Hence, the gap between the static dielectric constant and the optical dielectric constant, i.e. $\Delta\varepsilon$, increases, but the optical dielectric constant changes very slightly from GeTe to $Ge_1Sb_2Te_4$. Consequently, the static dielectric constant of amorphous PCMs climbs up with increasing the Sb_2Te_3 content.

As for non-PCMs, $\Delta\varepsilon$ of amorphous GeSe is larger than that of amorphous $Ge_{15}Te_{85}$, because of larger spectral weight of phonons in amorphous GeSe. In addition, there is nearly no difference between the optical dielectric constants determined by FT-FIR and FT-IR spectra, which hints both methods are valid.

As was reported by Shportko et al. [SKW+08, CJV+17], the presence of resonant bonding in crystalline PCMs leads to a doubling of the optical dielectric constant on crystallization. However, the optical dielectric constants of ordinary chalcogenide, such as $AgInTe_2$, does not change from the amorphous state to the crystalline state, because both states are governed by sp^3 covalent bonding. The experimental evidence is presented in this chapter that both the born effective charge and the static dielectric constant of amorphous PCMs change significantly upon crystallization. It is noteworthy that static dielectric constant of amorphous non-PCMs, such as $AgInTe_2$, also rises a lot after crystallization. Therefore, phonons are strengthened obviously from the amorphous to the crystalline for both PCMs and non-PCMs.

The comparison between the static dielectric constants and optical dielectric constants of amorphous chalcogenides including PCMs and non-PCMs is presented in table 7.1, and the

comparison of the dielectric constants between the amorphous and crystalline states is given in table 7.2.

Table 7.1 Summary of the FT-IR and FT-FIR measurements on amorphous PCMs along the GeTe-Sb_2Te_3 pseudo-binary line and amorphous non-PCMs. The static dielectric constant ε_{st} from FT-FIR, the optical dielectric constant ε_∞ from both FT-FIR and FT-IR, the spectral weight of phonons (SWP), the Born effective charge (Z^*) and the bandgap of those amorphous chalcogenides are listed for comparison. ([1] Taken from [Krem09])

Mass Ratio GeTe / Sb_2Te_3		ε_{st} **FT-FIR**	ε_∞ **FT-FIR**	**SWP** S / cm^2	Z^*	ε_∞ **FT-IR**	E_g
1	**0**	22.2	14.1	2235	2.08	13.2[1]	0.78[1]
0.89	**0.11**	25.3	13.2	1876		13.5[1]	0.81[1]
0.75	**0.25**	27.8	13.5	2059		12.1[1]	0.83[1]
0.67	**0.33**	35.0	14.6	2242		16.0[1]	0.77[1]
0.5	**0.5**	52.0	18.9	4046		16.6[1]	0.76[1]
0.33	**0.67**	52.0	17.3			18.2[1]	0.74[1]
Non-PCMs							
GeSe		15.1	8.9	2397	1.78	8.5	
$Ge_{15}Te_{85}$		15.6	11.7	783	3.08	12.3	

Table 7.2 The static dielectric constant, optical dielectric constant, the spectral weight of phonons and the bandgap are compared between the amorphous and crystalline states for $AgInTe_2$ (PCMs) and $Ge_1Sb_2Te_4$ (non-PCMs). ([1] Taken from [Krem09])

Materials	ε_{st} **FT-FIR**	ε_{∞} **FT-FIR**	**SWP S / cm^2**	ε_{∞} **FT-IR**	E_g **FT-IR**
a-$AgInTe_2$	17.5	8.6	1597	8.7[1]	1.36[1]
c-$AgInTe_2$	48.0	8.8	2826	8.8[1]	1.39[1]
a-$Ge_1Sb_2Te_4$	52.0	18.9	4046	16.2	0.76[1]
c-$Ge_1Sb_2Te_4$	147.9	33.5	10165	36.2[1]	0.39[1]

Conclusions and Outlook

8.1 Conclusions

This thesis presents a comprehensive study of dielectric properties of amorphous PCMs by AC electrical measurement, impedance spectroscopy and FT-FIR transmission. As the sandwich structures required for impedance spectroscopy measurements are prone to be affected by interface layers and as the results were in contradiction with existing literature data, AC electrical measurements and FT-FIR measurements were performed explicitly demonstrating the absence of such interface effects and other shortcomings in the samples. There are two aspects where this investigation goes beyond the scope of previous investigations: While previous investigations have studied the dielectric response in the THz range, this work investigated the entire frequency response from the DC limit to the near-infrared range. Furthermore, by comparing obtained results of different compounds, it is also able to study the stoichiometric dependence of dielectric properties and AC conductivities in amorphous GeTe-Sb_2Te_3 alloys. The experiments performed here, which investigate polarizability and phonon frequencies, come from a completely different direction as the advanced X-ray and neutron studies, but are sensitive to and therefore shed light on the very same properties: (local) atomic arrangement and bonding in the amorphous network. In that, this data can be regarded as complementary to these studies.

An increase in the static dielectric constant of amorphous PCMs is observed with increasing the content of Sb_2Te_3. The dielectric functions of all glasses studied in this work show no dispersion in radio frequencies, also the AC conductivity is frequency independent. In addition, the increase of ε_∞ in amorphous PCMs with temperature is due to the shrinkage of the bandgap, while the increase of ε_0 in amorphous PCMs with temperature is attributed to the enhancement of the intensity of infrared phonons. Furthermore, both the ε_0 and ε_∞ of PCMs increase on crystallization, which characterizes the change in bonding mechanism that accompanies crystallization. This is in contrast to non-PCMs, such as $AgInTe_2$, its ε_∞ stays the same upon crystallization, which unravels no changing in the bonding. However, the ε_0 of non-PCMs also increases because the phonon contribution is enhanced in ordered structures.

The ε_0 obtained by three different methods and ε_∞ by two different methods are compiled and compared in table 8.1. If one of the three methods had been compromised by shortcomings, it would be highly unlikely that both techniques independently produce the same results. Thus, the good agreement substantiates the validity of three methods and corroborates the observation that, in contradiction to literature data, ε_0 clearly exceeds ε_∞. Moreover, it indicates that the FT-FIR frequency range was sufficiently broad to cover all major optical excitations below the interband transition, i.e. there are no significant optical excitations between the lowest FT-FIR frequency (20 cm^{-1}) and the DC limit. Consequently, the complete dielectric functions of amorphous PCMs between the DC limit and the first interband transition are obtained.

Table 8.1 Summary of AC electrical measurement, impedance spectroscopy, FT-FIR transmission and FT-IR reflectance results. The static dielectric constants ε_{st} and the optical dielectric constants ε_{∞} of five PCMs and three non-PCMs are listed. ([1] Taken from [Schl12]. [2] Taken from [Krem09].)

Methods **Materials**	**PPMS** ε_{st} *(4 K - 120 K)*	**VNA** ε_{st}	**FT-FIR** ε_{st}	**FT-FIR** ε_{∞}	**FT-IR** ε_{∞}
a-$AgInTe_2$			17.5	8.6	8.7[2]
c-$AgInTe_2$			48.0	8.8	8.8[2]
a-GeSe	14.7–15.6		15.1	8.9	8.5
a-$Ge_{15}Te_{85}$	16.0–16.2	16.7[1]	15.6	11.7	12.3
a-GeTe	20.3–23.8	24.4	22.2	14.1	13.2[2]
a-$Ge_8Sb_2Te_{11}$	21.7–23.1	25.8	25.3	13.2	13.5[2]
a-$Ge_3Sb_2Te_6$	24.9–26.4	27.4	27.8	13.5	12.1[2]
a-$Ge_2Sb_2Te_5$	28.4–30.1	34.0	35.0	14.6	16.2
a-$Ge_1Sb_2Te_4$	35.5–39.0	47.0	52.0	18.9	16.6[2]
c-$Ge_1Sb_2Te_4$			147.9	33.5	36.2[2]
a-$Ge_1Sb_4Te_7$			52.0	17.3	18.2[2]

8.2 Outlook

PCMs have recently gained considerable attention for applications in nonvolatile memory such as random access memories. Multilevel resistive switching nonvolatile memory based on PCMs is promising for the fast switching speed, and low power consumption. In order to keep up with the demand for increased memory capacities, devices have been continuously scaled to smaller and smaller dimensions. The application of multilevel cells with the three-dimensional cross-point array architecture is able to further improve the storage density. The comprehensive study of dielectric properties of amorphous PCMs is very necessary.

The complete dielectric functions and the AC conductivities along with the frequency of amorphous PCMs are obtained between the DC limit and the first interband transition at room temperature. However, the measurement system was not calibrated at varied temperatures for the temperature dependent impedance measurement. The impedance measurement system was only calibrated at room temperature, instead of calibrating at each measurement temperature, as the access time of the cooling cryostat is limited. Therefore more experiments need to be further carried out.

1) To do the temperature dependent impedance measurement at low temperatures with the calibration process at each measurement temperature. To find out the transport mechanism in amorphous PCMs at low temperatures.

2) To do the temperature dependent FT-FIR measurement, which is expected to corroborate the temperature dependent impedance measurement.

3) To modify VNA samples by inserting an anti-diffusion layer between the PCM layer and the electrodes to avoid gold diffusion at elevated temperatures. Afterwards, to measure the aging effect of amorphous PCMs by impedance spectroscopy.

4) To find out the reason why VNA samples deteriorated after placing in the atmosphere for some time. This phenomenon is speculated to be caused by the interfacial change with time in VNA samples. To compare the interface of fresh VNA samples and aged VNA samples.

Appendix A

In appendix A, data analogous to those presented in Chapter 5.

A.1 GeSe

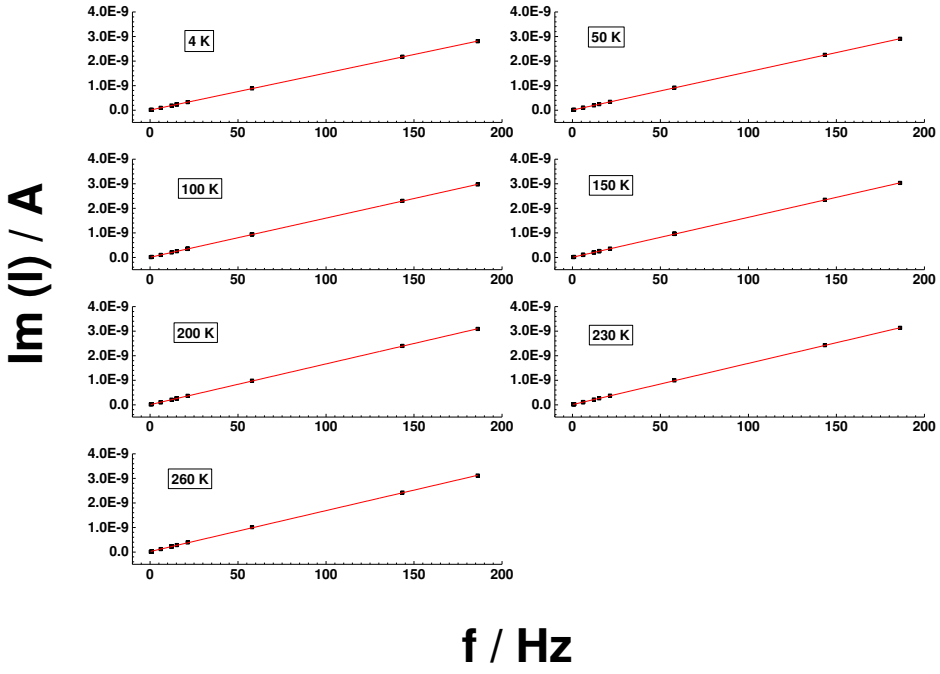

Figure A.1 ***AC electrical measurement on the amorphous GeSe sample at selected temperatures from 4 K to 260 K.*** *The X-axis of graphs presents the frequency and the Y-axis denotes the quadrature current. The measured data and fitting results are plotted in black dots and red lines, respectively.*

Table A.1 Capacitances and dielectric constants of amorphous GeSe at different temperatures measured by AC electrical measurements from 4 K to 260 K. The thickness of the amorphous $Ge_{15}Te_{85}$ is 540 nm and the capacitor area is 1 × 1 mm^2.

T / K	C / F	ε_{st}
4	2.40E-10	14.7
10	2.42E-10	14.8
20	2.44E-10	14.9
35	2.47E-10	15.0
50	2.49E-10	15.2
65	2.50E-10	15.3
80	2.52E-10	15.4
100	2.54E-10	15.5
120	2.56E-10	15.6
130	2.57E-10	15.7
150	2.59E-10	15.8
170	2.61E-10	16.0
200	2.65E-10	16.1
230	2.68E-10	16.3
260	2.66E-10	16.2

A.2 GeTe

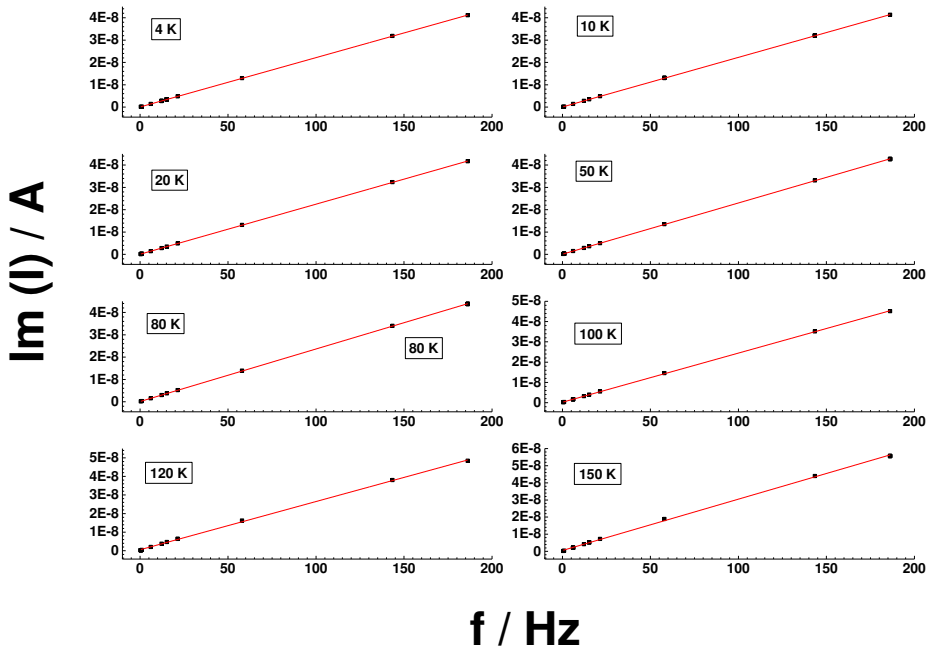

Figure A.2 ***AC electrical measurement on the amorphous GeTe sample with the classic gold electrode at selected temperatures from 4 K to 150 K.*** *The X- and Y-axis of graphs have the same label as in figure A.1. The measured and fitting data are shown in black dots and red lines, respectively.*

A.3 $Ge_8Sb_2Te_{11}$

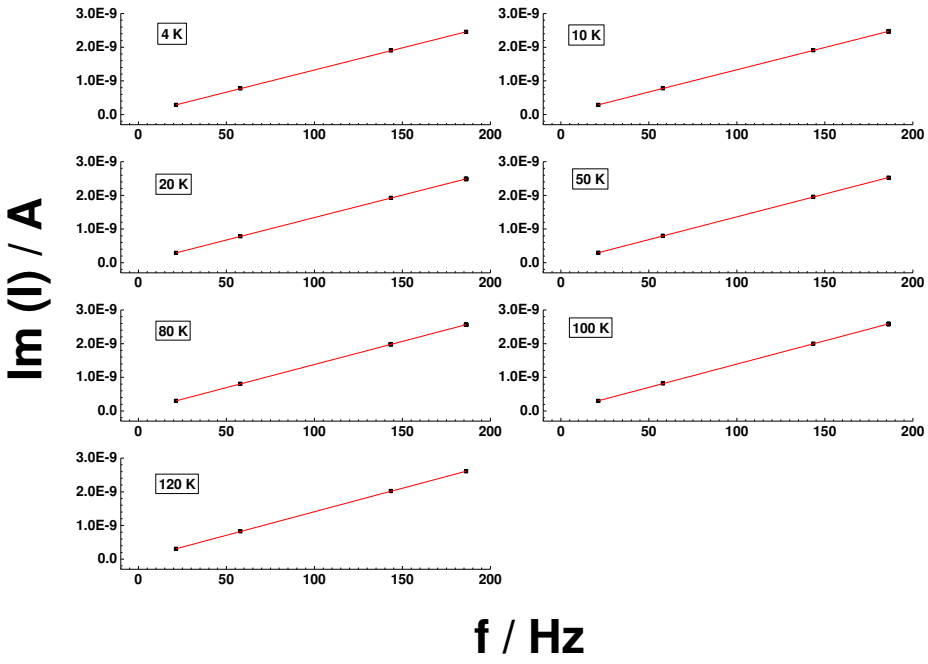

Figure A.3 ***AC electrical measurement on the amorphous $Ge_8Sb_2Te_{11}$ sample with classic gold electrode from 4 K to 120 K.*** *The X- and Y-axis of graphs have the same label as in figure A.1. The measured and fitting data are shown in black dots and red lines, respectively.*

Table A.3 Capacitances and static dielectric constants of amorphous $Ge_8Sb_2Te_{11}$ with the classic gold electrode from 4 K to 120 K. The thickness of the amorphous $Ge_8Sb_2Te_{11}$ thin film is 903 nm and the capacitor area is 1 × 1 mm^2.

***T* / K**	***C* / F**	**ε_{st}**
4	2.10E-10	21.7
10	2.11e-10	21.8
20	2.12e-10	22.0
35	2.14e-10	22.2
50	2.16e-10	22.3
65	2.17e-10	22.5
80	2.19e-10	22.6
100	2.20e-10	22.9
120	2.22e-10	23.1

A.4 $Ge_3Sb_2Te_6$

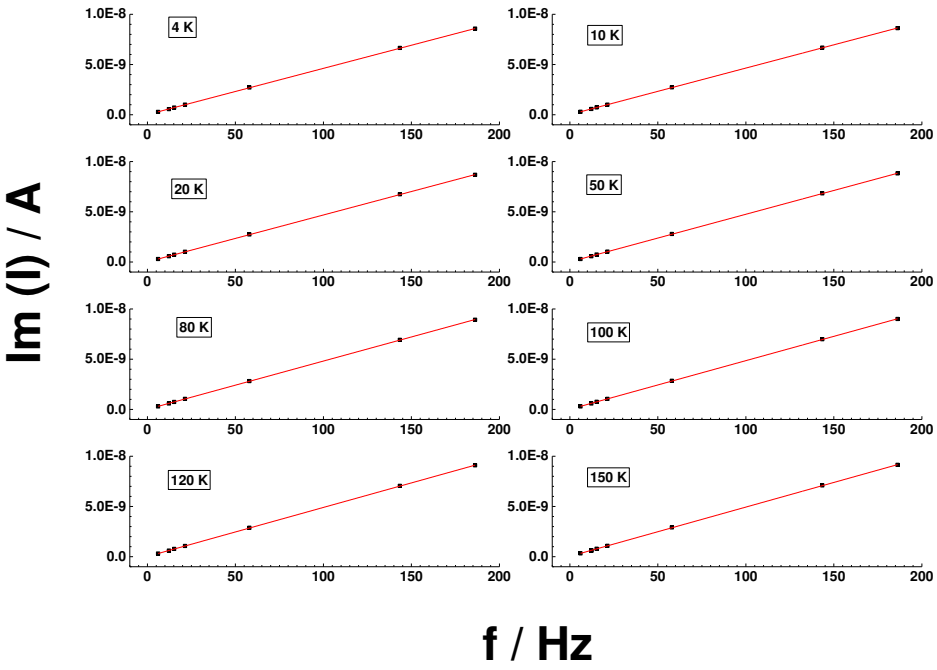

Figure A.4 ***AC electrical measurement on the amorphous $Ge_3Sb_2Te_6$ sample at selected temperatures from 4 K to 150 K.*** *The X- and Y-axis of graphs have the same label as in figure A.1. The measured and fitting data are shown in black dots and red lines, respectively.*

Table A.4 Capacitances and static dielectric constants of amorphous $Ge_3Sb_2Te_6$ with the classic gold electrode from 4 K to 150 K. The thickness of the amorphous $Ge_3Sb_2Te_6$ is 300 nm and the capacitor area is 1 × 1 mm^2.

T / K	C / F	ε_{st}
4	7.332E-10	24.85
10	7.377E-10	25.00
20	7.434E-10	25.20
35	7.495E-10	25.40
50	7.547E-10	25.58
65	7.560E-10	25.75
80	7.644E-10	25.91
100	7.707E-10	26.13
120	7.778E-10	26.37
150	7.812E-10	26.48

A.5 $Ge_2Sb_2Te_5$

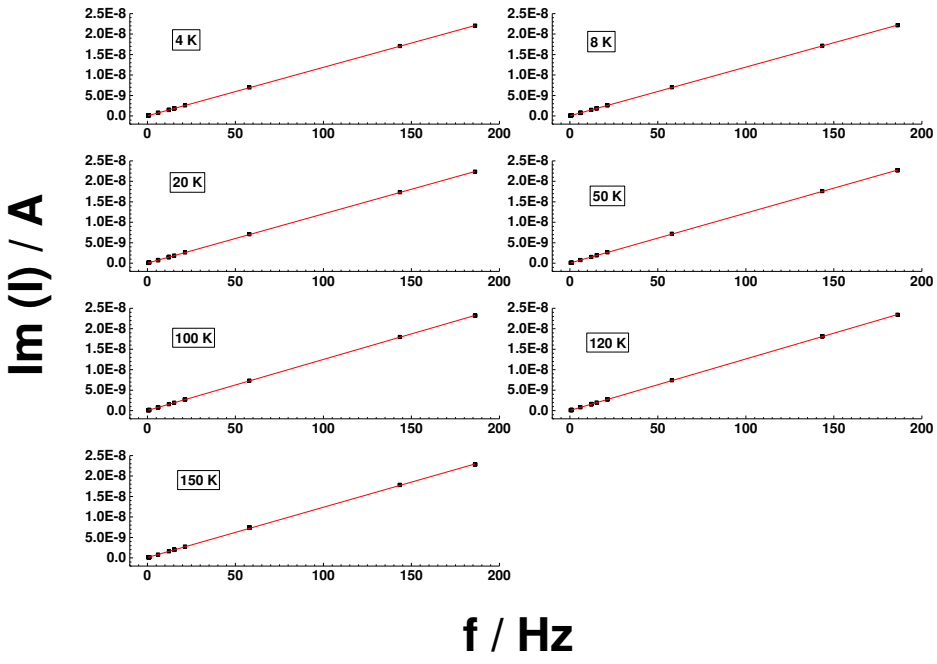

Figure A.5 ***AC electrical measurement on the amorphous $Ge_2Sb_2Te_5$ sample at selected temperatures from 4 K to 150 K****. The X- and Y-axis of graphs have the same label as in figure A.1. The measured and fitting data are shown in black dots and red lines, respectively.*

Table A.5 Capacitances and static dielectric constants of amorphous $Ge_2Sb_2Te_5$ with the classic gold electrode from 4 K to 150 K. The thickness of the amorphous $Ge_2Sb_2Te_5$ is 517 nm and the capacitor area is 2 × 2 mm^2.

T / K	C / F	ε_{st}
4	1.89E-9	28.4
8	1.90E-9	28.5
20	1.92E-9	28.8
50	1.94E-9	29.2
100	1.99E-9	29.9
120	2.00E-9	30.1
150	1.96E-9	29.4

A.6 $Ge_1Sb_2Te_4$

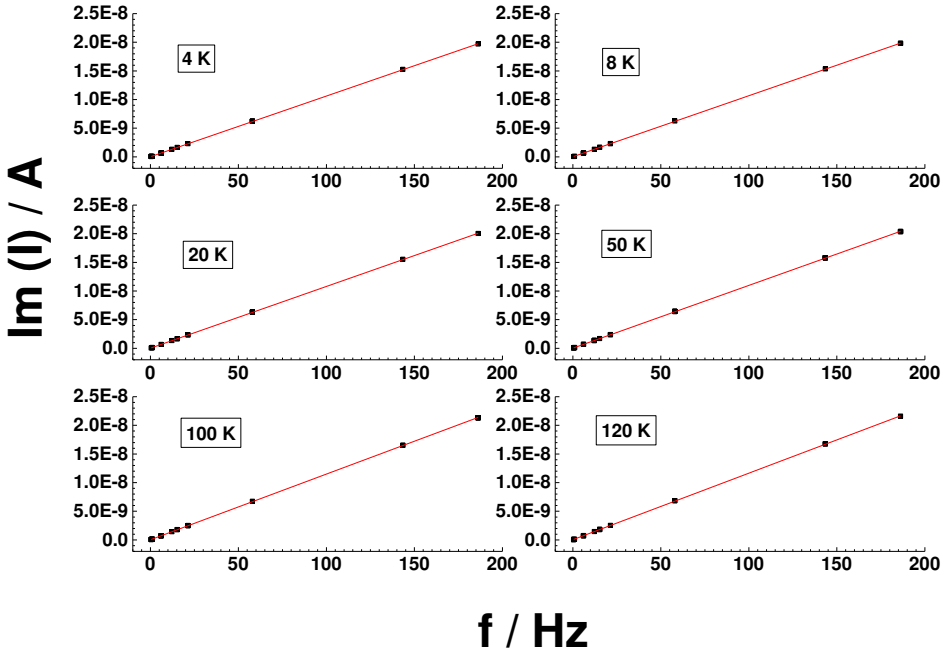

Figure A.6 ***AC electrical measurement on the amorphous $Ge_1Sb_2Te_4$ sample at selected temperatures from 4 K to 120 K****. The X- and Y-axis of graphs have the same label as in figure A.1. The measured and fitting data are shown in black dots and red lines, respectively.*

Table A.6 *Capacitances and static dielectric constants of amorphous $Ge_1Sb_2Te_4$ with the classic gold electrode from 4 K to 120 K. The thickness of the amorphous $Ge_1Sb_2Te_4$ is 746 nm and the capacitor area is 2 × 2 mm^2.*

T / K	C / F	ε_{st}
4	1.69E-9	35.5
8	1.70E-9	35.7
20	1.72E-9	36.2
50	1.75E-9	36.8
100	1.83e-9	38.5
120	1.85E-9	39.0

Appendix B

In appendix B, data analogous to those presented in Chapter 6. The temperature dependent impedance measurements were carried out on old samples, which have been placed in the atmosphere for several months. The AC conductivity at room temperature became frequency dependent above 10^7 Hz, which is quite similar to the result of samples with interfacial defects. This phenomena is more obvious in amorphous $Ge_2Sb_2Te_5$ and $Ge_1Sb_2Te_4$ samples because they are more conductive than other amorphous PCMs. The reason why those samples deteriorated with time need to be found out.

B.1 GeTe

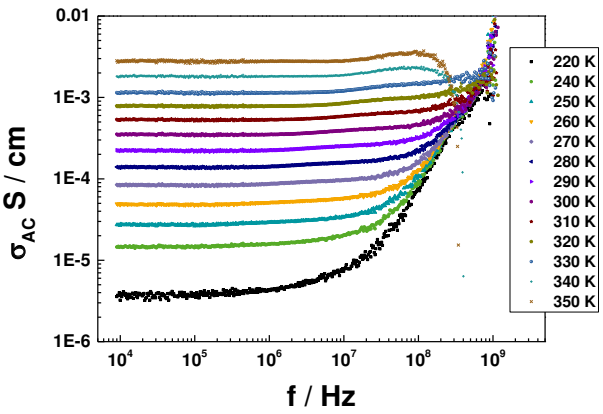

Figure B.1 ***The AC conductivity of amorphous GeTe measured by the impedance measurement from 220 K to 350 K.***

B.2 $Ge_8Sb_2Te_{11}$

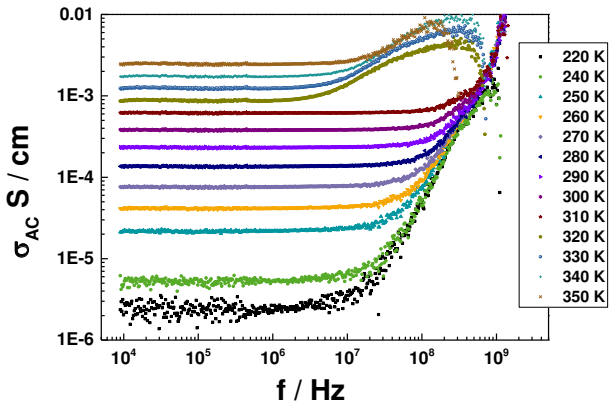

Figure B.2 ***The AC conductivity of amorphous $Ge_8Sb_2Te_{11}$ measured by the impedance measurement from 220 K to 350 K.***

B.3 $Ge_2Sb_2Te_5$

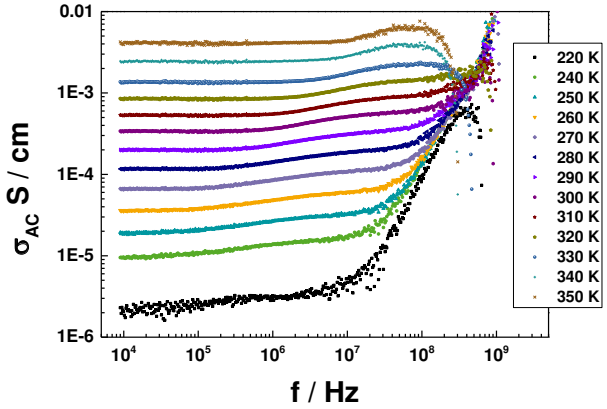

Figure B.3 ***The AC conductivity of amorphous $Ge_2Sb_2Te_5$ measured by the impedance measurement from 220 K to 350 K.***

B.4 $Ge_1Sb_2Te_4$

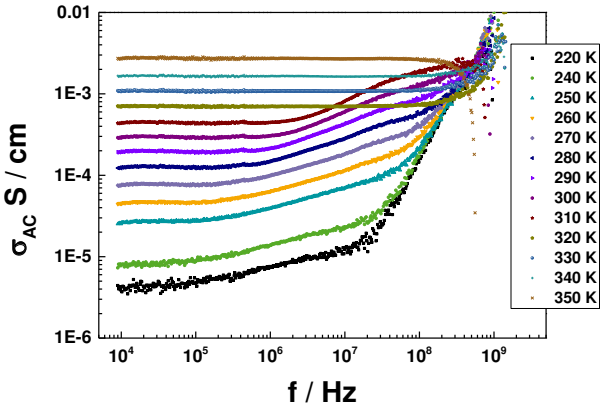

Figure B.4 ***The AC conductivity of amorphous $Ge_2Sb_2Te_4$ measured by the impedance measurement from 220 K to 350 K.***

Appendix C

In appendix C, data analogous to those presented in Chapter 7.

C.1 $Ge_1Sb_4Te_7$

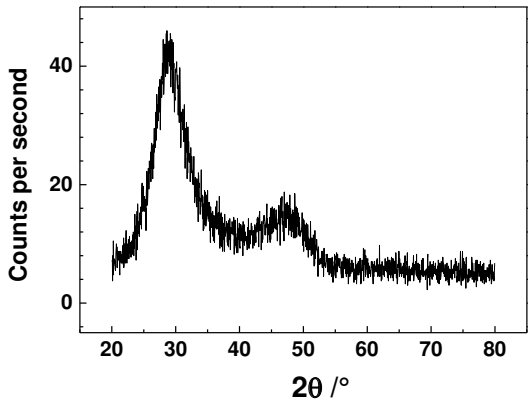

Figure C.1 ***XRD measurement identifies the structure and phases in the $Ge_1Sb_4Te_7$ thin film on the silicon substrate.*** *With the sputter chamber used in this work, as-deposited $Ge_1Sb_4Te_7$ thin film is partially crystalline. This amorphous sample was sputtered with the cooling system, without recording the exact temperature of the substrate during deposition.*

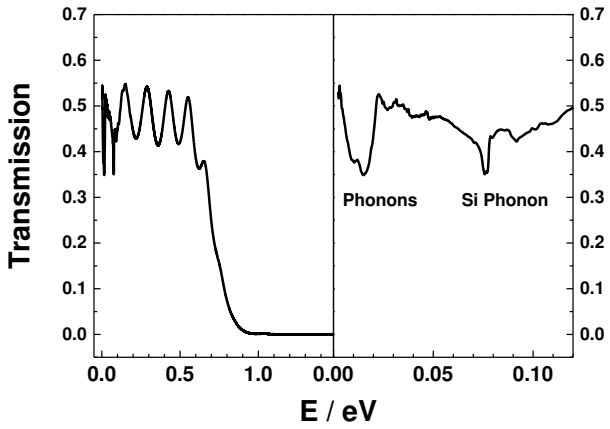

Figure C.2 ***The FT-FIR transmission spectrum of amorphous $Ge_1Sb_4Te_7$ thin film with the thickness of 939 nm from 0.0025 eV to 1.5 eV.***

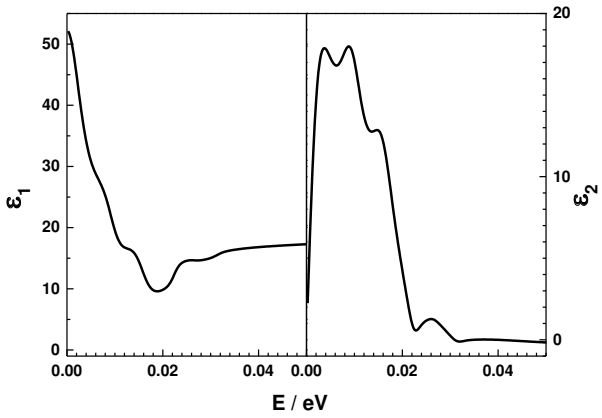

Figure C.3 ***The real part and the imaginary part of the dielectric function derived from the transmission spectra of amorphous $Ge_1Sb_4Te_7$ thin film are plotted from 0 to 0.05 eV.*** *Pronounced phonon absorption is discernible in this range.*

Bibliography

[Ovsh68] Ovshinsky S. R., Reversible Electrical Switching Phenomena in Disordered Structures, *Phys. Rev. Lett.* 21, 1450 (1968), cited on page 5, 8.

[WY07] Wuttig M. and Yamada N., Phase-change materials for rewriteable data storage, *Nat. Mater.* 6, 824 (2007), cited on page 1, 6, 8.

[BBF+10] Burr G. W., Breitwisch M. J., Franceschini M., Garetto D., Gopalakrishnan K., Jackson B., Kurdi B., Lam C., Lastras L. A., Padilla A., Rajendran B., Raoux S., Shenoy R. S., Phase change memory technology, *J. Vac. Sci. Technol. B.* 28, 223 (2010), cited on page 8.

[HOM+06] Hamann H. F., O'Boyle M., Martin Y. C., Rooks M., Wickramasinghe H. K., Ultra high-density phase-change storage and memory, *Nat. Mater.* 5, 383 (2006), cited on page 8.

[BMS+09] Bruns G., Merkelbach P., Schlockermann C., Salinga M., Wuttig M., Happ T. D., Philipp J. B., Kund M., Nanosecond switching in GeTe phase change memory cells, *Appl. Phys. Lett.* 95, 043108 (2009), cited on page 9.

[Hwa15] Hwang C. S., Prospective of Semiconductor Memory Devices: from Memory System to Materials, *Adv. Electron. Mater.* 1, 1400056 (2015), cited on page 9.

[LSG+08] Lencer D., Salinga M., Grabowski B., Hickel T., Neugebauer J., Wuttig M., A map for phase-change materials, *Nat. Mater.* 7, 972 (2008), cited on page 1, 9, 10, 134.

[SKW+08] Shportko K., Kremers S., Woda M., Lencer D., Robertson J., Wuttig M., Resonant bonding in crystalline phase-change materials, *Nat. Mater.* 7, 653 (2008), cited on page 2, 4, 9, 10, 28, 32, 55, 123, 138.

[SJV+11] Siegrist T., Jost P., Volker H., Woda M., Merkelbach P., Schlockermann C., and Wuttig M., Disorder-induced localization in crystalline phase-change materials, *Nat. Mater.* 10, 202 (2011), cited on page 1, 9, 11.

[ZTZ+12] Zhang W., Thiess A., Zalden P., Zeller R., Dederichs P. H., Raty J. Y., Wuttig M., Blugel S., Mazzarello R., Role of vacancies in metal–insulator transitions of crystalline phase-change materials, *Nat. Mater.* 11, 952 (2012), cited on page 9.

[HR10] Huang B., Robertson J., Bonding origin of optical contrast in phase-change memory materials, *Phys. Rev. B* 81, 081204 (2010), cited on page 9, 116.

[GCS+15] Gabardi S., Caravati S., Sosso G. C., Behler J., Bernasconi M., Microscopic origin of resistance drift in the amorphous state of the phase-change compound GeTe, *Phys. Rev. B* 92, 054201 (2015), cited on page 7, 9.

[Zach32] Zachariasen W. H., The atomic arrangement in glass, *J. Am. Chem. Soc.* 54, 3841 (1932), cited on page 4, 9.

[KFF+04] Kolobov A. V., Fons P., Frenkel A. I., Ankudinov A. L., Tominaga J., Uruga T., Understanding the phase-change mechanism of rewritable optical media, *Nat. Mater.* 3, 703 (2004), cited on page 9.

[JKS+08] Jóvári P., Kaban I., Steiner J., Beuneu B., Schöps A., Webb M. A., Local order in amorphous $Ge_2Sb_2Te_5$ and $GeSb_2Te_4$, *Phys. Rev. B* 77, 035202 (2008), cited on page 9.

[KKF+11] Krbal M., Kolobov A. V., Fons P., Tominaga J., Elliott S. R., Hegedus J., Uruga T., Selective detection of tetrahedral units in amorphous GeTe-based phase change alloys using Ge L3-edge x-ray absorption near-edge structure spectroscopy, *Phys. Rev. B* 83, 054203 (2011), cited on page 9, 113.

[MOI+16] Matsubara E., Okada S., Ichitsubo T., Kawaguchi T., Hirata A., Guan P. F., Tokuda K., Tanimura K., Matsunaga T., Chen M. W., Yamada N., Initial Atomic Motion Immediately Following Femtosecond-Laser Excitation in Phase-Change Materials, *Phys. Rev. Lett.* 117, 135501 (2016), cited on page 9.

[DZL+14] Deringer V. L., Zhang W., Lumeij M., Maintz S., Wuttig M., Mazzarello R., Dronskowski R., Bonding nature of local structural motifs in amorphous GeTe, *Angew. Chem. Int. Ed.* 53, 10817 (2014), cited on page 9.

[WW08] Wełnic W., Wuttig M., Reversible switching in phase-change materials, *Mater. Today* 11, 20 (2008), cited on page 9.

[KBJ+14] Krebs D., Bachmann T., Jonnalagadda P., Dellmann L., Raoux S., High-field electrical transport in amorphous phase-change materials, *New J. Phys.* 16, 043015 (2014), cited on page 9, 89.

[AJ07] Akola J., Jones R. O., Structural phase transitions on the nanoscale: The crucial pattern in the phase-change materials $Ge_2Sb_2Te_5$ and GeTe, *Phys. Rev.* B 76, 235201 (2007), cited on page 9.

[AJK+09] Akola J., Jones R. O., Kohara S., Kimura S., Kobayashi K., Takata M., Matsunaga T., Kojima R., Yamada N., Experimentally constrained density-functional calculations of the amorphous structure of the prototypical phase-change material $Ge_2Sb_2Te_5$, *Phy.s Rev. B* 80, 020201 (2009), cited on page 9, 10.

[HE08] Hegedus J., Elliott S. R., Microscopic origin of the fast crystallization ability of Ge–Sb–Te phase-change memory materials, *Nat. Mater.* 7, 399 (2008), cited on page 9, 10.

[CBK+09] Caravati S., Bernasconi M., Kühne T. D., Krack M., Parrinello M., Unravelling the Mechanism of Pressure Induced Amorphization of Phase Change Materials, *Phys. Rev. Lett.* 102, 205502 (2009), cited on page 9, 10.

[RBB+08] Raoux S., Burr G. W., Breitwisch M. J., Rettner C. T., Chen Y. C., Shelby R. M., Salinga M., Krebs D., Chen S. H., Lung H. L., Lam C. H., Phase-change random access memory: a scalable technology, *IBM J. Res. Dev.* 52, 465-480 (2008), cited on page 10, 11.

[LSW11] Lencer D., Salinga M., Wuttig M., Design Rules for Phase-Change Materials in Data Storage Applications, *Adv. Mater.* 23, 2030 (2011), cited on page 8.

[Emin76] Emin D., Linear and Nonlinear Electron Transport in Solids, edited by J. T. Devreese, V. E. V. Doren, *Springer US*, Vol. 17, p. 409 (1976), cited on page 10.

[ISL+09] Ielmini D., Sharma D., Lavizzari S., Lacaita A. L., Reliability impact of chalcogenide-structure relaxation in phase change memory (PCM) cells – Part I: Experimental study, *IEEE Trans. Electron Dev.* 56, 1070 (2009), cited on page 10.

[MGK89] Maan A. S., Goyal D. R., Kumar A., A.C. conductivity of amorphous Ga-Se-Te system, *Rev. Phys. Appl.* 24, 1071 (1989), cited on page 11.

[PGL+13] Prokhorov E., Gervacio-Arciniega J. J., Luna-Bárcenas G., Kovalenko Y., Espinoza-Beltrán F. J., Trápaga G., Dielectric properties of $Ge_2Sb_2Te_5$ phase-change films, *J. Appl. Phys.* 113, 113705 (2013), cited on page 10, 11, 61, 111, 129.

[SPH+10] Santos R. R., Prokhorov E., Hernández J. G., Bárcenas G. L., Kovalenko Y., Dielectric relaxation processes in stoichiometric Ge:Sb:Te amorphous films, *J. Non-Cryst. Solids* 356, 2541–2545 (2010) , cited on page 10, 11, 61.

[SMW12] Siegrist T., Merkelbach P., Wuttig M., Phase Change Materials: Challenges on the Path to a Universal Storage Device, *Annu. Rev. Condens. Matter Phys.* 3, 215–237 (2012), cited on page 1.

[Raou09] Raoux S., Phase Change Materials, *Annu. Rev. Mater. Res.* 39, 25–48 (2009), cited on page 1.

[Herp09] Herpers A., Eigenschaftstrends in Phasenwechselmaterialien bei Stöchiometrie-variation. *Diploma thesis*, RWTH Aachen University (2009), cited on page 1.

[LPB+13] Luckas J., Piarristeguy A., Bruns G., Jost P., Grothe S., Schmidt R. M., Longeaud C., Wuttig M., Stoichiometry dependence of resistance drift phenomena in amorphous GeSnTe phase-change alloys, *J. Appl. Phys.* 113, 023704 (2013), cited on page 1.

[MAI+88] Maeda Y., Andoh H., Ikuta I., Minemura H., Reversible phase ‐ change optical data storage in InSbTe alloy films, *J. Appl. Phys.* 64, 1715–1719 (1988), cited on page 1.

[FWN+00] Friedrich I., Weidenhof V., Njoroge W., Wuttig M., Structural transformations of Ge2Sb2Te5 films studied by electrical resistance measurements, *J. Appl. Phys.* 87, 4130 (2000), cited on page 1.

[YON+91] Yamada N., Ohno E., Nishiuchi K., Akahira N., Takao M., Rapid-phase transitions of GeTe-Sb2Te3 pseudobinary amorphous thin films for an optical disk memory, *J. Appl. Phys.* 69, 2849 (1991), cited on page 2.

[MKY+06] Matsunaga T., Kojima R., Yamada N., Kifune K., Kubota Y., Tabata Y., Takata M., Single Structure Widely Distributed in a GeTe–Sb2Te3 Pseudobinary System: A Rock Salt Structure is Retained by Intrinsically Containing an Enormous Number of Vacancies within its Crystal, *Inorg. Chem.* 45, 2235–2241 (2006), cited on page 3.

[Merk11] Merkelbach P. J., Crystalline Phase-Change Materials: Disorder, Medium-range Order and Electrical Switching, *Dissertation*, RWTH Aachen University, (2011), cited on page 3.

[IR60] Ioffe A. F., Regeli A. R., Non-crystalline, amorphous, and liquid electronic semiconductors, *Prog. Semicond.* 4, 237 (1960), cited on page 4.

[SCM+11] Sosso G. C., Caravati S., Mazzarello R., Bernasconi M., Raman spectra of cubic and amorphous $Ge_2Sb_2Te_5$ from first principles, *Phys. Rev. B* 83, 134201 (2011), cited on page 4, 113.

[MSS+16] Mukhopadhyay S., Sun J. F., Subedi A., Siegrist T., Singh D. J., Competing covalent and ionic bonding in Ge-Sb-Te phase change materials, *Sci. Rep.* 6, 25981 (2016), cited on page 4, 134.

[RZL+15] Raty J. Y., Zhang W., Luckas J., Chen C., Mazzarello R., Bichara C., Wuttig M., Aging mechanisms in amorphous phase-change materials, *Nat. Commun.* 6, 7467 (2015), cited on page 4, 7, 13, 88, 89, 91, 134.

[AHM78] Adler D., Henisch H. K., Mott S. N., The mechanism of threshold switching in amorphous alloys, *Rev. Mod. Phys.* 50, 209 (1978), cited on page 5.

[PLB+04] Pirovano A., Lacaita A. L., Benvenuti A., Pellizzer F., Bez R., Electronic switching in phase-change memories, *IEEE Trans. Electron Devices* 51, 452 (2004), cited on page 5.

[WS14] Wimmer M., Salinga M., The gradual nature of threshold switching, *New J. Phys.* 16, 113044 (2014), cited on page 5.

[Emin06] Emin D., Current-driven threshold switching of a small polaron semicon-ductor to a metastable conductor, *Phys. Rev. B* 74, 035206 (2006), cited on page 5.

[IZ07] Ielmini D., Zhang Y. G., Analytical model for subthreshold conduction and threshold switching in chalcogenide-based memory devices, *J. Appl. Phys.* 102, 054517 (2007), cited on page 5.

[IZ072] Ielmini D., Zhang Y. G., Evidence for trap-limited transport in the subthres-hold conduction regime of chalcogenide glasses, *Appl. Phys. Lett.* 90, 192102 (2007), cited on page 5.

[Ielm08] Ielmini D., Threshold switching mechanism by high-field energy gain in the hopping transport of chalcogenide glasses, *Phys. Rev. B* 78, 035308 (2008), cited on page 5.

[Zald12] Zalden P., Phase-Change Materials: Structure, vibrational states and thermo-dynamics of crystallization, *Doctoral dissertaion*, RWTH Aachen University, p 93, 142, 173, 146 (2012), cited on page 2, 7, 113.

[BI11] Boniardi M., Ielmini D., Physical origin of the resistance drift exponent in amorphous phase change materials, *Appl. Phys. Lett.* 98, 243506 (2011), cited on page 7.

[Kreb10] Krebs D., Electrical Transport and Switching in Phase Change Materials, *Doctoral dissertaion*, RWTH Aachen University (2010), cited on page 8.

[Krem09] Kremers S., Optische Eigenschaften von Phasenwechselmaterialien für zukünftige optische und elektronische Speicheranwendungen, *Doctroal dissertation*, RWTH Aachen University (2009), p 91, cited on page 2, 10, 89, 90, 117, 119, 123, 125, 129, 137, 140, 141, 145.

[BM05] Barsoukov E., Macdonald J. R., Impedance spectroscopy: Theory, Experie-ment, and Applications, *New Jersey*, p. 16 (2005), cited on page 32.

[BCS88] Bates J. B., Chu Y. T., Stribling W. T., Surface topography and impedance of metal-electrolyte interfaces, *Phys. Rev. Lett.* 60, 627 (1988), cited on page 32.

[Asal93] Asal R. A., The metal-insulator transition in the amorphous silicon-nickel system, *Dissertation*, Bangalore University (1993), cited on page 16.

[Rahm11] Rahman M. M., Electrical thermal and optical studies on chalcogenide glasses suitable for phase change memory applications, *Dissertation*, Bangalore University (2011), cited on page 16.

[KKA+16] Khan Z. H., Khan S. A., Agel F. A., Salah N. A., Husain M., Chalcogenides to Nanochalcogenides; Exploring Possibilities for Future R&D in book: Advances in nanomaterials, published by *Springer India* (2016), cited on page 16.

[CFO69] Cohen M. H., Fritzsche H., Ovshinsky S. R., Simple Band Model for Amorphous Semiconducting Alloys, *Phys. Rev. Lett.* 22,1065 (1969), cited on page 16.

[Kirk73] Kirkpatrick S., Percolation and conduction, *Rev. Mod. Phys.* 45, 574 (1973), cited on page 17.

[MO71] Marshall J. M., Owen A. E., Drift mobility studies in vitreous arsenic trise-lenide, *Philos. Mag.* 24, 1281–1305 (1971), cited on page 17.

[AS03] Anthopoulos T. D., Shafai T. S., Alternating current conduction properties of thermally evaporated α-nickel phthalocyanine thin films: Effects of oxygen doping and thermal annealing, *J. Appl. Phys.* 94, 4, (2003), cited on page 18, 114.

[Mans80] Mansingh A., AC conductivity of amorphous semiconductors, *Bull Mater. Sci.* 2, 325–351 (1980), cited on page 19.

[FAH05] Farid A. M., Atyia H. E., Hegab N. A., AC conductivity and dielectric properties of Sb_2Te_3 thin films, *Vacuum* 80(4), 284–294 (2005), cited on page 19, 111, 113.

[AM76] Ashcroft N. W. , Mermin N. D., Solid State Physics, published by *Saunders College*, (1976), cited on page 19.

[MD79] MOTT N. F., DAVIS E. A., Electronic Processes in Non-Crystalline Materials, published by *Clarendon-Press*, Oxford (1979), cited on 17, 18, 20.

[Luck12] Luckas J., Electronic Transport in Amorphous Phase-Change Materials, *Dissertation*, RWTH Aachen (2012), cited on page 2, 18, 21, 22, 88.

[KK58] Kasuya T., Koide E., A Theory of Impurity Conduction. II, *J. Phys. Soc. Jpn.* 13, 1287–1297 (1958), cited on page 22.

[MA60] Miller A., Abrahams E., Impurity Conduction at Low Concentrations, *Phys. Rev.* 120, 745 (1960), cited on page 22.

[Mott69] Mott N. F., Conduction and switching in non-crystalline materials, *Contemp. Phys.* 10, 125 (1969), cited on page 22.

[Schm68] Schmidlin F. W., Theory of Multiple Trapping, *Solid State Commun.* 22, 401–474 (1977), cited on page 22.

[Mott68] Mott N. F., Conduction in glasses containing transition metal ions, *J. Non-Cryst. Solids* 1,1–17 (1968), cited on page 23.

[SK03] Schönhals A., Kremer F., Analysis of Dielectric Spectra in book: Broadband Dielectric Spectroscopy, published by *Springer* (2003), cited on page 26.

[Deby13] Debye P., *Ver. Deut. Phys. Gesell.* 15, 777 (1913), cited on page 27.

[Bött52] Böttcher C. J., Dielectrics in Static Fields in book: Theory of Electric Polarization, published by *Elsevier Publishing Company* (1952), cited on page 27.

[DG02] Dressel M., M., Grüner G., Electrodynamics of Solids, published by *Cambridge University Press*, UK (2002), cited on page 28.

[Scot71] Scott J. F., Raman Spectra and Lattice Dynamics of α-Berlinite ($AlPO_4$), *Phys. Rev. B* 4, 1360–1366 (1971), cited on page 29.

[GL97] Gonze X., Lee C., Dynamical matrices, Born effective charges, dielectric permittivity tensors, and interatomic force constants from density-functional perturbation theory, *Phys. Rev. B* 55, 10355–10368 (1997), cited on page 29, 90.

[BIS+12] Bhagyajyoti, Immanuel J., Sudheer L. S., Bhaskar P., Parvathi C. S., Review on Lock-in Amplifier, *IJSETR* 1, 40-45 (2012), cited on page 33.

[PPMS11] PPMS Electrical Transport Option (ETO) User's Manual, Quantum Design, Chapter 1, 1-3 (2011), cited on page 34.

[Schl12] Schlich F. F., Phase-transitions in crystalline IV-VI alloys for phase-change memory devices and impedance spectroscopy on amorphous phase-change materials, *Master thesis*, RWTH Aachen University (2012), cited on page 11, 36, 38, 49, 52, 66, 67, 68, 70, 93, 95, 98, 121, 145.

[Krüg10] Krüger K., Impedanzspektroskopie an amorphen Phasenwechselmaterialien, *Diplomarbeit*, RWTH Aachen University, p64, 32, 33 (2010), cited on page 11, 64, 68, 70, 93.

[Agil] Agilent network analyser basics, *Agilent technologies*, cited on page 37.

[CM] Specification Sheet of Z probe power, high-frequency wafer probe (40 GHz), Cascade Microtech, Inc, cited on page 43.

[UMCS] User Manual Calibration Substrate CSR-8, Suss Microtec, www.suss.com, cited on page 43.

[RS17] Rohde & Schwarz, R&S ZVL Vector Network Analyser Specifications, version 10, (2017), cited on page 42.

[HRC+93] Homes C. C., Reedyk M., Crandles D. A., Timusk T., Technique for measuring the reflectance of irregular, submillimeter-sized samples, *Appl. Opt.* 32, 2976 (1993), cited on page 53.

[CLS14] Chanda G., Lobo R.P.S.M., Schachinger E., Wosnitza J., Naito M., Pronin A. V., Optical study of superconducting Pr_2CuO_x with x ~ 4, *Phys. Rev. B* 90, 024503, 2014, cited on page 53, 57.

[Wiki] https://en.wikipedia.org/wiki/Optical_coating, cited on page 54.

[Jell98] Jellison G. E., Spectroscopic ellipsometry data analysis: measured versus calculated quantities, *Thin Solid Films* 313, 33-39 (1998), cited on page 55.

[Fox01] Fox M., Optical Properties of Solids, published by *Oxford University Press* (2001), cited on page 55.

[AS97] Abdullah A. H., Sherman W. F., Kramers-Kronig type analysis of short spec-tral range reflection spectra, *Vibrational Spectroscopy* 13, 133-142 (1997), cited on page 23.

[Roes65] Roessler D. M., Kramers - Kronig analysis of non-normal incidence reflection, *Br. J. Appl. Phys.* 16, 9 (1965), cited on page 23.

[Mart05] Martin P. M., Handbook of Deposition Technologies for Films and Coatings (3rd Edition) Science, *Applications and Technology* (2005), cited on page 23.

[Kalb06] Kalb J. A., Crystallization kinetics in antimony and tellurium alloys used for phase change recording, *Dissertaion*, RWTH Aachen University (2006), cited on page 23.

[Jost12] Jost P., Charge transport in phase-change materials, *Dissertaion*, RWTH Aachen University (2012), cited on page 62.

[Volk13] Volker H., Disorder and electrical transport in phase-change materials, *Dissertaion*, RWTH Aachen University (2013), cited on page 121.

[LKK+11] Luckas J., Kremers S., Krebs D., Salinga M., Wuttig M., Longeaud C., The influence of a temperature dependent bandgap on the energy scale of modulated photocurrent experiments, *J. Appl. Phys.* 110, 013719 (2011), cited on page 62.

[WM64] Weinman J., Mahler J., An analysis of electrical properties of metal electrodes, *Med. Biol. Eng. Comput.* 2, 299-310 (1964), cited on page 62.

[CJV+17] Chen C., Jost P., Volker H., Kaminski M., Wirtssohn M., Engelmann U., Krüger K., Schlich F., Schlockermann C., Lobo R. P. S. M., Wuttig M., *Phys. Rev. B* 95, 094111 (2017), cited on page 138.

[Basu05] Basu P. K., Theory of Optical Processes in Semiconductors: Bulk and Micro-structures, published by *Oxford University Press Inc. New York*, (2005), cited on page 23.

[Kuz05] Kuzmenko A. B., Kramers-Kronig constrained variational analysis of optical spectra, *Rev. Sci. Instrum.* 76, 083108 (2005), cited on page 57.

[Norr12] Norrman N. O., Messung der statischen Dielektrizitätszahl von amorphen Phasenwechselmaterialien bei tiefen Temperaturen, *Bachelor thesis*, RWTH Aachen University, p16 (2012), cited on page 79.

[KE15] V. S. Kostiantyn, F. V. Eugen, Influence of the local structure in phase-chage materials on their dielectric permittivity, *Nanoscale Res. Lett.* 10 (2015), cited on page 85.

[Moli91] M. I. Molina, Sum rule in the many-phonon problem, *Phys. Lett. A* 161 (1991), cited on page 85.

[IVK+99] I. V. Bodnar, V. F. Gremenok, K. Bente, TH. Doering, W. Schmitz, Optical Properties of AgInTe2 Films Prepared by Pulsed Laser Deposition, *Phys. Stat. Sol. (a)* 175, 607 (1999), cited on page 136.

[MJ05] Macdonald R. J., Johnson W. B., Fundamentals of Impedance Spectroscopy in book Impedance Spectroscopy: Theory, Experiment, and Applications, published by *JohnWiley & Sons, Inc*., Hoboken, New Jersey, second edition (2005), cited on page 101, 111.

[LZZ+13] Li Y., Zhong Y. P., Zhang J. J., Xu X. H., Wang Q., Xu L., Sun H. J., Miao X. S., Intrinsic memristance mechanism of crystalline stoichiometric $Ge_2Sb_2Te_5$, *Appl. Phys. Lett.* 103, 043501 (2013), cited on page 111.

[SKM+13] Singh G., Kaura A., Mukul M., Tripathi S. K., Electrical, optical, and thermal properties of Sn-doped phase change material $Ge_2Sb_2Te_5$, *J. Mater. Sci.* 48, 299–303 (2013), cited on page 111.

[HHH12] Huang Y. H., Huang Y. J., Hsieh T. E., A study of phase transition behaviors of chalcogenide layers using in situ alternative-current impedance spectroscopy, *J. Appl. Phys.* 111, 123706 (2012), cited on page 111.

[Elli87] Elliott S. R., A.c. conduction in amorphous chalcogenide and pnictide semiconductors, *Adv. Phys.* 36, 135–217 (1987), cited on page 111.

[KRR+09] Krebs D., Raoux S., Rettner C. T., Burr G. W., Salinga M., Wuttig M., Threshold field of phase change memory materials measured using phase change bridge devices. *Appl. Phys. Lett.* 95, 082101, (2009), cited on page 99.

[RCD+11] Raoux S., Cabrera D., Devasia A., Kurinec S., Cheng H. Y., Influence of Dopants on the Crystallization Temperature, Crystal Structure, Resistance, and Threshold Field for $Ge_2Sb_2Te_5$ and GeTe Phase Change Materials. E/PCOS, (2011), cited on page 99.

[WSK+03] Waghmare U. V., Spaldin N. A., Kandpal H. C., Seshadri R., First-principles indicators of metallicity and cation off-centricity in the IV-VI rocksalt chalcogenides of divalent Ge, Sn, and Pb, *Phys. Rev. B* 67, 125111 (2003), cited on page 134.

[Gray65] Gray H. B., Electrons and Chemical Bonding, published by *W. A. Benjamin-Inc*., New York, (1965), cited on page 134.

[LA71] Lakatos A. I., Abkowitz M., Electrical Properties of Amorphous Se, As_2Se_3, and As_2S_3, *Phys. Rev. B* 3, (1971), cited on page 16, 114.

[AJ12] Akola J., Jones R. O., Amorphous structures of Ge/Sb/Te alloys: Density functional simulations, *Phys. Status Solidi* 249, 1851–1860 (2012), cited on page 4.

[LKG+13] Luckas J., Krebs D., Grothe S., Klomfaß J., Carius R., Longeaud C., Wuttig M., Defects in amorphous phase-change materials, *J. Mater. Res.* 28, 1139, 2013, cited on page 16.

[SKL+17] Sherchenkov A. A., Kozyukhin S. A., Lazarenko P. I., Babich A. V., Bogoslovskiy N. A., Sagunova I. V., Redichev E. N., Electrical properties and transport mechanisms in phase change memory thin films of quasi-binary- line GeTe-Sb_2Te_3 chalcogenide semiconductors, *Semiconductors* 51(2), (2017), cited on page 2, 103.

[PBK+08] Park J. W., Baek S. H., Kang D. T., Lee H., Kang Y. S., Lee T. Y., Suh D. S., Kim K. J., Kim C. K., Khang Y. H., Silva J. L. F., Wei S. H., Optical properties of (GeTe, Sb_2Te_3) pseudobinary thin films studied with spectroscopic ellipsometry, Jun-Woo Park, *Appl. Phys. Lett.* 93, 021914 (2008), cited on page 10.

[SGZ95] Salam F., Giuntini J. Ch., Zanchetta J. V., Ionic conductivity of silver chalcogenide glasses, *Ionics,* 1, 171 (1995), cited on page 137.

[LM70] Lowndes R. P., Martin D. H., Dielectric constants of ionic crystals and their variations with temperature and pressure, *Proc. Roy. Soc. Lond. A.* 316, 351-375 (1970), cited on page 23, 118.

[Mott87] Mott S. N., The mobility edge since 1967, *J. Phys. C: Solid State Phys.* 20, 3075 (1987), cited on page 16.

[VSC04] Vaz A. R., Salvadori M. C., Cattani M., Young modulus measurement of nanostructured metallic thin films, *J.M.N.M.* 20-21, 758-762 (2004), cited on page 69.

[Mori99] Morigaki K., Physics of amorphous semiconductors, published by *Imperial college press* (1999), cited on page 22.

[Penn62] Penn D., Wave-number-dependent dielectric function of semiconductors, Phys. Rev. 128 (5), 2093 (1962), cited on page 89.

[ABE+00] Afifi M. A., Bekheet A. E., Elwahhab E. Ahd, Atyia H. E., Ac conductivity and dielectric properties of amorphous In_2Se_3 films, Vacuum 61, 9 (2001), cited on page 114.

[Käs17] Käs M., Electrical transport in micro- and nano-scale devices of amorphous phase-change materials, *Dissertation*, RWTH Aachen University (2017), cited on page 114.

Acknowledgements

Firstly and foremost I would like to thank Prof. Matthias Wuttig for offering me the opportunity to do the PhD at the I Physikalisches Institute IA, RWTH Aachen. I have experienced an amazing time in Aachen. I am deeply grateful for his guidance and encouragement during the hard time and I will never forget his enthusiasm for science.

I am particularly grateful to Dr. Hanno Volker, who is the best officemate and a nice person. He offered me a lot of help from time to time in the past years, such as in experiments discussion and scientific writing.

I would also like to thank Dr. Peter Jost a lot. He is a very patient and helpful colleague. During my doctoral study, he gave me many wise advices and helped me in solving some puzzles. In addition, he contributed a lot to our paper.

I really appreciate Dr. Ricardo P.S.M. Lobo a lot for his great deal of work in carrying out FT-FIR measurements and data analyzing as well as the fruitful discussions. In addition, I am truly grateful to Dr. Martin Salinga for the access to the vacuum cryostat for the temperature dependent impedance measurements.

I am very thankful to Marvin Kaminski and Matti Wirtssohn for their help in the sample preparation. I would also like to thank my bachelor student Nils Oscar Norrman for his effort in the AC electrical measurement at low frequencies. Thanks for the help from Dr. Felix Lange, Sebnem Yazici and Henning Hollermann for the process of sample HF etching.

I would like to thank the colleagues in our lab, who introduced me several experimental setups and provided technical support, Dr. Martin Wimmer, Dr. Matthias Käs and Christoph Persch, Dr. Daniel Dorow Gesprach, Stephan Hermes, Sebastian Mohrhenn. Thanks for the former work of the topic by Kathrin Krüger, Franziska Schlich and Carl Schlockermann. Thanks for the thesis proofreading by Prof. Matthias Wuttig, Dr. Ricardo Lobo, Dr. Hanno Volker, Dr. Peter Jost, Dr. Weiwei Zhou, Dr. Shuai Wei, Dr. Julia Walter, Dr. Min Zhu and Yudong Cheng.

Thanks for insightful discussions with Dr. Peter Zalden, Dr. Wei Zhang, Dr. Ju-Young Cho and thanks for the cooperation from all other colleagues.

I am obliged to the financial support by the China Scholarship Council (CSC) and the Deutsche Forschungsgemeinschaft (SFB917). In the end, I would like to dedicate this thesis to my family, who are always being there for me.